JOURNAL OF GEOPHYSICAL RESEARCH, VOL. 108, NO. D20, 4634, doi:10.1029/2001JD001253, 2003

Monthly averages of aerosol properties: A global comparison among models, satellite data, and AERONET ground data

S. Kinne,[1] U. Lohmann,[2] J. Feichter,[1] M. Schulz,[3] C. Timmreck,[1] S. Ghan,[4] R. Easter,[4] M. Chin,[5] P. Ginoux,[6] T. Takemura,[7] I. Tegen,[8] D. Koch,[9] M. Herzog,[10] J. Penner,[10] G. Pitari,[11] B. Holben,[5] T. Eck,[12] A. Smirnov,[12] O. Dubovik,[12] I. Slutsker,[12] D. Tanre,[13] O. Torres,[14] M. Mishchenko,[15] I. Geogdzhayev,[9] D. A. Chu,[12] and Y. Kaufman[5]

Received 29 August 2001; revised 18 March 2002; accepted 12 March 2003; published 21 October 2003.

[1] New aerosol modules of global (circulation and chemical transport) models are evaluated. These new modules distinguish among at least five aerosol components: sulfate, organic carbon, black carbon, sea salt, and dust. Monthly and regionally averaged predictions for aerosol mass and aerosol optical depth are compared. Differences among models are significant for all aerosol types. The largest differences were found near expected source regions of biomass burning (carbon) and dust. Assumptions for the permitted water uptake also contribute to optical depth differences (of sulfate, organic carbon, and sea salt) at higher latitudes. The decline of mass or optical depth away from recognized sources reveals strong differences in aerosol transport or removal among models. These differences are also a function of altitude, as transport biases of dust do not always extend to other aerosol types. Ratios of optical depth and mass demonstrate large differences in the mass extinction efficiency, even for hydrophobic aerosol. This suggests that efforts of good mass simulations could be wasted or that conversions are misused to cover for poor mass simulations. In an attempt to provide an absolute measure for model skill, simulated total optical depths (when adding contributions from all five aerosol types) are compared to measurements from ground and space. Comparisons to the Aerosol Robotic Network (AERONET) suggest a source strength underestimate in many models, most frequently for (subtropical) tropical biomass or dust. Comparisons to the combined best of Moderate-Resolution Imaging Spectroradiometer (MODIS) and Total Ozone Mapping Spectrometer (TOMS) indicate that away from sources, model simulations are usually smaller. Particularly large are discrepancies over tropical oceans and oceans of the Southern Hemisphere, raising issues on the treatment of sea salt in models. Totals for mass or optical depth in many models are defined by the absence or dominance of only one aerosol component. With appropriate corrections to that component (e.g., to removal, to source strength, or to seasonality) a much better model performance can be expected. Still, many important modeling issues remain inconclusive as the combined result of poor coordination (different emissions and meteorology), insufficient model output (vertical distributions, water uptake by aerosol type), and unresolved measurement issues (retrieval assumptions and temporal or spatial sampling biases). *INDEX TERMS:* 1610 Global Change: Atmosphere (0315, 0325); 1615 Global Change: Biogeochemical processes (4805); 3319 Meteorology and Atmospheric Dynamics: General circulation;

[1]Max-Planck-Institut für Meteorologie, Hamburg, Germany.
[2]Department of Physics, Dalhousie University, Halifax, Nova Scotia, Canada.
[3]Laboratoire des Sciences du Climat et l'Environnement, Gif-sur-Yvette, France.
[4]Pacific Northwest National Laboratory, Battelle, Richland, Washington, USA.
[5]NASA Goddard Space Flight Center, Greenbelt, Maryland, USA.
[6]Geophysical Fluid Dynamics Laboratory, NOAA, Princeton, New Jersey, USA.
[7]Research Institute for Applied Mechanics, Kyushu University, Fukuoka, Japan.
[8]Max-Planck-Institut für Biogeochemie, Jena, Germany.
[9]Department of Applied Physics and Applied Mathematics, Columbia University-NASA Goddard Institute for Space Studies, New York, USA.
[10]Department of Atmospheric, Oceanic and Space Sciences, University of Michigan, Ann Arbor, Michigan, USA.
[11]Dipartimento di Fisica, Università degli Studi dell'Aquila, L'Aquila, Italy.
[12]Goddard Earth Sciences and Technology Center, University of Maryland Baltimore County-NASA Goddard Space Flight Center, Greenbelt, Maryland, USA.
[13]Laboratoire d'Optique Atmosphérique, Université des Sciences et Technologies de Lille 1, Lille, France.
[14]Joint Center for Earth Systems Technology, University of Maryland Baltimore County-NASA Goddard Space Flight Center, Greenbelt, Maryland, USA.
[15]NASA Goddard Institute for Space Studies, New York, USA.

0148-0227/03/2001JD001253

KEYWORDS: tropospheric aerosol, aerosol component modeling, aerosol module evaluation, direct aerosol radiative forcing, regional comparisons

Citation: Kinne, S., et al., Monthly averages of aerosol properties: A global comparison among models, satellite data, and AERONET ground data, *J. Geophys. Res.*, *108*(D20), 4634, doi:10.1029/2001JD001253, 2003.

1. Introduction

[2] Aerosol introduces one of the largest uncertainties in model-based estimates of anthropogenic forcing on climate [*Houghton et al.*, 1995, 2001]. Thus an adequate representation of aerosol properties in these climate models is essential. To improve the characterization for concentration, size and absorption of aerosol on regional and seasonal scales, new aerosol modules were developed. In contrast to prior schemes, these new modules distinguish among different aerosol types or components. Components have their individual sources and their individual properties for size, (spectral) absorption and humidification (their ability to swell in size with increases to the ambient relative humidity). In separate processes, sources of each aerosol type are translated into aerosol mass, then converted into optical depth and eventually associated with a forcing. And it is the sum of aerosol component forcings that defines the aerosol impact on climate. To trust these climate assessments, the new aerosol modules must be tested.

[3] The validation of aerosol modules, however, is extremely difficult. Measurements of aerosol properties (e.g., optical depth) from ground or space exist. Particularly complete are data of the Aerosol Robotic Network (AERONET). However, all these remote sensing measurements are highly integrated: not only over the atmospheric column but also over all aerosol components. Thus investigations for the treatment of a particular aerosol type may be limited to seasons and regions, when or where that aerosol type dominates the aerosol composition. To make matters worse, many measurements are local in nature and/or temporally sparse or already contaminated by a-priori assumptions. With these limitations in mind only general evaluations of the new aerosol modules are possible. In this study, based on a comparison of monthly averages for a complete yearly cycle, regional model tendencies are explored. This is done in consistency tests among models and in comparisons to data from ground and space.

[4] First, the models are introduced. This includes a review of assumptions for aerosol type properties. Then model biases are identified on the basis of regional monthly averages. Finally, aerosol data sets of multiyear measurements from ground and space are introduced and comparisons to model simulations are examined and evaluated.

2. Models

[5] Our understanding of climatic impacts resulting from changes to atmospheric properties is largely based on simulations with global models. For aerosol, many uncertainties regarding its climatic impact are a direct consequence of simplifications to the variable nature of aerosol on regional and seasonal scales. Thus, for a better representation of aerosol properties, new aerosol modules distinguish among at least five aerosol types: sulfate, organic carbon, black carbon, dust and sea salt. These aerosol types differ not only in composition, size, humidification and/or lifetime, but also in their distributions globally by season. Thus a distinction by aerosol type promises a better representation of aerosol properties regionally and seasonally. However, the necessity of additional assumptions adds to an already uncertainty-rich multiple step process: The four basic modeling steps of Figure 1 now need to be simulated individually for each aerosol type.

[6] First, emissions of each aerosol type and their precursors are prescribed or calculated. Then aerosol type sources are individually processed to yield a distribution of aerosol mass. This aerosol processing is highly parameterized and closely linked to meteorological conditions. These are generated or prescribed depending on the model. The processing includes atmospheric chemistry (e.g., gas to particle conversions for sulfate and organic carbon), transport (advection, diffusion, convection) and removal (dry or wet deposition and sedimentation). Next, aerosol mass is converted into optical depth, on the basis of assumptions on size, absorption and humidification of aerosol and on prescribed ambient relative humidity. With variations to these properties on regional and seasonal scales, these conversions will vary. Finally, the (direct) aerosol climatic impact is derived as radiative transfer methods associate the simulated aerosol properties with a change in the energy balance, where the change at the top of the atmosphere captures the climatic impact.

[7] In this study, intermediate results of new aerosol modules of seven models are investigated. As model results

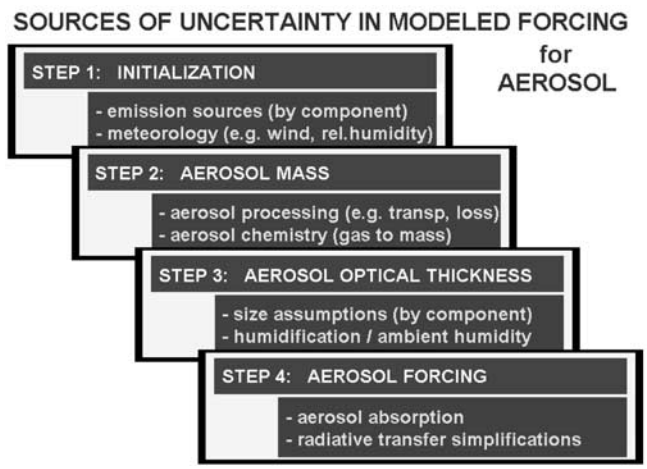

Figure 1. The four major modeling steps (and their most important associated items) of aerosol modules in global climate models to determine the aerosol direct forcing. See color version of this figure in the HTML.

Table 1. Comparison of Model Resolution, Meteorology, and References for Emission Sources[a]

	EC ECHAM4	GO GOCART	MI MIRAGE	GI GISS	CC Sprintars	GR Grantour	UL ULAQ
Origin	MPI,ger	NASA,us	PNNL,us	NASA,us	Kyushu,jap	U.Mich,us	U.Aquila,it
Grid (lon/lat)	3.8 × 3.8	2.5 × 2.0	2.8 × 2.8	4.0 × 5.0	1.1 × 1.1	5.6 × 5.6	10 × 22.5
Vert.layers	19	20 (26)	24	9	11	19	25
Simulation	50 years	′90′96′97	6′94-5′95	3 years	′90	1 year	5 years
Met-data	generated	geos/das	ECMWF	generated	ncar/ncep	echam3.6	from gcm
Clouds	prognostic	diagnostic	prognostic	prognostic	prognostic	prognostic	diagnostic
Hum.growth	r1	r1	r2		r3		r2
Emis: dust	r4	r5	r6	r7	r8	r5	r5
Emis: carb.	r9, r10	r11, r12	r9, r10	r9	r9, r13, r10	r9, r10	r9, r12
Emis: salt	r14	r15	r16	r15	r17		
Surf. winds	prognostic	SSM/I	ECMWF	r18	prognostic	r18	r18
Emis: sulf.	r19	r20	r19	r19	r19	r19	r19
Sulf.oxidant	imported	imported	co-ch4 ch.	semi-prog	imported	imported	imported

[a]MIRAGE: Water-uptake is based on ECMWF relative humidity and nudges towards ECMWF winds and temperatures. GISS: Oxidant precursors are imported rather than oxidants (H_2O_2 is carried as a prognostic species). References: r1, *Koepke et al.* [1997]; r2, *Koehler* [1936]; r3, *Hobbs et al.* [1997]; r4, *Schulz et al.* [1998]; r5, *Ginoux et al.* [2001]; r6, *Gillette and Passi* [1988]; r7, *Tegen and Fung* [1995]; r8, *Gillette* [1978]; r9, *Liousse et al.* [1996]; r10, *Cooke and Wilson* [1996]; r11, *Duncan et al.* [2003]; r12, *Cooke et al.* [1999]; r13, *Guenther et al.* [1995]; r14, *Guelle et al.* [2001]; r15, *Monahan et al.* [1986]; r16, *O'Dowd et al.* [1997]; r17, *Erickson et al.* [1986]; r18, *Gong et al.* [1997]; r19, *Benkowitz et al.* [1996]; r20, *Olivier et al.* [1996].

depend on model specific assumptions, model details are introduced first. Special attention was given to assumptions for the conversion of aerosol mass into aerosol optical depth.

2.1. Model Specifications

[8] Aerosol modules of seven global models are compared. The models primarily simulate tropospheric processes at horizontal resolutions of about 300 × 300 km. The models can be divided into two classes: Global circulation models (GCMs), which generate their own meteorology, and chemical transport models (CTMs), which adopt meteorological data (usually for a particular year). For GCMs the link to a particular year can be accomplished through nudging, an elementary form of data assimilation. Nudging in GCMs reduces biases of simulated circulation and simulated winds.

[9] 1. ECHAM4 (EC) is a global circulation model [*Roeckner et al.*, 1996; *Lohmann et al.*, 1999], which originated at the Max-Planck-Institute for Meteorology (Hamburg, Germany). Wind, temperature and pressure fields are generated without a link to a particular year (50 year simulation). (Successful nudging to ECMWF data from 1993 to 1997 has been demonstrated, though it is not considered here.)

[10] 2. MIRAGE (MI) is a chemical transport model of PNNL (Richland, Washington, United States), which is coupled on-line with a global circulation model [*Ghan et al.*, 2001a, 2001b]. To improve agreement on time-scales of days nudging has been applied. Results are based on ECMWF assimilated wind, temperature and sea-surface temperature fields from June 1994 to May 1995.

[11] 3. GOCART (GO), from Georgia Institute of Technology and NASA-Goddard (Atlanta, Georgia/Greenbelt, Maryland, United States), is a chemical transport model [*Chin et al.*, 2000, 2002; *Ginoux et al.*, 2001] driven by assimilated meteorological fields from the GEOS DAS (Goddard Earth Observing System Data Assimilation System). Simulations usually refer to 1990. Additional simulations with meteorological data for 1996 and 1997 were used to demonstrate year-to-year variability.

[12] 4. CCSR (CC) (or SPRINTARS) from the Center for Climate System Research at the University of Tokyo and from Kyushu University (Tokyo and Kyushu, Japan), is a chemical transport model [*Takemura et al.*, 2000, 2002]. The model is coupled with the CCSR/NIES (National Institute for Environmental Studies) atmospheric general circulation model. Here, results are based on nudged wind, temperature and pressure fields of the NCEP/NCAR (National Center for Environmental Predictions/National Center for Atmospheric Research) reanalysis for 1990.

[13] 5. GISS (GI), the community model of NASA-GISS (New York City, United States) is a global circulation model [*Tegen et al.*, 1997, 2000; *Koch et al.*, 1999; *Koch*, 2001]. Fields for wind, temperature and pressure are generated without a link to a particular year (3 year simulation).

[14] 6. Grantour (Gr), from the University of Michigan (Ann Arbor, Michigan, United States), is a Lagrangian model that treats the global scale transport, transformation and removal of trace species in the atmosphere [*Walton et al.*, 1988]. Wind, temperature and pressure fields are generated without a link to a particular year (1 year simulation).

[15] 7. ULAQ (UL) is a coarse resolution chemical transport model [*Pitari et al.*, 2002] from the University of L'Aquila (Italy). Meteorological variables are generated in a coupled GCM model (5 year simulation).

[16] Next, individual model assumptions with respect to the four steps of Figure 1 are explored in more detail.

2.1.1. Initialization

[17] The meteorological data provide the background in model simulations. The meteorology is either generated (GCM) or prescribed (CTM) by observed meteorological data (e.g., wind, temperature, pressure). Meteorological data of all models differed, because even when identical years in CTMs were selected, the sources of assimilation data differed. Model characteristics parameters, including choices for meteorology are summarized in Table 1.

[18] One of the more important reasons to explain differences in simulated aerosol properties are adopted data for aerosol emissions. The IPCC report [*Houghton et al.*, 2001] provides a comprehensive overview on current data sets for aerosol components. For the seven evaluated models the

primary references for each aerosol type are listed in Table 1. Even when the same primary reference is given, many uncertainties regarding the comparability of source strength among models remain. Differences in data implementation (daily or monthly averages), a dependence on meteorology (near surface winds) and the use of secondary data dilute a clear picture of source strength. Future model evaluations need to focus on assumptions for source strength and seasonality as not to attribute their differences to aerosol processing.

2.1.2. Toward Aerosol Mass

[19] The processing of emission sources toward a distribution of 3-D mass fields for each aerosol type involves many processes. All models address the major aerosol mechanisms, including sulfate chemistry (gas to particle conversion), transport (advection, diffusion and convection) and aerosol processing: (1) dry deposition: aerosol clustering from turbulent mixing; (2) in-cloud scavenging: (a) aerosol can act as cloud condensation nucleus and (b) aerosol can diffuse in cloud drops with subsequent removal via precipitation; (3) below-cloud scavenging: aerosol capture and removal by rain; (4) aerosol re-emission: by evaporation of rain or cloud drops; (5) gravitational settling.

[20] Most of these processes are highly parameterized and tuned to model resolution. Thus aerosol processing to mass has one of the largest potentials for errors. More detailed model comparisons in the future have to include tests of particular processes (e.g., tracer studies to understand transport biases or comparisons of near surface wind fields). In addition, control experiments linked to a particular aerosol type are very much needed, similar to a recently concluded comparison of simulated (near surface) sulfate mass to local measurements in COSAM [*Lohmann et al.*, 2001; *Barrie et al.*, 2001; *Roelofs et al.*, 2001].

2.1.3. Toward Aerosol Optical Depth

[21] In the new aerosol modules the (dry) aerosol mass m is converted to aerosol optical depth τ, separately for each aerosol type. The conversion factor, as the ratio between optical depth and dry mass, is called the mass extinction efficiency b (units in m^2/g). For a distribution of spheres, b is defined by

$$b = \tau/m = 0.75\ Q/(\rho\ r_e)H$$

where Q is the extinction efficiency, ρ is the density, r_e is the effective radius ($\Sigma r^3/\Sigma r^2$), and H is the humidification factor.

[22] The extinction efficiency Q is the ratio between extinction cross-section and the geometric cross-section. Q depends on aerosol size and composition. Q is largest, if particle radius and interacting wavelength have similar values. Maximum values for Q near values of 3 are common for size-distributions with effective radii of about 0.5 μm at mid-visible wavelengths. Q converges towards 2 for increasingly larger radius-to-wavelength ratios (geometrical limit). For increasingly smaller radius-to-wavelength ratios, Q decreases sharply (inverse proportional to 4th power) for scattering aerosol but only moderately (inverse proportional) for absorbing aerosol. For hydrophilic aerosol components (e.g., sulfate, sea salt and organic carbon) water uptake impacts Q in two ways: Water uptake increases the aerosol size, thereby increasing the radius-to-wavelength ratio. And water uptake decreases the aerosol absorption, which is less important if the effective aerosol radius is larger than the wavelength.

[23] The humidification factor H accounts for effects of water uptake by hydrophilic aerosol types.

$$H = 1 \qquad \text{for hydrophobic aerosol}$$

$$H = \left(Q_{,hum}/Q\right)\left(r_{e,hum}/r_e\right)^2 \qquad \text{for hydrophilic aerosol}$$

The subscript ($_{hum}$) indicates values at ambient (moist) conditions as compared to completely dry conditions. Thus the radius ratio ($r_{e,hum}/r_e$) captures aerosol swelling. This swelling is nonlinear, as a function of the ambient relative humidity, which can vary strongly within the region of a model grid point. Thus choices for the regional effective ambient relative humidity become a critical issue for the sizing of hydrophilic aerosol types.

[24] Given the multiparameter influence for m-to-τ conversions, model assumptions for size, humidification, density and composition (refractive index influences values for Q) are compared next.

2.1.3.1. Size Assumptions

[25] Larger mass extinctions efficiencies are associated with smaller (and especially absorbing) aerosol and with more humid environments. Table 2 provides a summary of size-assumptions.

[26] A higher number of size-classes (or size modes) can better represent the observed aerosol size distributions. This is particularly important when super-micrometer sizes are involved, and recognized with 2 to 10 size-classes for dust and sea salt. In contrast, for sulfate and carbon aerosol most models consider only a single (submicrometer) size class. Such simplification permits a direct comparison among models. For sulfate, the dry size is large in GISS and small in Grantour, relative to other models. For both carbon types, the dry sizes in GISS and also CCSR are large, whereas dry sizes in ECHAM4 and GOCART are small (although their assumed wide distribution permits few larger sizes to contribute).

2.1.3.2. Humidification Assumptions

[27] The mass extinction efficiency is also a function of environmental conditions. The ambient relative humidity moderates the size of hydrophilic aerosol. Most models allow water uptake only for sulfate, sea salt and organic carbon. Size and relative humidity relationships are summarized in Table 3.

[28] Most models recognize the nonlinear relationship between size and humidity. However, there are significant differences already at intermediate relative humidities (50–80%). With respect to aerosol size, the assumed swelling (or radius increase) is usually stronger for larger aerosol (e.g., sea salt versus sulfate). With respect to aerosol type the assumed swelling is usually stronger for sulfate than for carbon. This is in agreement with observed correlations between size and ambient relative humidity at several U.S. National Park sites [*Malm et al.*, 1994; D. Day and W. Malm, private communication, 2000]. In Table 3, the locations of Grand Canyon, Arizona, and Big Bend, Texas, provide data for carbon-dominated aerosol, whereas Great

Table 2. Comparison of Assumed Dry Aerosol Sizes in Models[a]

	EC	GO	MI	GI	CC	Gr	UL
DU	***2*** *sizes* variable *smaller away from sources*	***7*** *sizes* .14, .24, .45, .80, 1.4, 2.4, 4.5	***2*** *sizes* .16, .75	***8*** *sizes* .15, .25, .40, .80, 1.5, 2.5, 4.0, 8.0	***10*** *sizes* .13, .20, .33, .52, .82, 1.3, 2.0, 3.2, 5.1, 8.0	***2*** *sizes* .88, 1.91	***5*** *sizes* $.01 \times 2^n$, $n = 5,..9$
OC	***1*** *size* .11	***1*** *size* .10	***2*** *sizes* .02, .16	***1*** *size* .50	***1*** *size* .24	***1*** *size* .17	***5*** *sizes* $.01 \times 2^n$, $n = 2,..5$
BC	***1*** *size* .04	***1*** *size* .04	***2*** *sizes* .02, .16	***1*** *size* .10	***1*** *size* .067	(in OC)	***5*** *sizes* $.01 \times 2^n$, $n = 1,..4$
SS	***2*** *sizes* variable *function of surface winds*	***2*** *sizes* .80, 5.7 *data from four size bins*	***2*** *sizes* .16, 2.7	***1*** *size* 2.0 *data from six size bins*	***10*** *sizes* .13, .20, .32, .50, .79, 1.3, 2.0, 3.2, 5.0, 7.9	***2*** *sizes* .79, 1.6	***6*** *sizes* $.01 \times 2^n$, $n = 5,..10$
SU	***1*** *size* .24	***1*** *size* .24	***4*** *sizes* .02, .16, .75, 2.7	***1*** *size* .30	***1*** *size* .24	***1*** *size* .12	***16*** *sizes* $.01 \times 2^n$, $n = -5,..10$

[a]For each aerosol type the number of size classes is listed. In addition, mean radii of assumed size-bins or effective radii r_e (third moment to second moment ratio) of assumed lognormal size-distributions are provided (in units of μm). ECHAM4 and GOCART fixed aerosol size modes are based on the GADS data set [*Koepke et al.*, 1997]. MIRAGE assumes internal mixing of components (only model) and predicts number and mass for each of the 4 modes. CCSR assumes for transport processes an internal mixture of organic and black carbon (except for 50% of the black carbon mass originating from fossil fuel) with different oc/bc mass ratios according to the source.

Smoky, Kentucky, provides data for sulfate-dominated aerosol.

[29] The water uptake in hydrophilic aerosol types depends not only on the prescribed humidification (strength, see Table 3) but also on the prescribed ambient relative humidity, which may be in error. Because of the increased sensitivity at higher ambient relative humidities, small humidity errors can have a strong impact on aerosol size and the derived aerosol forcing. Therefore many models introduce less physical but 'more stable' simplifications. These include the replacement of the predicted by (re-analysis) prescribed ambient relative humidities (e.g., MIRAGE), the assumption of a maximum growth factor far before saturation (e.g., sulfate in GISS or sea salt in ULAQ),

Table 3. Comparison of Assumed Humidifications[a]

RH, %	EC	GO	MI	GI	CC	Gr	UL	"Observed"
				OC				
0	1.00	1.00	1.00	1.00	1.00	1.00	1.00	
50	1.24	1.24	1.06	1.00	1.08	1.00	1.01	1.01–1.05
70	1.35	1.35	1.11	1.00	1.10	1.00	1.03	1.15–1.30
80	1.45	1.45	1.17	1.00	1.44	1.00	1.05	1.25–1.50
90	1.65	1.65	1.31	1.00	1.69	1.00	1.09	1.40–1.90
95	1.89	1.89	1.51	1.00	1.96	1.00	1.18	
				SS				
0	1.00	1.00	1.00	1.00	1.43	1.00	1.00	
50	1.30	1.60	1.38	1.00	1.43		1.05	
70	1.49	1.81	1.62	1.00	1.43		1.18	
80	1.57	1.99	1.83	1.00	1.43	1.67	1.45	
90	2.06	2.38	2.27	1.00	1.43		1.52	
95	2.57	2.89	2.84	1.00	1.43		1.55	
				SU				
0	1.00	1.00	1.00	1.00	1.00	1.00	1.00	
50	1.41	1.40	1.20	1.00	1.22	1.28	1.30	1.05–1.20
70	1.57	1.50	1.34	1.06	1.37	1.41	1.52	1.15–1.35
80	1.70	1.60	1.47	1.20	1.48	1.53	1.67	1.20–1.50
90	1.94	1.80	1.77	1.60	1.76	1.75	1.84	1.45–1.80
95	2.27	1.90	2.16	1.60	2.26	2.05	1.92	1.70–2.05

[a]Prescribed size increases for organic carbon (OC), sea-salt (SS) and sulfate size (SU), with respect to their dry size, are compared for ambient relative humidities (RH) of 50, 70, 80, 90 and 95%. Estimates from measured relationships between size (via scattering) and relative humidity are given as well. ULAQ and GISS values are derived from permitted optical depth τ increases, $\Delta(r_{e,hum}/r_e) \sim$ SQRT ($\Delta\tau$). CCSR sea-salt aerosols consist of 70% of salt and 30% of water in mass. GOCART permits limited humidification for black carbon on a time delay basis. GISS uses a growth cap for sulfate at 85% ambient relative humidity (*rh*). "Observed" surface statistics are from three U.S. National Park sites, $\Delta(r_{e,hum}/r_e) \sim$ SQRT (Δ*scattering coefficient*).

Table 4. Comparison of Assumed Dry Mass Densities[a]

	EC	GO	MI	GI	CC	Gr	UL
DU: dust	2.65	2.6	2.6	2.5	2.5	2.5	2.5
OC: organic carbon	1.9	1.8	1.7	1.0	1.47	1.0	2.0
BC: black carbon	1.0	1.0	1.0	1.0	1.25	1.0	1.0
SS: sea salt	2.17	2.2	1.9	2.16	2.25	2.17	2.2
SU: sulfate	1.7	1.7	1.77	1.7	1.77	1.77	1.7

[a]Values are given in g/cm^3.

the prescription of an average swell-factor (e.g., sea salt in CCSR), the omission of swelling altogether (e.g., carbon in Grantour) (if not understood) or worse, the assumption of a constant for the conversion of component mass into optical depth (e.g., carbon and sea salt in GISS) which also rejects all other (e.g., temporal) dependences. In what way these simplifications can be justified is unclear, since neither model provided data on their applied 3-dimensional ambient relative humidity fields. Meaningful future model comparisons have to explore the water uptake for each aerosol type, which may require simulations with prescribed relative humidity fields.

2.1.3.3. Density Assumptions

[30] The dry mass density is inversely proportional to the mass extinction efficiency. Assumed dry mass densities are compared in Table 4. The largest differences among models are for organic carbon. However, the suggested uncertainty of up to 2 only applies to dry aerosol, and the likely water uptake reduces uncertainties (as densities decrease toward 1g/cm^3). For dust, sulfate and sea-salt aerosol components model assumptions are similar, except for the low sea-salt value of MIRAGE. However, also this difference will be washed out with likely water uptake.

2.1.3.4. Composition Assumptions

[31] Mass extinction efficiency is also affected by assumptions to aerosol composition (and absorption) via the extinction efficiency Q. Especially at small size parameters (when aerosol size is small compared to the wavelength) absorption can increase mass extinction efficiencies (e.g., black carbon type in the visible). Absorption by aerosol is a critical parameter in radiative forcing simulations. In fact, a better representation of aerosol absorption is a major reason for the separate treatment of aerosol types in new aerosol modules. Absorption is defined by the refractive index's imaginary part (roughly: >0.1 strong /0.1> moderate >0.001 / <0.001 weak). Its selection for tropospheric aerosol is particularly important at mid-visible wavelengths, because of (weight-) maxima for the product of aerosol extinction and available radiative energy. Assumed refractive indices at a visible and an infrared wavelength for the five aerosol types are compared in Table 5.

[32] The data of Table 5 are for 'dry' aerosol and the addition of water will reduce real and imaginary parts toward the refractive index of water (1.34/0.1e-8). Any similarity among choices in models originates largely from the limited number of catalogued values. However, there are some noteworthy differences.

[33] At visible wavelengths, differences are larger for the imaginary parts of organic carbon and dust:

[34] 1. For dust (vis) the lowest model assumption of 0.002 is supported by statistics from inversions of sky radiances [*Dubovik and King*, 2000] at dust-dominated sites. On the other hand, the largest values of 0.008 are in line with diffuse reflectance measurements [*Patterson et al.*, 1976]. As large optical depths for dust are found in many regions of the world, this difference is significant for simulations of the aerosol radiative forcing. Weaker dust absorption at solar wavelengths reduces the warming of the aerosol layers and increases solar energy losses to space [*Kaufman et al.*, 2001], resulting in a more negative ToA forcing. Absorption of dust increases toward shorter wavelengths (UV) and decreases toward longer wavelengths (near-IR). It is unclear, if and to what degree this important spectral dependence is considered in models with limitations to spectral resolution in their (solar) radiative transfer schemes.

[35] 2. For carbon (vis), absorption is largely determined by the fraction of black carbon. All models agree on strong absorption for black carbon, assuming large refractive index imaginary parts of about 0.5. Less understood is the absorption of organic carbon. Estimates [*Novakov et al.*, 1997] suggest light to moderate absorption with a refractive index imaginary part of near 0.005 at visible wavelengths. However, uncertainties are so large that some models ignore absorption by organic carbon completely. This is not a good choice, even though black carbon is expected to dominate carbon absorption. It should be kept in mind that black carbon only accounts for a small portion of the total carbon

Table 5. Comparison of Assumed Dry Component Refractive Indices at 0.55 and 10 μm (Real Part, Imaginary Part)

	EC	GO	MI	GI	CC	Gr	UL
Visible 0.55 μm							
DU	1.5, ***.0055***	1.5, ***.0078***	1.5, ***.002***	1.56, ***.005***	1.53, ***.008***	1.53, ***.008***	1.56, ***.006***
OC	1.53, ***.006***	1.53, ***.006***	1.55, ***0***	1.53, ***.005***	1.53, ***.006***	1.53, ***0***	1.6, ***.0035***
BC	1.75, ***.44***	1.75, ***.44***	1.9, ***.6***	1.57, ***.5***	1.75, ***.44***	1.75, ***.44***	2.07, ***.6***
SS	1.5, ***0***	1.5, ***0***	1.5, ***0***	1.45, ***0***	1.38, ***0***	1.38, ***0***	1.50, ***0***
SU + MSA[a]	1.43, ***0***	1.43, ***0***	1.53, ***0***	1.43, ***0***	1.43, ***0***	1.43, ***0***	1.45, ***0***
Infrared 10 μm							
DU	2.9, ***.7***	2.57, ***.5***	1.62, ***.12***	3.0, ***1.0***	1.75, ***.162***	1.75, ***.162***	
OC	1.9, ***.1***	1.82, ***.09***	1.7, ***.07***	2.19, ***.13***	1.82, ***.09***	2.19, ***.13***	
BC	2.2, ***.73***	2.21, ***.72***	2.22, ***.73***	2.3, ***1.29***	2.21, ***.72***	2.21, ***.72***	
SS	1.55, ***.02***	1.5, ***.014***	1.5, ***0***	1.53, ***.016***	1.31, ***.04***	1.31, ***.04***	
SU + MSA[a]	1.95, ***.455***	1.89, ***.455***	1.98, ***.06***	1.95, ***.455***	1.89, ***.455***	1.89, ***.455***	

[a]Sulfate: usually based on 75% sulfuric acid solution (MIRAGE data are based on ammonium sulfate).

Table 6. Comparison of Radiative Transfer Schemes: Choices of Models for Spectral Resolution and Method[a]

	Micrometers	EC	GO	MI	GI	CC	Gr	UL
visible	.2–.7	1 (sp-t)	1 + 7 (sp-a)	9 (sp-t)	1(sp-a)	7 (sp-a)	4 (sp)	(sp)*
near-IR	.7–4	1 (sp-t)	3 (sp-a)	10 (sp-t)	1(sp-a)	1 (sp-a)	5 (sp)	(sp)*
far-IR	4–50	6 (sp)	10 (sp-a)	1 (10 μm)	4(sp-a)	10 (sp-t)	14 (sp)	(em)*

[a]Here, sp, spectral sub-bands; em, emissivity approach; −a, adding doubling; −t, two-stream; asterisk, external option.

mass, and that smaller black carbon sizes (compared to organic carbon) have a reduced impact on total carbon properties toward longer wavelengths. Thus good estimates for the absorption properties of organic carbon matter and are needed.

[36] At far-infrared wavelength, the choices for refractive indices are usually less important, because of a lack in extinction and in temperature contrast to the ground. Choices, however, are important for elevated larger aerosol sizes. This mainly applies to dust. Yet with respect to dust many uncertainties regarding their composition and associated infrared absorption features remain [*Sokolik and Toon*, 1999].

2.1.4. Toward Radiative Forcing

[37] To relate aerosol properties to climate, simulations with spectral broadband radiative transfer methods are performed. Necessary input data, in terms of aerosol properties, are (type combined) measures for amount (optical depth), absorption (single scattering albedos) and scattering behavior (phase-function) as function of wavelength. Radiative transfer is well understood, and scheme-related errors should be small. However, time-efficiency requirements in global models (evaluation at each grid point in frequent time steps) require simplifications to the radiative transfer method and more importantly to the spectral resolution. These approximations can compromise prior modeling efforts. Table 6 provides an overview of the number of assumed spectral bands and the adopted radiative transfer method.

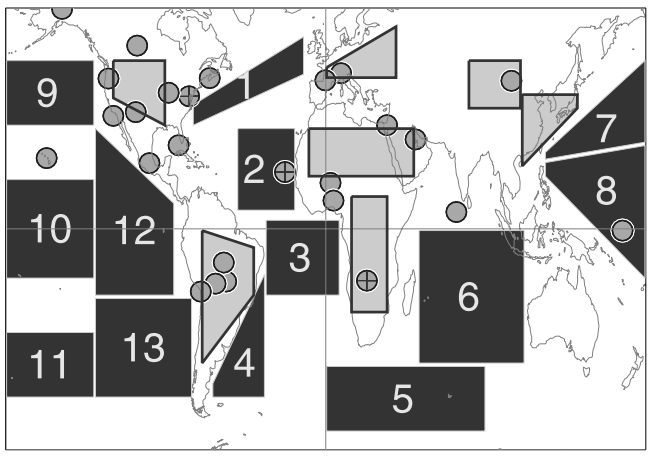

Figure 2. Location of selected regions and AERONET sites for model evaluations. Data at three AERONET sites are investigated in more detail. These sites are marked by a cross: GSFC (USA), Capo_Verde (off Africa) and Mongu (southern Africa). See color version of this figure in the HTML.

[38] Rather than judging radiative transfer choices of individual models, potential errors from common simplifications are explored for different aerosol types. As to relate to the climate-predicting nature of these models, results of sensitivity studies over cloud-free ocean scenes are expressed in 'cooling' or 'warming' (these are terms that capture the changes to the radiative net-flux at the top of the atmosphere, where energy gain to the Earth-atmosphere system is referred to as 'warming' and an energy loss as 'cooling'). With respect to the radiative transfer method, the use of the widely used two-stream scattering approximation tends to overestimate (solar) cooling by about 5%. Common spectral simplifications can even lead to larger errors. For example, a solar two-band approach (with 1 visible band (0.55 μm) and 1 near-IR band (1.6 μm)) largely ignores the solar spectral variability of aerosol properties. This leads to an underestimate of (solar) cooling by about 15% for dust and by about 25% for biomass and urban aerosol. Another common simplification is the neglect of aerosol forcing in the far-IR. While this may be justifiable for near surface aerosol (e.g., urban pollution), the effect of (IR) warming is nonnegligible if aerosol is elevated (e.g., biomass and dust) and characteristic aerosol sizes exceed 1 μm in size (e.g., dust). The neglect of IR (greenhouse)-effects for dust can introduce errors comparable in magnitude (though opposite in sign) to that of a solar two-band approximation. In summary, simplifications of current radiative transfer schemes can easily lead to forcing errors on the order of 20%.

2.1.5. Summary

[39] All four modeling steps (see Figure 1) are potential sources for errors. The largest uncertainties are associated with the initial two steps (initialization and aerosol processing for mass fields), because of complex assumptions and parameterizations, which were not examined in this study. In contrast, model differences during the last two modeling steps (mass to optical depth conversions and radiative transfer calculations) result from assumptions or simplifications that can be tested. Particularly useful is an understanding of conversion biases, because models are usually evaluated in comparisons to optical depth. Critical aerosol

Table 7. Classification for Regions of Figure 2 by Type and Source Strength

Class	Regions in Figure 2
Urban sources	E. Europe, E. Asia
Urban outflow	regions **1**, **7** and **9**
Dust sources	N. Africa, Asia
Dust outflow	region **2**
Biomass sources	Africa, S. America
Biomass outflow	regions **3**, **4** and **8**
Remote, tropical	regions **6** and **10**
Remote, S. Hemis.	regions **5** and **11**
Unclassified	regions **12** and **13**, N. America

properties for the mass conversion are the prescribed ambient relative humidity and assumptions to aerosol size, humidification, density and composition. Although aerosol assumptions of all tested models were presented in Tables 2–5, firm conclusions on biases are not possible, without data on ambient relative humidity fields and relative weights for sizes classes of multibinned aerosol types. This illustrates the need for additional model output (water uptake) and for control runs (e.g., prescribing identical ambient relative humidity fields for size swelling) in future model evaluation efforts. Nonetheless, demonstrated dependencies and listed model assumptions provide a useful background for the understanding of differences among models, when effective mass conversions are derived (below) from simulated mass and optical depth data for each aerosol type on a regional and seasonal basis.

2.2. Simulated Monthly Averages

[40] The evaluation of general model tendencies is based on monthly averages. Individually for each aerosol type, model results are compared. Comparisons focus on aerosol mass and aerosol optical depth, intermediate properties in global aerosol forcing simulations. Combining both properties and also conversions of mass into optical depth are explored. In addition, compositional mixture and absorption are addressed.

[41] Comparisons are conducted on a regional basis. These regions are small enough to accommodate distinct differences in sources and transport but large enough minimize effects from differences in spatial resolution (of models). The regional choices include 13 ocean regions and the 7 land regions. All regions plus locations of 20 Aerosol Robotic Network (AERONET) ground sites with yearlong aerosol statistics are displayed in Figure 2.

[42] The huge number of comparisons (each month, each aerosol type, each regions and different properties) necessitated a more compact approach. Therefore simulated monthly averages are summarized by ''yearly average'' and ''seasonality''. Seasonality is defined as the yearly range of the three-month running mean relative to the yearly average $[(avg_{3mo\_MAX} - avg_{3mo\_MIN})/(\Sigma\ avg_{mo}/12)]$. In addition, regions of Figure 2 were combined according to dominant aerosol type (urban, dust or biomass) and according to source distance, as outlined in Table 7.

[43] For the eight regional aerosol classes of Table 7 yearly average and seasonality were compared for aerosol mass, aerosol optical depth and mass extinction efficiency. Model tendency were identified for each aerosol type by comparing individual model simulations to that of the median model (the model ranked fourth among the seven models).

2.2.1. Aerosol Mass

[44] All models display the expected decrease in aerosol mass from sources toward remote regions. However, there are differences in source strength, in decay rate (toward remote regions) and in seasonality among the seven models. Mass simulations of all seven models are displayed in Figure 3 and quantified in Table 8. Table 8 also identifies models with extreme behavior, and uncommon model tendencies are summarized in Figure 4. Figure 3 also illustrates that for yearly averages the variability from simulations for three different years with the same model is small compared to differences (disk size in Figure 3) among models. Thus, to explain model differences, the choice of meteorological data appears of secondary importance.

[45] Despite some common general trends, mass differences among models are large. Not only type-combined totals (disk sizes in Figure 3) but also contributions of individual aerosol types (pie sections of disks in Figure 3) vary, when comparing simulated mass of different models for the same region. Models with extreme mass simulations are identified for each aerosol class and each aerosol type in Table 8 for yearly average and for seasonality strength. For more detailed information on mass simulations, the individual model values (yearly average, seasonality strength and seasonality phase) for each of the 20 regions of Figure 2 are compared in Appendix B. To simplify a comparison of the yearly average medians among aerosol types, the average compositional mixture aerosol class is summarized in Table 9, which also shows mass ratios between organic and black carbon.

[46] Model simulations identify dust and sea salt as leading contributors to aerosol mass, which at least in part reflects their relative large particles sizes ($m \sim r^3$). Over continents dust dominates by mass. Even for urban and biomass source regions dust mass matches the combined mass contributions from carbon and sulfate. Over oceans, sea salt usually dominates by mass, except for dust outflow regions (e.g., west off Africa). As yearly averages and seasonality for dust and sea salt display higher variability than for other aerosol types, the large differences in simulated total mass among models are not surprising.

[47] Larger differences are also found for simulated carbon mass away from urban sources. Although carbon is less important in terms of total mass, the mass ratio between organic and black carbon varies by almost one order of magnitude (GISS ~12 and Grantour ~1.5), even after excluding very large values in excess of 20 by the ULAQ model. Different choices for carbon sources are certainly a contributing factor as ob/bc ratios from biomass burning are usually larger than ratios from fossil fuel burning.

2.2.2. Aerosol Optical Depth

[48] Aerosol optical depth (or aerosol optical thickness, thus AOT) is derived from simulated aerosol mass fields. Thus a somewhat similar behavior is expected. However, while the decrease away from sources toward remote regions is maintained, there are differences, due to increased

Figure 3. (opposite) Simulated aerosol mass averaged for the regions of Figure 2. Yearly averages (disks) and seasonality (rings) of each model are presented. Over each region the size of disks or rings indicates the amount (according to the scale in the lower right), and the detail on disks or rings indicates fractional contributions by aerosol type (following the key in the upper right). Also shown is the impact of different meteorological data (1990, 1996, and 1997 simulations with the GOCART model) on the yearly average and a model composite with 4th-ranked aerosol component properties. See color version of this figure in the HTML.

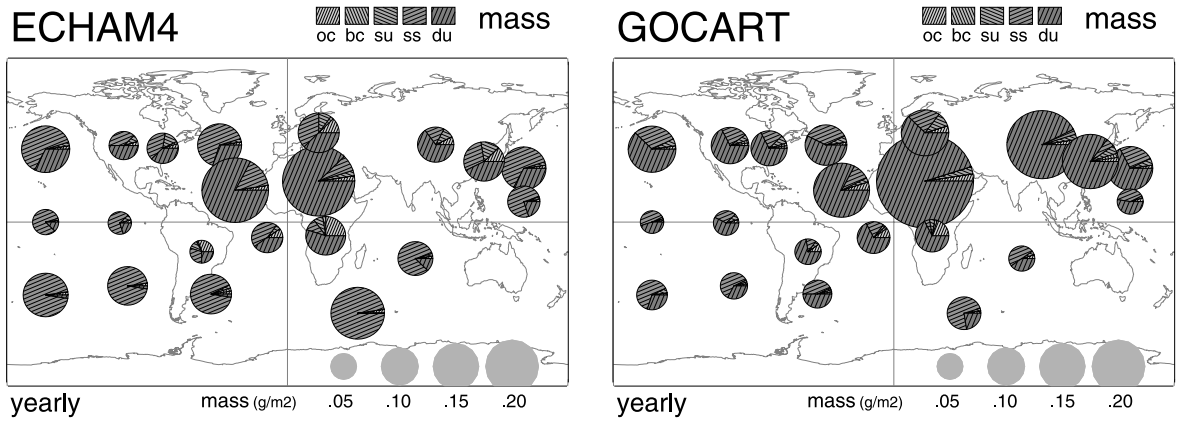
ECHAM4
oc bc su ss du
mass
yearly
mass (g/m2)
.05
.10
.15
.20

GOCART
oc bc su ss du
mass
yearly
mass (g/m2)
.05
.10
.15
.20

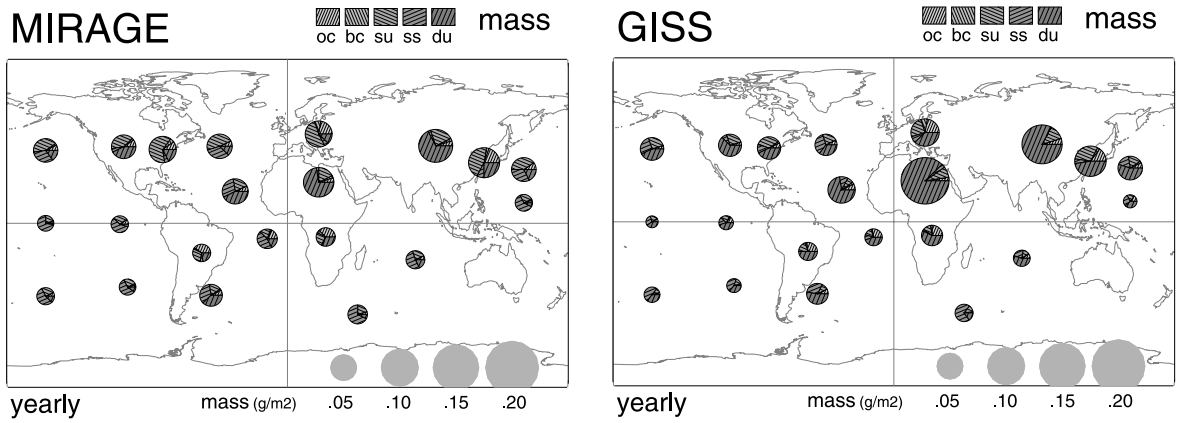
MIRAGE
oc bc su ss du
mass
yearly
mass (g/m2)
.05
.10
.15
.20

GISS
oc bc su ss du
mass
yearly
mass (g/m2)
.05
.10
.15
.20

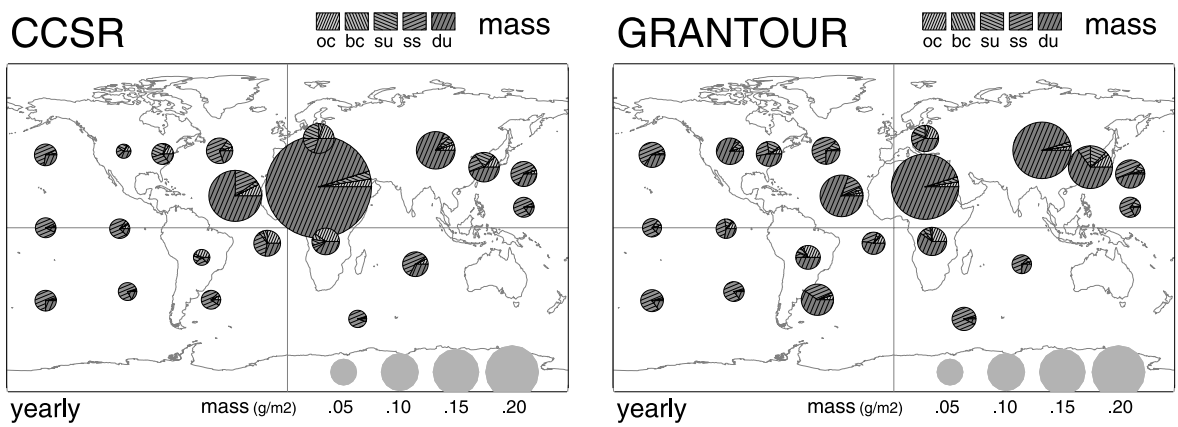
CCSR
oc bc su ss du
mass
yearly
mass (g/m2)
.05
.10
.15
.20

GRANTOUR
oc bc su ss du
mass
yearly
mass (g/m2)
.05
.10
.15
.20

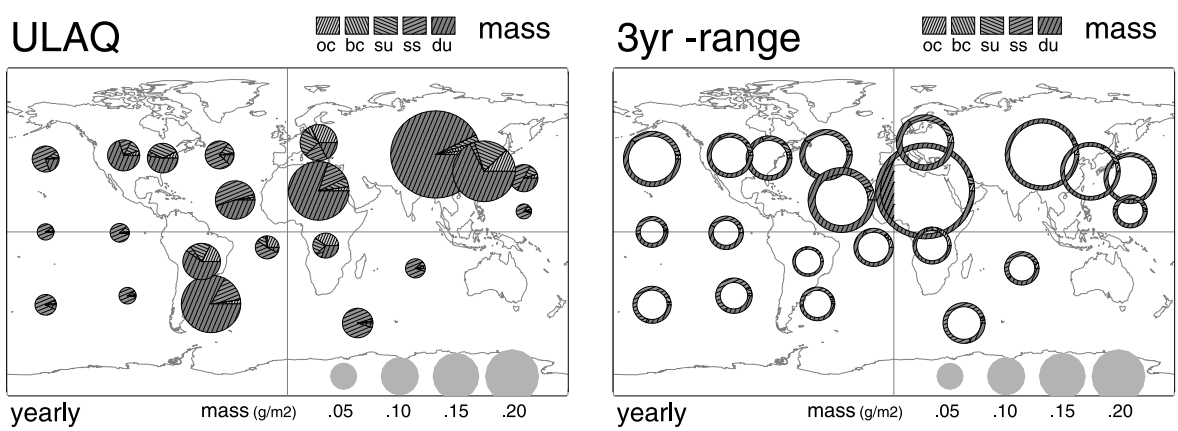
ULAQ
oc bc su ss du
mass
yearly
mass (g/m2)
.05
.10
.15
.20

3yr -range
oc bc su ss du
mass
yearly
mass (g/m2)
.05
.10
.15
.20

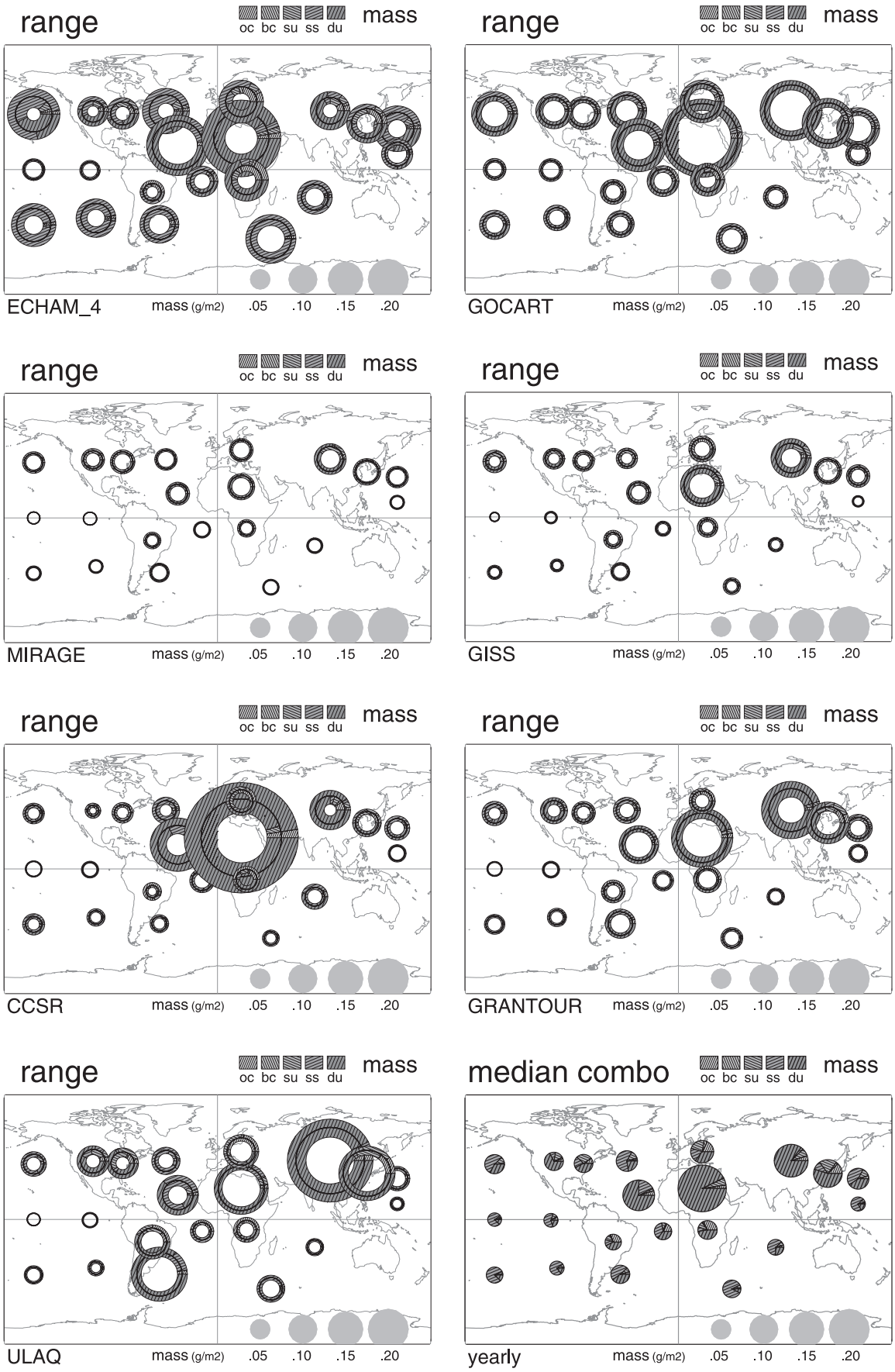

Figure 3. (continued)

Table 8. Simulated Component Mass: Values of the Median Model and Models With Extreme Tendencies[a]

	Yearly Average Component Mass, mg/m^2									
	OC		BC		SU		SS		DU	
	Avg.	Max/Min	Avg.	Max/Min	Avg.	Max/Min	Avg.	Max/Min	Avg.	Max/Min
Urban sources	9.8	***UL***/*GO*	2.3	***UL***	12.9	***UL, MI***	11.1	***EC, GO***/*GI, MI*	48.4	***GO, UL***/*MI*
Urban outflow	1.1	***MI, GI***	.4	*UL*	5.3	***MI***	28.2	***EC, GO***/*GI, MI*	16.9	***GO, EC***/*MI*
Dust sources	3.2	***UL***	.8		9.6	*Gr*	2.9	***UL, EC***/*MI*	253.	***GO, CC***/*MI, GI*
Dust outflow	2.9	***CC***/*UL*	.7	*UL, GI*	3.2	***MI***	17.6	***UL, EC***/*GI*	99.0	***EC, GO***/*MI, GI*
Biomass sources	13.3		1.5	***EC***	3.6	***UL, MI***	3.4	***EC***/*GI, MI*	26.7	***GO***/*MI, CC*
Biomass outflow	2.9	***CC***	.4	***CC***/*UL*	2.1	***MI***	17.1	***EC***/*GI*	14.8	***UL, GO***/*MI, CC*
Remote, tropics	1.0	*UL*	.1	***Gr, GO***/*UL*	1.8	***MI***	18.7	***EC***/*GI*	7.5	***GO***/*UL, MI*
Remote, S. Hemis.	.5	***MI, GO***/*Gr, UL*	.1	***GO, MI***/*UL, GI*	1.7	***MI***/*CC,Gr*	30.7	***EC, GO***/*GI, MI*	4.1	***GO***
	Seasonality for Component Mass									
	OC		BC		SU		SS		DU	
	Var	Max/Min	Var	Max/Min	Var	Max/Min	Var	Max/Min	Var	Max/Min
Urban sources	0.3	***GO***	.3		.8	***Gr***/*MI, CC*	1.3	*MI*	1.2	
Urban outflow	.7	*UL*	.5	***GO***	.5	***CC***	1.3	***EC***/*MI*	1.3	
Dust sources	.6	***EC***/*MI*	.5	***EC***/*UL*	1.0	***CC***/*MI*	.8	***GO, EC***	1.0	***EC***
Dust outflow	1.7		1.3	***MI***	.6	***CC****UL*	.8	*MI*	1.1	***UL***
Biomass sources	1.5		1.7		.3	***GO, EC***	.6	***MI***	1.0	***EC***
Biomass outflow	1.0	***UL***	1.2	***UL***	.3	***CC***	.3	***EC, GI***/*MI*	.7	***EC***
Remote, tropics	1.5	*MI*	1.2	***UL***	.4	*MI*	.5	***EC***/*MI*	1.0	***CC***/*Gr*
Remote, S. Hemis.	1.5		1.4		.9	*GO, UL*	.7	*MI*	1.2	***CC***/*GI*

[a]For class-combined regions (see Table 7), yearly averages (Avg) and seasonality (Var) of the median model (4th-ranked among all models) are presented. Seasonality is the ratio of the 3-month running mean range during a year and the yearly average. In addition, models are displayed whose values for Avg or Var exceed (italic-bold) or fail (italic) that of the median model by more than 50%.

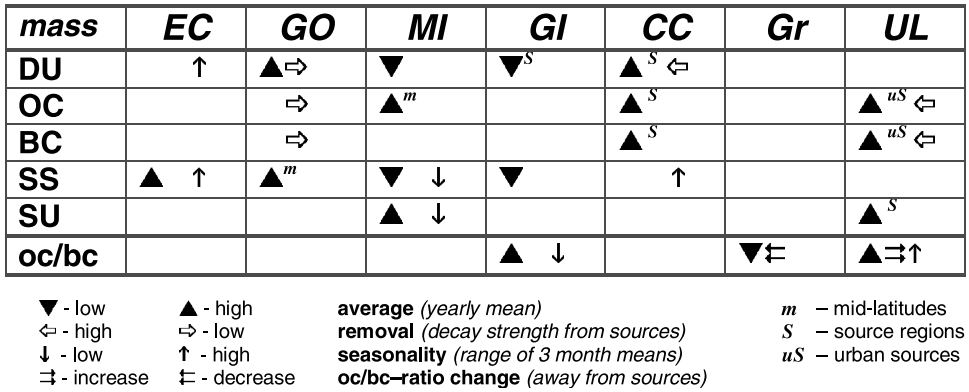

Figure 4. Component aerosol mass tendencies with respect to the median model.

Table 9. Simulated Fractional Component Contributions to Aerosol Mass, oc/bc Mass Ratios, and Models With Extreme Tendencies[a]

	Mass									
	OC + BC		SU		SS		DU			
	Percent	Max Model	Percent	Max Model	Percent	Max Model	Percent	Max Model	oc/bc Ratio	oc/bc Ratio Max/Min Models
Urban sources	17	***MI***	22	***MI***	15	***EC***	46	***GO***	4	***MI***/*GO*
Urban outflow	4	***MI***	14	***MI***	48	***EC***	34	***GO***	4.5	***GI***/*Gr*
Dust sources	3	***MI***	7	***MI***	4	***EC***	86	***GO***	4.5	***MI***/*Gr*
Dust outflow	4	***MI***	6	***MI***	20	***UL***	70	***EC***	6.5	***GI***/*Gr*
Biomass sources	31	***CC***	13	***MI***	9	***Gr***	47	***GO***	⟨10⟩	***MI***/*GO*
Biomass outflow	9	***GI***	8	***MI***	47	***CC***	36	***GO***	⟨8⟩	***GI***/*Gr*
Remote, tropics	4	***GI***	9	***MI***	64	***UL***	25	***GI***	7	***GI***/*Gr*
Remote, S. Hemis.	2	***GI***	7	***MI***	77	***EC***	14	***GO***	7	***GI***/*Gr*

[a]For class-combined regions (see Table 7), yearly averages of aerosol component fractional contributions (in percent) and of oc/bc mass ratios are presented. In addition, models with the largest fractional contribution (italic-bold) and models with the largest (italic-bold) and smallest (italic) oc/bc mass ratio are listed. Very high oc/bc ratios of the ULAQ models (caused by strong BC removal) were ignored.

contributions from smaller sized aerosol types (e.g., sulfate and carbon) and due to influences of ambient moisture on size. Adopted size for each aerosol type is also the main modulator of how efficiently mass is converted into optical depth. Thus optical depth tendencies for source strength, decay rate and seasonality will not always match those for aerosol mass. Aerosol optical depth simulations of all seven models are displayed in Figure 5 and quantified in Table 10. Table 10 also identifies models with extreme behavior, and uncommon model tendencies are summarized in Figure 6. Figure 5 also illustrates that for yearly averages the variability from simulations for three different years with the same model is small compared to differences (disk size in Figure 5) among models.

[49] Amount (disk size in Figure 5) and compositional mixture (pie-sections in Figure 5) of regionally averaged aerosol optical depths indicate that fractional contribution of carbon and sulfate now become comparable to dust and sea salt and at times even dominate. With quite different aerosol type contributions to the total optical depth, model differences are much larger than a comparison of total optical depth might have suggested (many models can be identified by their dominant aerosol type). Optical depth comparisons for individual aerosol types in Table 10 indicate that simulations are least agreeable for dust and sea salt and that model differences are usually larger away from sources, as transport and processing issues become more important. For more detailed information on aerosol optical depths simulations, the values of individual models (yearly average, seasonality strength and seasonality phase) for each of the 20 regions of Figure 2 are compared in Appendix B. Again, to simplify a comparison of the yearly average medians among aerosol types the average compositional mixture for each aerosol class is summarized in Table 11. Table 11 also identifies model biases toward any aerosol type by indicating models with the highest and smallest contributions for each class region.

[50] Each of the four aerosol types (carbon (= oc + bc), sulfate, sea salt and dust) can be dominant. Thus, except for sea salt over continents, none of these four aerosol types can be neglected in order to achieve accurate estimates for aerosol optical depths.

[51] None of the four aerosol types exceeds on a model median and yearly average basis contributions of 60% to the total optical depth for any class region. This makes it very difficult to evaluate any individual aerosol type via (type-combined) column measurements (e.g., satellite), except for particular seasons, when dominant type contributions are significantly higher (e.g., carbon near tropical sources during the biomass burning season).

[52] Models agree better on source location than on source strength or transport. A more detailed analysis for (visible) aerosol optical depth partitioning differences is given in Appendix B. Summarizing those comparisons, models agree on dominant carbon for central Africa and South America, high sulfate and carbon in and off Europe and East Asia, dominant sea salt in midlatitudes of the Southern Hemisphere and dominant dust over central Asia and Northern Africa. The largest disagreements among models are found for source strength of dust and biomass burning, sea salt over tropical oceans, carbon over tropical and Southern Hemispheric oceans and dust in off-source regions, where the ladder two are largely related to transport.

2.2.3. Single-Scattering Albedo

[53] The single-scattering albedo ω_0 determines how much of attenuated radiation (attenuated because of an interaction between radiation and an atmospheric particles) is scattered. The remaining nonscattered fraction $(1 - \omega_0)$ multiplied with the optical depth τ is a measure for aerosol absorption. Thus the smaller the single-scattering albedo the larger is the potential for absorption. Particularly important is the value at visible wavelengths, where most of the interaction between sunlight and aerosol occurs. Relative tendencies for the single-scattering albedo ω_0 of five models (not absorption) are summarized in Figure 7.

[54] Only four of the seven model provided data. However, their differences for single-scattering already are significant (a sample will be provided in the comparison section). ECHAM4 suggest relative strong absorption, whereas the absorption suggested by MIRAGE and especially ULAQ is relatively weak. An explanation is difficult because underlying assumptions are incomplete (e.g., permitted water uptake).

2.2.4. Mass Extinction Efficiency

[55] Model tendencies for the conversion of mass into optical depth must be understood for any meaningful evaluation of aerosol source choices and aerosol processing from comparisons to aerosol optical depth. A determination of mass extinction efficiencies (mee) from theoretical assumptions failed because of incomplete data (e.g., size-distribution, water-uptake and ambient relative humidity). However, an effective conversion can be determined from the ratio of simulated optical depth and (dry-) mass for each aerosol type. A quick overview on relative model tendencies for mass to optical depth conversions is given in Figure 8.

[56] The magnitude of mass extinction efficiencies varies among aerosol types. Conversions for carbon and sulfate are on the order of 10 m^2/g, whereas conversion for dust and sea salt are on the order of 1 m^2/g.

[57] Regional differences on a yearly and model average basis are presented in Figure 9. Also given, as a model composite of Figures 3 and 5, are regional averages for aerosol mass and aerosol optical depth, indicating that a mass domination by dust and sea salt does not always lead to a domination in terms of optical depth. Details on model tendencies for mass extinction efficiencies of aerosol types on a regional basis are illustrated in Figure 10 and quantified in Table 12.

Figure 5. (opposite) Simulated aerosol optical depth averaged for the regions of Figure 2. Yearly averages (disks) and seasonality (rings) of each model are presented. Over each region the size of disks or rings indicates the amount (according to the scale in the lower right), and the detail on disks or rings indicates fractional contributions by aerosol type (following the key in the upper right). Also shown is the impact of different meteorological data (1990, 1996, and 1997 simulations with the GOCART model) on the yearly average and a model composite with 4th-ranked aerosol component properties. See color version of this figure in the HTML.

ECHAM4

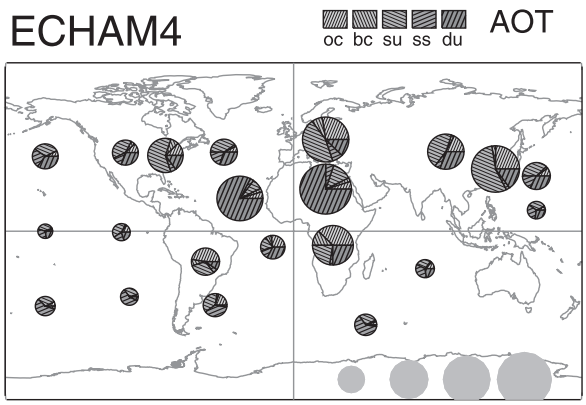

GOCART

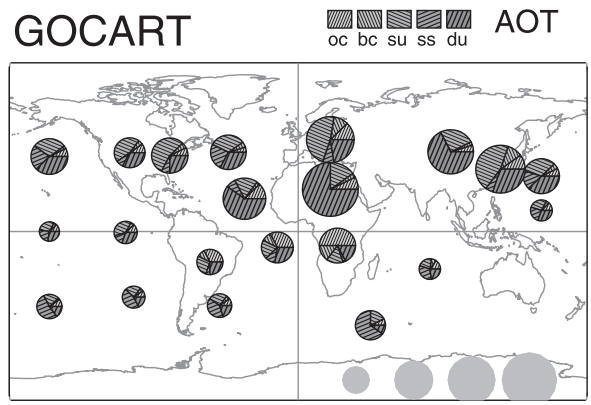

MIRAGE

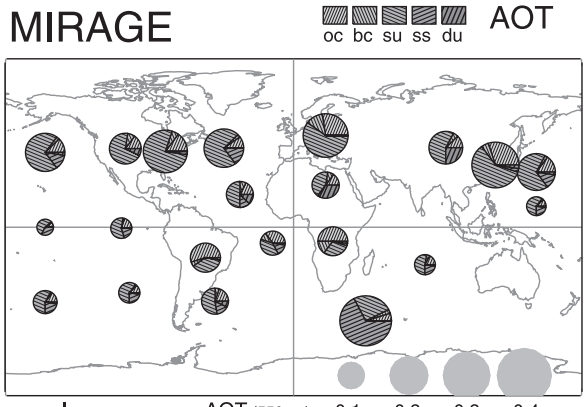

GISS

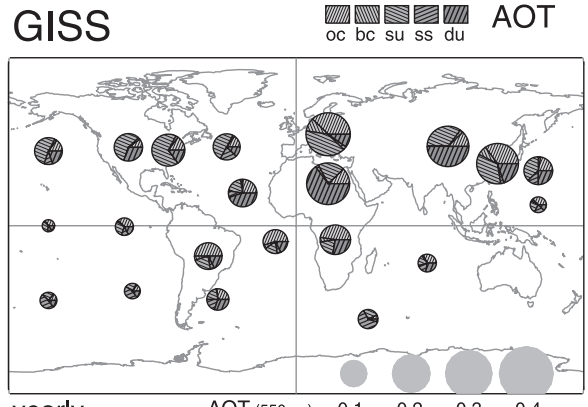

CCSR

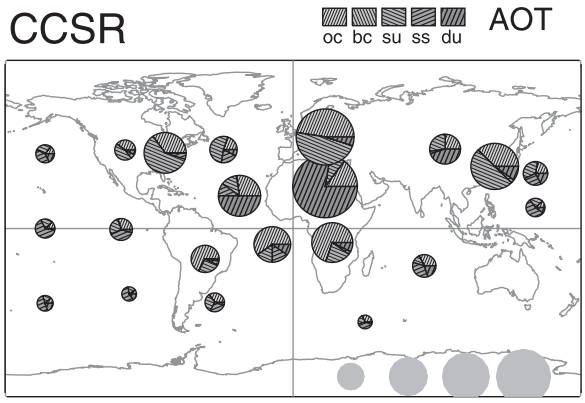

Grantour

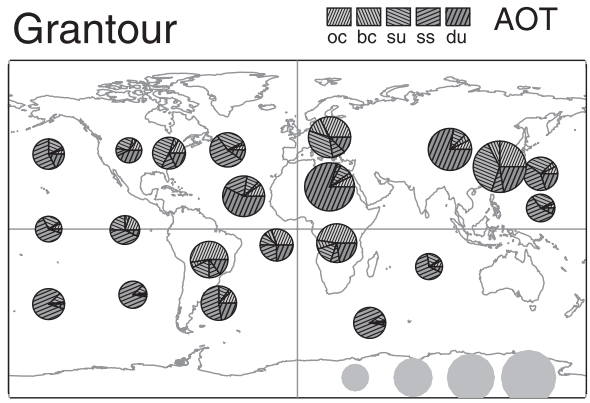

ULAQ

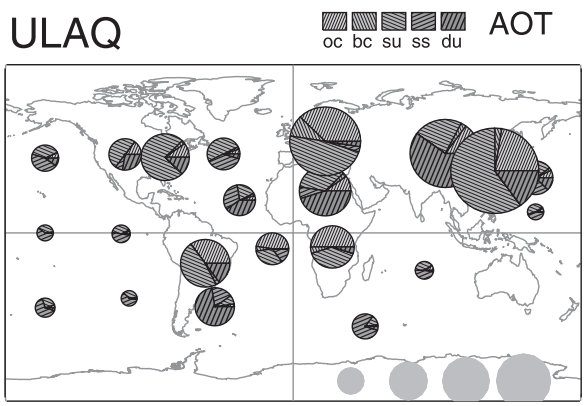

3yr -range

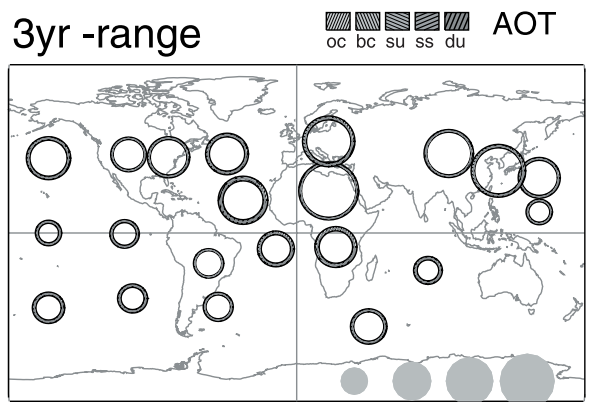

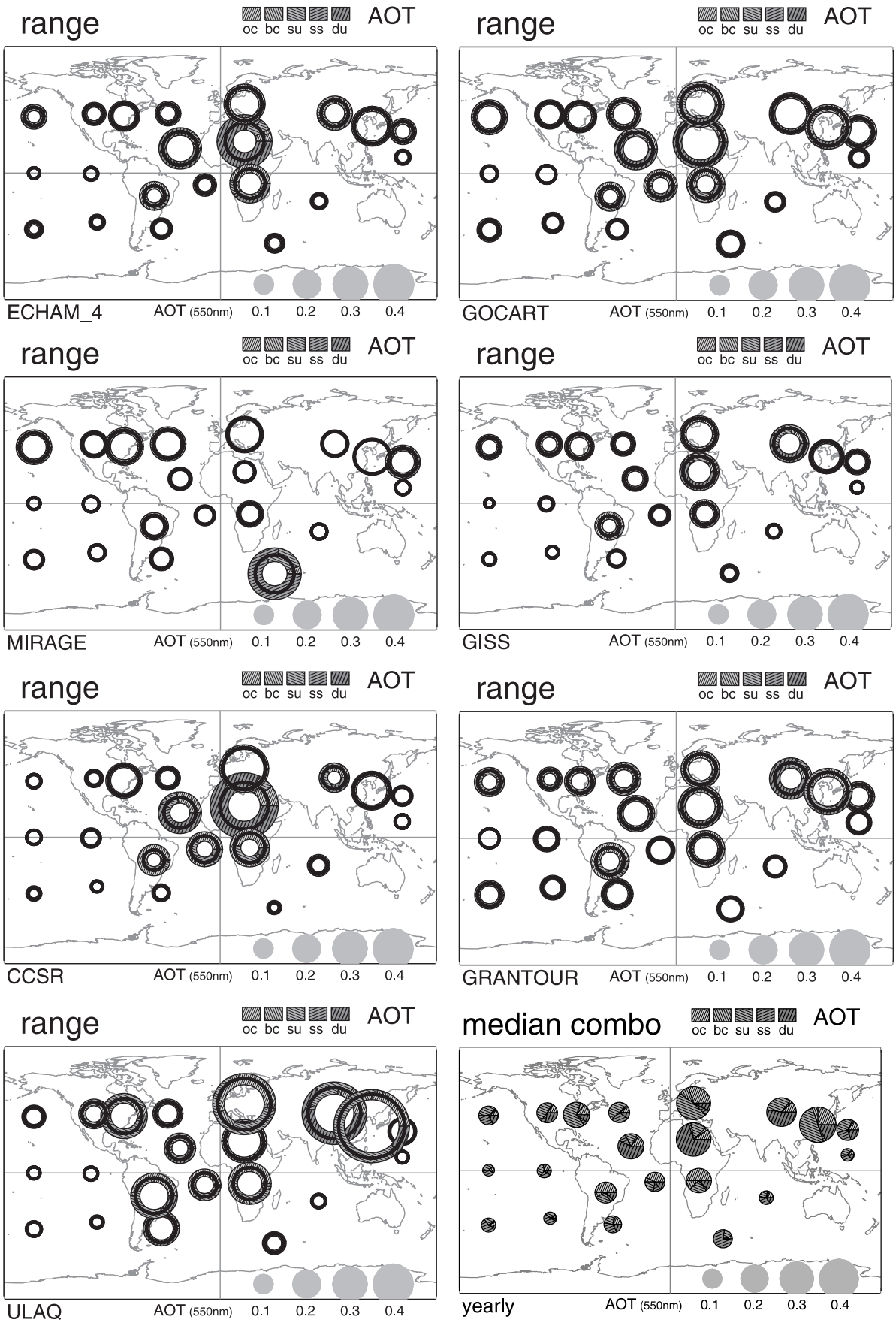

Figure 5. (continued)

Table 10. Simulated Aerosol Optical Depth: Values of the Median Model and Models With Extreme Tendencies[a]

	Yearly Average Component Aerosol Optical Thickness									
	OC		BC		SU		SS		DU	
	Avg.	Max/Min	Avg.	Max/Min	Avg.	Max/Min	Avg.	Max/Min	Avg.	Max/Min
Urban sources	.073	***UL, CC***/*GO*	.025	***UL***	.158	***UL***	.010	***Gr***/*MI*	.045	***GO, UL***/*MI*
Urban outflow	.011	***MI***	.003	***GO, MI***/*UL*	.044	***MI***	.028	***Gr, UL***/*GI*	0.22	***GO***/*MI, CC*
Dust sources	.020	***UL***	.007		.058	***UL***/*Gr*	.003	***UL, EC***/*MI*	.218	*MI*
Dust outflow	.021	*EC*	.006	***GO***/*UL*	.023	***MI, GO***	.014	***Gr, UL***/*EC*	.127	***EC***/*MI, GI*
Biomass sources	.065	***UL, CC***	.025	***UL***	.026	***UL***	.004	***Gr***/*MI*	.028	*MI, CC*
Biomass outflow	.022	***CC***/*EC*	.003	***GO, Gr***	.020	***MI***	.019	***Gr***/*GI*	.015	***UL, Gr***/*MI, CC*
Remote, tropics	.006	***CC***/*UL*	.001	***MI, GO***/*UL*	.014	***MI***	.016	***Gr***/*GI*	.008	***GO***/*UL, MI*
Remote, S. Hemis.	.004	***MI, GO***/*UL, Gr*	.001	***GO, Gr***/*UL*	.012	***MI***/*CC*	.050	***MI, Gr***/*CC, GI*	.005	***GO***/*MI*
	Seasonality for Component Aerosol Optical Thickness									
	OC		BC		SU		SS		DU	
	Var	Max/Min	Var	Max/Min	Var	Max/Min	Var	Max/Min	Var	Max/Min
Urban sources	.4	***GO***/*MI, UL*	.3		.4	***Gr, UL***	1.3	*MI*	1.2	
Urban outflow	.7	***GO***/*UL*	.6	***GO***/*UL*	.5	***CC***	1.4	***MI***/*CC*	1.3	
Dust sources	.7	*MI*	.4	***EC***	1.0	*MI*	.9	***GO, EC***	1.0	***EC***
Dust outflow	1.5	*UL, GI*	1.5		.7	***CC***/*MI*	.7	*CC, MI*	1.1	***UL***
Biomass sources	1.5	*MI*	1.5		.4		.6	***EC***	1.0	***EC***
Biomass outflow	1.0	***UL***	.9	***UL***	.3		.2	***EC***	.7	***EC***
Remote, tropics	1.3	*MI*	1.1	***UL***	.3		.4	***MI***/*CC*	1.0	***CC***/*Gr*
Remote, S. Hemis.	1.6		1.6		.9	***Gr***/*GO*	.9	***MI***/*GI, UL*	1.2	***CC***/*GI*

[a]For class-combined regions (see Table 7), yearly averages (Avg) and seasonality (Var) of the median model (4th-ranked among all models) are presented. Seasonality is the ratio of the 3-month running mean range during a year and the yearly average. In addition, models are displayed whose values for Avg or Var exceed (italic-bold) or fail (italic) that of the median model by more than 50%.

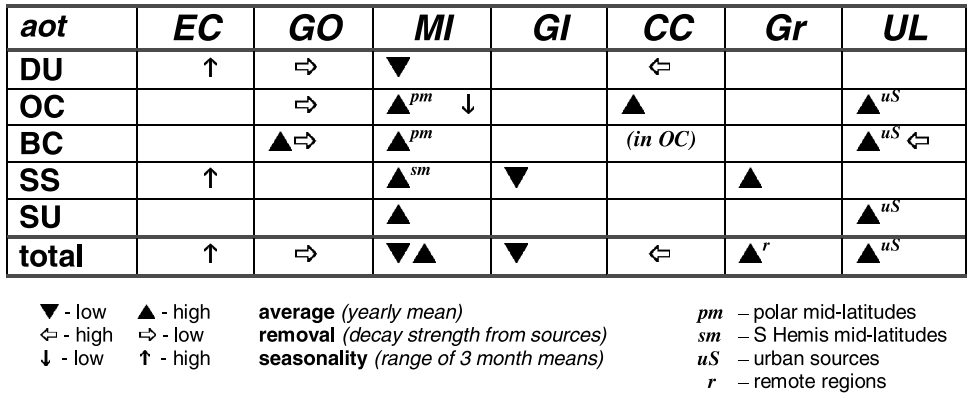

Figure 6. Component aerosol optical depth tendencies with respect to the median model.

Table 11. Simulated Fractional Component Contributions to Aerosol Optical Depth and Models With Extreme Tendencies[a]

	Aerosol Optical Thickness									
	OC		BC		SU		SS		DU	
	Percent	Max/Min	Percent	Max/Min	Percent	Max/Min	Percent	Max/Min	Percent	Max/Min
Urban sources	28	***CC***/*GO*	7	***Gr***/*EC*	47	***MI***/*Gr*	4	***Gr***/*MI*	14	***GO***/*MI*
Urban outflow	10	***CC***/*Gr*	2	***GO***/*UL*	42	***MI***/*Gr*	27	***Gr***/*GI*	19	***GO***/*MI*
Dust sources	11	***CC***/*UL*	3	***MI***/*UL*	25	***MI***/*Gr*	2	***EC***/*MI*	59	***Gr***/*MI*
Dust outflow	14	***CC***/*EC*	3	***MI***/*UL*	19	***MI***/*EC*	13	***UL***/*EC*	51	***EC***/*MI*
Biomass sources	48	***CC***/*UL*	7	***GO***/*UL*	27	***UL***/*Gr*	3	***Gr***/*MI*	15	***GI***/*MI*
Biomass outflow	23	***GI***/*Gr*	3	***GO***/*UL*	28	***MI***/*Gr*	26	***Gr***/*GI*	19	***GO***/*MI*
Remote, tropics	14	***GI***/*UL*	3	***GO***/*UL*	31	***MI***/*CC*	38	***Gr***/*GI*	14	***GO***/*UL*
Remote, S. Hemis.	8	***CC***/*Gr*	1	***GO***/*UL*	23	***MI***/*Gr*	60	***Gr***/*MI*	8	***CC***/*MI*

[a]For class-combined regions (see Table 7), yearly averages of aerosol component fractional contributions (in percent) are presented. In addition, models with the largest (italic-bold) and smallest (italic) fractional contribution are listed.

ssa (ω_0)	EC	GO	MI	GI	CC	Gr	UL
urban	▼ ↑		▲	---		---	▲
dust	▼	↑	▲ ↑	---	↑	---	▲
biomass	▼ ↑		↑	---		---	
remote	▼	↑		---		---	▲ ↓

▼ - low ▲ - high **average** *(yearly mean)* --- no data given
↓ - low ↑ - high **seasonality** *(range of 3 month means)*

Figure 7. Aerosol single scattering albedo tendencies with respect to the median model.

[58] Mass extinction efficiencies for sulfate, sea salt and organic carbon are higher at midlatitudes. This can be explained by on average higher ambient relative humidities. Mass extinction efficiencies for dust are smallest near dust sources, because of the presence of larger aerosol, which is otherwise lost to gravity.

[59] Differences among models for the mass extinction efficiency are largest for sea salt. Surprisingly large are also differences for dust, since mass conversions are not affected by the ambient moisture. The seasonality for mass extinction efficiency is weak compared to that of mass and optical depth. Seasonality differences among models are largely limited to hydrophilic aerosol, especially at higher latitudes, and therefore most likely caused by differences in the relative humidity fields.

[60] The large disagreement for the mass extinction efficiencies of any aerosol type is disturbing. A close agreement is highly desirable, as to avoid biases for derived component aerosol optical depths. As of now, many models have relatively large conversions for one type and relatively small conversions for another type. Thus there is a danger that type-combined totals of optical depth often appear in better agreement to measurements (e.g., satellites) than they should (as biases of different aerosol types offset each other). Tools for constraints on mass conversions are now becoming available with size-information from remote sensing data by satellites (e.g., Angstrom parameter) or ground data (e.g., AERONET size-distributions). Another possibility to avoid conversions biases at least for dust and sea salt is a direct comparison of aerosol ('wet') mass with column size-distribution retrievals from AERONET.

2.2.5. Summary

[61] The intercomparison of models revealed many differences for simulated mass and optical depth. With many opposing (thus partially offsetting) trends for different aerosol types, differences among models were often much larger than a comparison of (aerosol type-combined) totals would have suggested. In an effort to provide a quick overview of the peculiarities of particular models, unusual tendencies are summarized in Figure 11. For yearly average and seasonality of aerosol optical depth and aerosol mass, following the regional classification of Table 2, model deviations in excess of 30% with respect to the median (or fourth-ranked) model and with respect to MODIS retrievals (introduced later) are summarized. In addition, the most unusual overall model tendencies and tendencies on a component basis are as follows:

[62] 1. ECHAM4 has high MASS and AOT for dust, especially in spring near the Azores. Uncommon model behaviors by component are (a) for sulfate: high mass and seasonality, low mee; (b) for dust: strong (out of phase) seasonality for mass and aot; (c) for sea-salt: high mass, very low mee (size overestimate), low aot; (d) for carbon: low mee.

[63] 2. GOCART has strong transport (or weak removal). Uncommon model behaviors by component are (a) for sulfate: dust: high mass, lower mee; (b) for sea-salt: high mass at high latitudes; (c) for carbon: high bc-mee and bc-aot, low urban mass and aot, low oc/bc ratio.

[64] 3. MIRAGE has very strong NH sulfate MASS and AOT and weak tropical sources. Uncommon model behaviors by component are (a) for sulfate: high mass and high aot (esp. in NH); (b) for dust: low mass, mee and aot, weak seasonality; (c) for sea-salt: low mass, high mee seasonality; (d) for carbon: high mass and aot at higher latitudes, low in the tropics.

[65] 4. GISS has low MASS and AOT, except for sulfate. Uncommon model behaviors by component are (a) for sulfate: low mee but strong mee-seasonality; (b) for dust: low source mass is offset by high mee; (c) for sea-salt: low mass, high mee but still low aot; (d) for carbon: low mass, low aot.

[66] 5. CCSR has strong sources for dust and carbon but a weak transport. Uncommon model behaviors by component are (a) for sulfate: strong mee; (b) for dust: high source mass, weak transport, strong seasonality; (c) for sea-salt: strong seasonality for mass; (d) for carbon: high source mass, high mee and aot, weak transport, low oc/bc ratio.

[67] 6. Grantour has the strongest (sea-salt) AOT in remote regions. Uncommon model behaviors by component are (a) for sea-salt: high mee, high aot; (b) for carbon: high mass and aot in urban regions, very low oc/bc ratio.

[68] 7. ULAQ has strong MASS and AOT for sulfate and carbon near (urban) sources, transport is weak. Uncommon model behaviors by component are (a) for sulfate: high mass and aot near sources; (b) for dust: weak mee seasonality; (c) for sea-salt: weak mee seasonality; (d) for carbon: high urban mass and aot, weak transport, oc/bc ratio that is very large away from sources (fast bc removal).

[69] On a final note, it should be emphasized that uncommon tendencies or the lack of them (among models) are not a measure of modeling skill. Model skill can only be determined in comparisons to quality data.

3. Comparisons

[70] To evaluate models on an absolute scale the agreement of simulated aerosol properties to measurements was explored. The data had to cover an entire year to address seasonality issues, although multiyear data sets were pre-

mee	EC	GO	MI	GI	CC	Gr	UL
DU			▼	▲^{S}			↓
OC	▼ ↑			↓	▲		↓
BC	▼ ↓		↑	↓	*(in OC)*		
SS	▼		↑	▲ ↓		▲	↓
SU				▼ ↑	▲		

▼ - low ▲ - high **average** *(yearly mean)* *S* - source regions
↓ - low ↑ - high **seasonality** *(range of 3 month means)*

Figure 8. Component aerosol mass extinction efficiencies with respect to the median model.

ferred to minimize biases from a particular year. Only monthly or seasonal statistics were compared in order to minimize sampling biases of data sets. The compared aerosol property is primarily the mid-visible aerosol optical depth. Easily imagined (it captures the aerosol impact on the attenuation of direct sunlight), it is one of the standard retrieved aerosol properties in remote sensing. Remote sensing measurements from ground (AERONET) and space (AVHRR, TOMS, MODIS) are used. Their retrieved aerosol properties, however, are vertically (column-) integrated and type-combined. Thus evaluations of particular aerosol types will be largely limited to regions or seasons, where these aerosol types dominate. With currently diverse assumptions for size and water uptake among models, conclusions on aerosol source strength and processing from optical depth comparisons will be limited. Next, the measurement data sets are always introduced first before comparisons to model simulation are presented.

3.1. AERONET

[71] AERONET is a federated worldwide network of CIMEL sun-/sky-photometers that are monitored and maintained at the NASA-Goddard Space-Flight Center [*Holben et al.*, 1998]. Data have been collected since 1993. The sun-/sky-photometers have a 1.2 degree field of view and sample sequentially at (up to) eight solar spectral subbands (.34, .38, .44, .50, .67, .87, .94 and 1.02 μm). Weather and instrument status permitting, up to 50 attenuation (4/hr) and 10 sky-radiance (1/hr) measurements can be taken during a day.

[72] Attenuation measurements of direct sunlight are always repeated twice (three consecutive measurements) for quality purposes. Sharp discontinuities among triplet data and among consecutive triplet averages indicate poor or cloud-contaminated data, which were removed in 'quality controlled' attenuation data sets [*Smirnov et al.*, 2000].

[73] Sky-radiance measurements involve an upward solar principal scan and a complete azimuthal scan. The added information from the scanning modes enables via radiative transfer inversion techniques [*Dubovik and King*, 2000; *Dubovik et al.*, 2000] usually reliable estimates for aerosol size-distribution, aerosol absorption and the presence of nonspherical shapes. Without a consistent quality algorithm in place only sky-radiance scans within minutes of 'quality controlled' attenuation data are considered.

3.1.1. Selected Sites

[74] Twenty AERONET sites were picked for local comparisons. The pick selection was based on aerosol type diversity and data volume. Table 13 summarizes the geographical coordinates, dominant aerosol type and data totals (prior to the year 2000). Particularly important is the number of quality sky data (Sky-g), because these data completely define the aerosol properties: absorption, size and optical depth.

[75] To better illustrate the derived AERONET properties [*Holben et al.*, 2000; *Dubovik et al.*, 2002], monthly statistics from three samples sites are introduced. These three sites, Goddard or GSFC, Cape Verde and Mongu are specially marked in Figure 2. GSFC located east of Washington, D. C., is dominated by urban aerosol, Cape Verde off the African west coast is dominated by dust aerosol and Mongu in central southern Africa, is dominated by biomass aerosol during the biomass burning season from July to November.

3.1.2. Sun Photometer Data

[76] Measurements of the direct attenuation of sunlight provide data on aerosol optical depth τ and Angstrom parameter α ('alpha-slope'). Averages for the three sample sites are compared in Figure 12.

[77] The aerosol optical depth τ at 0.55 μm wavelength (a measure for the attenuation of visible light) displays strong seasonal variations at all three sites: A strong maximum during the height of the biomass season from August to October in (subtropical and) tropical regions of the Southern Hemisphere (e.g., Mongu), early spring and mid-year summer maxima of Saharan dust outflow off western Africa (e.g., Cape Verde) and a summer maximum for urban(-industrial) areas of the Northern Hemisphere (e.g., GSFC or Goddard).

[78] The Angstrom parameter α captures the spectral change in optical depth, here between 0.44 μm and 0.87 μm wavelength. α is defined as the negative slope in a log {optical depth}/log {wavelength}-space. For the spectral region of the Sun photometer, the Angstrom parameter is sensitive to size of submicrometer aerosol. Values between 1.5 and 2.0 indicate particles sizes of the 'accumulation mode' with a few tenth of a micrometer in size. These aerosol sizes are characteristic for biomass-burning-dominated aerosol (July to November at Mongu) and urban influenced aerosol (GSFC) [*Eck et al.*, 1999]. Sites dominated by larger 'coarse mode' particles (e.g., dust at Cape Verde) display smaller Angstrom parameters. Values below 0.4 almost resemble the spectrally neutral behavior of clouds (thus are often a cause of mistaken identity in Angstrom based cloud-screens of aerosol retrievals).

[79] The variability during a month is much larger for τ than for α. Thus, only for the optical depth (in the upper panel of Figure 12), sectional averages of the probability

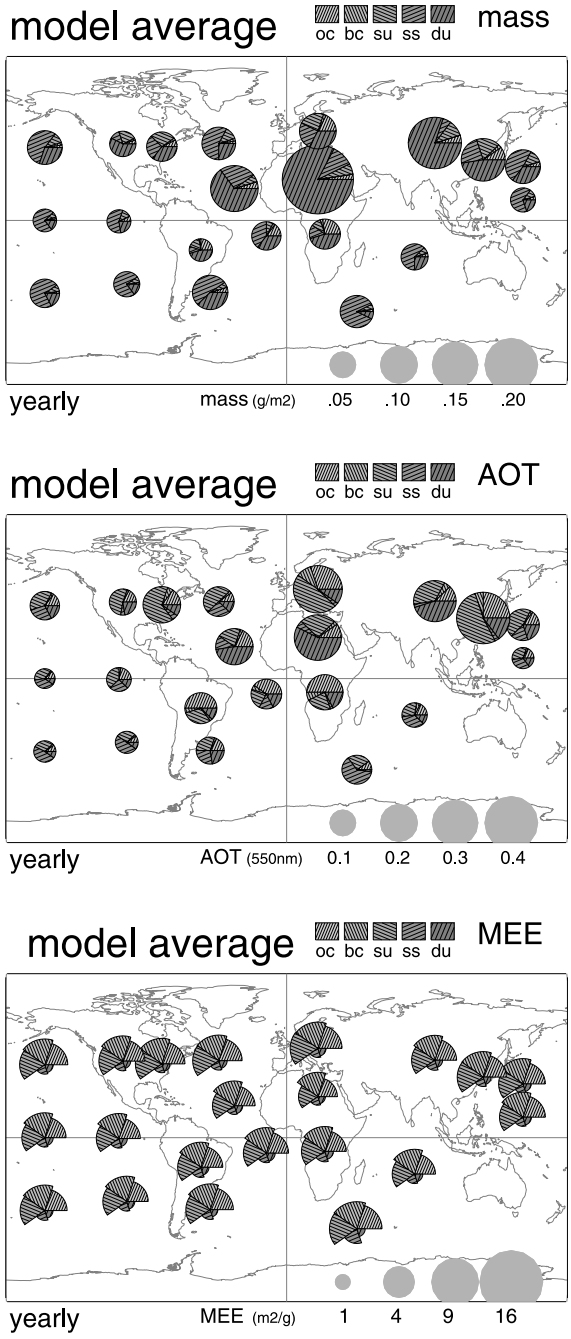

Figure 9. Aerosol mass, aerosol optical depth and mass extinction efficiency (the conversion factor that applied to mass yields optical depth) for the average model. The average model represents the mean among all seven models. Regional averages of the five aerosol types (organic carbon, black carbon, sea salt, sulfate and dust) are compared. See color version of this figure in the HTML.

distribution are provided. As the median (50% probability value) is usually smaller than the mean, the distribution has a long tail toward larger optical depths or in other words large optical depths or less common. On the basis of data from the three sample sites, this trend is more common for dust, early in the biomass burning season and during urban winters.

3.1.3. Sky and Sun Photometer Data

[80] The combined use of sky-radiance and direct attenuation data permits the derivations of aerosol size (-distribution) and aerosol absorption. Aerosol monthly averages for optical depth τ, single-scattering albedo ω_0 and size r_e (Σ volume/Σ surface area) are compared for the three sample sites in Figures 13 and 14.

[81] Monthly averages for the optical depth τ in Figure 13 resemble those of Figure 12, despite a much weaker statistics. Monthly averages for the mid-visible single-scattering albedo ω_0 demonstrate that lower values are linked to biomass burning (especially in the early season) and that values for urban and dust aerosol are closer to one. Size-distributions for urban and biomass-dominated aerosol resemble each other and the effective particle radii r_e are in the accumulation mode (ca. 0.2 μm). In contrast, for dust-dominated aerosol effective radii r_e are in the coarse mode (usually exceeding 1 μm). For dust, the size-distribution information of the accumulation mode is rejected, when nonsphericity is involved. (Nonsphericity is indicated when the inversions indicate a smaller real part of the refractive index in the visible than in the near-infrared. In case of nonsphericity, the enhanced side scattering in interpreted by the inversion as a large number of small spheres, thus concentrations of the accumulation mode are artificially raised.)

[82] The simultaneous retrieval of multiple aerosol properties from AERONET [*Dubovik et al.*, 2002] permitted an exploration of correlations between absorption potential ($1 - \omega_0$), optical depth τ and size r_e:

[83] 1. For biomass aerosol (e.g., Mongu) the absorption potential appears independent from optical depth and optical depth and aerosol size appears anti-correlated toward the end of the biomass season.

[84] 2. For dust aerosol (e.g., Cape Verde) there is no clear correlation between optical depth and absorption potential. However, early in the year low optical depths tend to be associated with stronger absorption potential. A likely explanation are contributions of biomass aerosol to background conditions during that time, which is in agreement with AERONET size-distribution shifts to smaller sizes. Correlations between optical depth and size vary for dust, with usually positive correlations (e.g., large sizes and large optical depth) away from sources and with anti-correlations more common near dust sources.

[85] 3. For urban aerosol (e.g., GSFC), absorption and optical depth are commonly anti-correlated especially during the summer season. A good correlation between atmospheric water vapor and optical depth signals the influence of water uptake on the aerosol composition. The correlation between optical depth and aerosol size is weak, although there is a good correlation to the smaller aerosol sizes ($r_e < 0.5$ μm).

[86] The AERONET (sun/sky) statistics suggests several important things: (1) Variations in aerosol concentrations are much stronger than variations for aerosol composition or size. (2) Large concentrations are usually less common than small concentrations. (3) And aerosol absorption can be significant, especially near sources of biomass burning and urban pollution.

[87] With a complete aerosol definition, the local aerosol influence on the energy balance can be determined. Calcu-

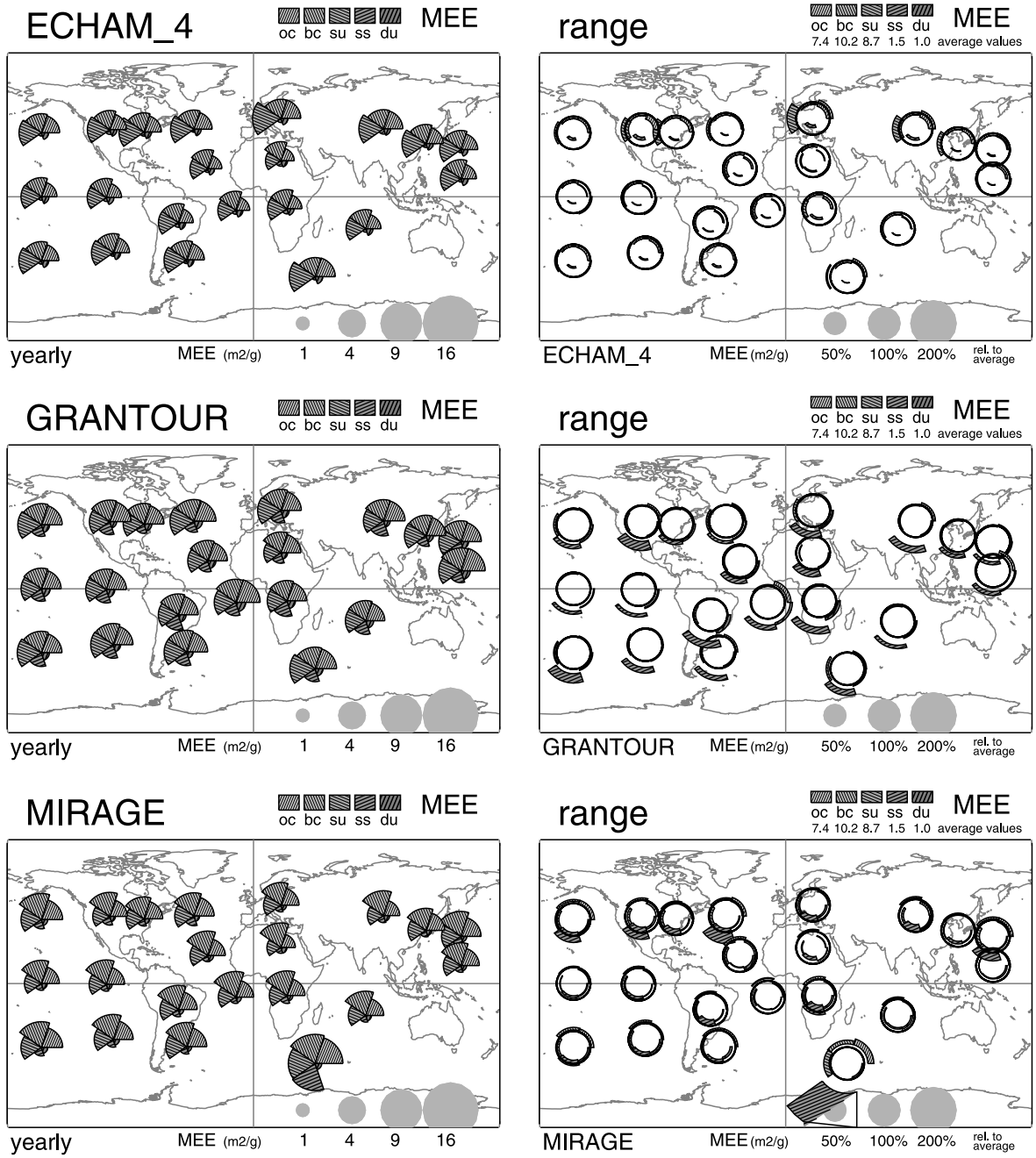

Figure 10. Mass extinction efficiencies (MEE) for the five aerosol types. Yearly averages for regions of Figure 2 are displayed in the left panels. The right panels display the range of three-month running means, where the range is plotted with respect to the average conversion factor, which is indicated by a circle. Values inside the circle indicate relative weak conversions, values outside the circle indicate relatively strong conversion. Circle values for (over all models and regions) averaged conversion factors of each aerosol type are listed in the captions of the right panel figures. See color version of this figure in the HTML.

lated (local) estimates of the seasonal direct aerosol forcing at the 20 AERONET sites of Table 13 are provided in Appendix A.

3.1.4. Comparison Issues

[88] AERONET statistics is based on local measurements samples. Their usefulness, when comparing to simulations of global models, depends largely on indifferences to (daytime and clear-sky) sampling and on the ability to represent on regional scales. Thus potential biases of monthly averages of AERONET data are explored next.

3.1.4.1. Temporal Representation

[89] Data sampling at particular daylight times or particular days can bias long-term averages. AERONET data are sampled only during daylight hours in the absence of clouds. The sampling is usually irregular because of the requirement of cloud-free conditions. An evaluation of

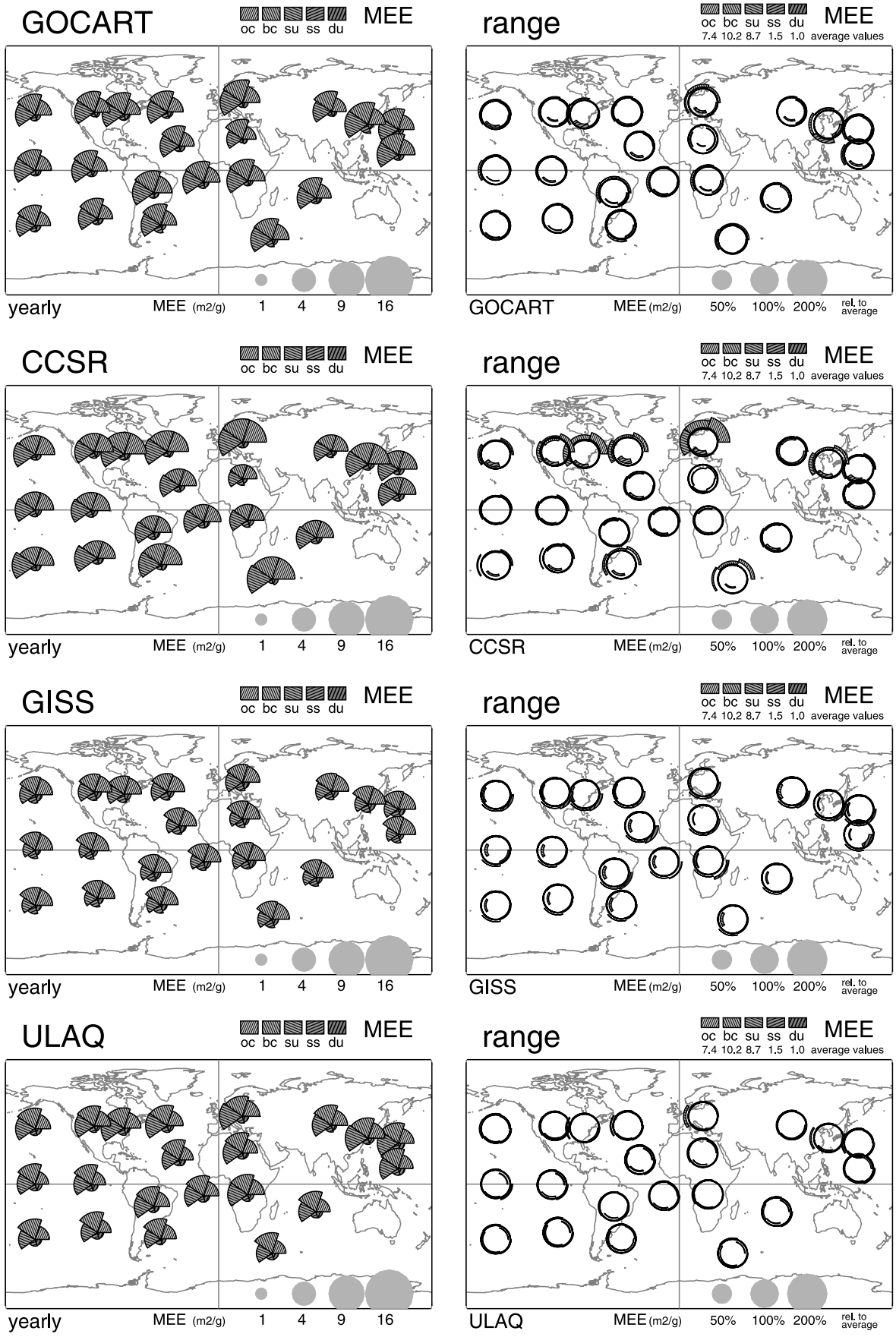

Figure 10. (continued)

Table 12. Simulated Mass Extinction Efficiency: Values of the Median Model and Models With Extreme Tendencies[a]

	Yearly Average Component Mass Extinction Efficiency, m^2/g									
	OC		BC		SU		SS		DU	
	Avg.	Max/Min	Avg.	Max/Min	Avg.	Max/Min	Avg.	Max/Min	Avg.	Max/Min
Urban sources	8	***CC***	10	***UL***	13	*GI, MI*	1.2	***Gr, GI****/EC*	1.0	***GI****/MI*
Urban outflow	8	***CC***	10		10	*GI*	1.3	***Gr, GI****/EC, CC*	1.0	*MI*
Dust sources	6		10		7	***UL****/MI*	1.1	***Gr, GI****/GO, EC*	.9	***GI***
Dust outflow	6	*EC*	10		7	***CC****/GI*	.9	***Gr, GI****/EC*	.9	***GI, Gr***
Biomass sources	7	*EC*	10		8	***GO****/GI*	1.2	***Gr****/EC, GO*	1.0	***GI****/MI, GO*
Biomass outflow	7	***Gr, CC****/EC*	11	*EC*	8	***CC****/GI*	1.1	***Gr, GI****/EC*	1.1	***Gr****/MI*
Remote, tropics	7	*EC, UL*	10	***MI***	8	*GI*	1.1	***Gr, GI****/EC*	1.1	*MI*
Remote, S. Hemis.	8	***MI, CC****/UL*	11		11	***CC****/GI, UL*	1.3	***Gr, GI****/EC*	1.0	
	Seasonality for Component Mass Extinction Efficiency									
	OC		BC		SU		SS		DU	
	Var	Max/Min	Var	Max/Min	Var	Max/Min	Var	Max/Min	Var	Max/Min
Urban sources	.23	***CC****/GI, UL*	.10	*GI, EC*	.26	***CC, EC****/GO, MI*	.38	*GI, UL*	.11	***GO***
Urban outflow	.23	***MI****/GI, UL*	.04	***MI****/GI, EC*	.17	***MI***	.23	***MI, CC****/GI, UL*	.11	***GI****/UL*
Dust sources	.12	***EC****/GI, UL*	.03	*GI, EC*	.19	***EC****/UL*	.24	***MI****/GI, UL*	.13	*UL*
Dust outflow	.11	***EC, MI****/GI*	.04	***MI****/GI, EC*	.17	***GI***	.30	*GI, MI*	.20	***MI****/EC*
Biomass sources	.12	***EC****/GI,UL*	.04	***MI****/GI, EC*	.23	*UL*	.22	***MI****/GI*	.13	
Biomass outflow	.13	*GI, Gr*	.04	*GI, EC*	.11	***GI***	.20	*GI, CC*	.09	
Remote, tropics	.08	***GO****/GI*	.06	*GI, EC*	.14	***GI***	.11	***MI****/GI, UL*	.12	*Gr*
Remote, S. Hemis.	.24	*GI, UL*	.05	***MI****/GI, EC*	.14	***MI, GI***	.30	***MI****/GI, UL*	.11	***MI****/UL*

[a]For class-combined regions (see Table 7), yearly averages (Avg) and seasonality (Var) of the median model (4th-ranked among all models) are presented. Seasonality is the ratio of the 3-month running mean range during a year and the yearly average. In addition, models are displayed whose values for Avg or Var exceed (italic-bold) or fail (italic) that of the median model by more than 30% (for Avg) and 50% (for Var).

AERONET, by binning data according to the time of measurement shows, that daily trends are quite common. However, in terms of monthly averages large differences are rare (usually less than 5% and in extreme cases still less than 20% of the daily average). A summary of trends between morning (am) and afternoon (pm) measurements for the 20 AERONET sites is given in Figure 15.

[90] To avoid temporal sampling issue in the future, comparisons could apply subsampling techniques to accommodate the least frequent measurement. For model comparisons to data from AERONET or satellites, this means a restriction of model output to daytime or overpass times and cloud-free situations. However, there are scale complications. For instance, what corresponds to 'locally cloud-free' on a 300 × 300 km scale? It also does not help that 'cloud-free subsets' of models often display opposing trends: Smaller optical depths are explained by aerosol removal within clouds, while larger optical depths are attributed to swelling in the vicinity of clouds. Also considering the fewer events from subsampling, it remains unclear whether the benefit of more direct comparisons outweighs the loss in statistical significance.

[91] For comparisons between AERONET and satellite retrievals, subsampling to the tune of daytime overpasses by polar-orbiting satellite is desirable (if satellite pixels are small enough to retrieve local aerosol properties). With aerosol detecting geo-stationary satellites and (proposed) aerosol detecting satellites that move with the sun, however, AERONET subsampling may not be necessary.

3.1.4.2. Regional Representation

[92] Local AERONET data may not apply to regions, representing a GCM model grid point, even if averaged over time. To illustrate this point, an example is given in Figure 16. Yearly averages and their monthly variability during a year are presented for four European AERONET sites in northern Italy and France (Ispra, Lille, Toulouse and Aire Adour). All four sites display quite different properties, although they are close enough to fall into a region represented by a single grid point in models. For comparison, simulations of models are displayed. Here for each model differences in site-properties are the result of spatial interpolation. Despite the significant spread among model predictions for the European region, each model can claim good agreement to measurements depending on its site choice.

[93] Models, however, cannot be given the freedom to pick sites statistics that fits best. Rather it needs to be determined, what site, if any, can represent on regional scales. To find answers to the regional representation of local data, satellite data are applied. Although satellite retrievals may lack accuracy, the spatial coverage of retrievals can identify those AERONET sites, which qualify for comparisons on regional scales and which do not. For this purpose values at the smallest retrieval resolution over each site were compared to simultaneous regional (300 × 300 km) averages. Based on aerosol optical depth monthly averages of retrievals by MODIS and TOMS, a summary of regional biases is given in Figure 17. MODIS data were preferred over TOMS data, because MODIS aerosol products are available at smaller subscales.

[94] The identification of sites, solely based on satellite average at different spatial scales, is less successful than hoped for. Only sites with strong local pollution are easily identified (e.g., Mexico City). Otherwise trends on local biases remain unclear. Even on the basis of only 10 × 10 km averages (of the MODIS aerosol optical depth product), trends of a site's regional representation within a month can vary wildly in strength and even in sign. Apparently, local issues (e.g., orography) and transport (e.g., advection of different air masses) cannot be overlooked. In light of the

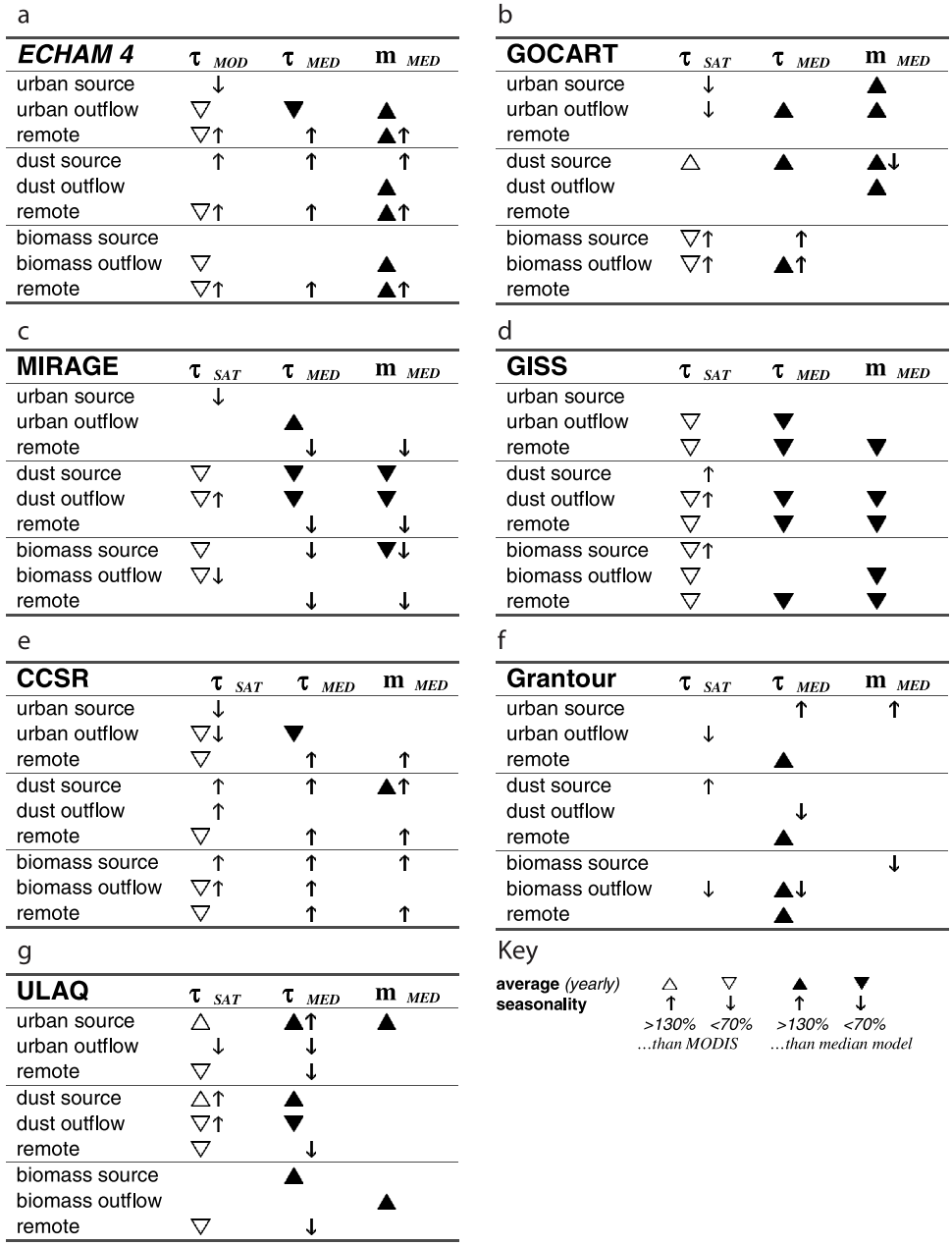

Figure 11. Model tendencies for yearly average and seasonality for component combined optical depth τ and mass **m** with respect to the median model and with respect to satellite data.

variability, much stronger statistical samples are needed than those provided by the limited number of successful local MODIS aerosol retrievals during one month over land. In summary, a much more detailed analysis and a better statistical sample are necessary to identify regional trends for many sites.

[95] Thus, for the model evaluation with AERONET data, only three sites with known local pollution were removed: Mexico City, Arica and Goddard. In addition three other sites were removed because of a relative close geographical proximity to other AERONET sites: Banizoumbou, Cuiaba and Conception. To maintain the number of AERONET sites at 20 for the model evaluations, six additional sites were added and are introduced in Table 14.

3.1.5. Comparison of Aerosol Optical Depths

[96] Model simulated aerosol optical depths τ are evaluated by comparing yearly mean, seasonality strength and seasonality phase. Comparisons at 20 AERONET sites are illustrated in Figure 18, quantified in more detail in Appendix C and summarized in Table 15.

[97] The combined average of all models (see 'model average' in Figure 18) illustrates in general terms differences between simulated aerosol optical depths and AERONET data. There is a tendency by models to underestimate in the tropics, especially in regions of biomass burning, and there is a tendency by models to overestimate from the Mideast or Asia, in regions with significant dust contributions. Agreement seems best near and off urban industrial regions of the Northern Hemisphere. This could suggest that

Table 13. Twenty AERONET Sites: Location, Altitude, Dominant Aerosol Type, Number of Measurements Prior to the Year 2000[a]

Location	Latitude, °N	Longitude, °E	*z*, m	Site Type	Aerosol	SUN	SKY-a	SKY-g
Mongu	−15.3	23.2	1100	continental	biomass	10169	1297	423
Sevilleta	34.4	253.1	1480	continental	rural	34611	3280	1459
Cuiaba	−15.5	304.0	250	continental	biomass	6162	464	325
Banizoumbou	13.5	2.7	0	continental	dust	8622	1550	608
Cape Verde	16.7	337.1	60	near-ocean	dust	11455	956	444
Waskesiu	53.9	253.9	550	continental	biomass	12601	457	204
Goddard (GSFC)	39.0	283.1	50	continental	urban	29260	4168	2291
HJ-Andrews	44.2	237.8	830	continental	rural	10569	1198	374
Ispra	45.8	8.6	240	continental	urban	6309	417	99
Dry Tortugas	26.4	277.2	0	near-ocean	mixed	12732	958	294
Lanai	21.8	203.0	80	near-ocean	maritime	10532	1171	290
Alta Floresta	−9.9	302.7	180	continental	biomass	5800	366	116
Bahrain	26.2	50.5	0	near-ocean	dust (+urban)	9634	1186	947
Mexico City	19.3	260.8	2270	continental	urban	1966	628	198
Bondville	40.1	271.7	210	continental	rural	8462	440	221
Ilorin	8.3	4.3	350	continental	dust (+bio)	4848	726	291
Dalanzadgad	43.6	104.4	1470	continental	dust	9371	940	256
Conception	−16.1	298.0	500	continental	biomass	2416	283	212
Sede Boker	30.5	34.5	400	continental	dust	15391	1950	1131
Arica	−18.5	289.7	30	near-ocean	urban (+dust)	10142	1281	831

[a]Listed are the number of quality-controlled attenuation measurements (SUN), the number of all sky-scanning measurements (SKY-a) and, as the "quality-assured" subset, the number of sky-data (SKY-g), whose measurements coincide with SUN quality measurements.

models underestimate contribution from biomass burning, overestimate contributions of dust and do well for contributions from urban pollution. Unfortunately, it is not quite so simple, because there are large differences among models, as illustrated for the aerosol optical depth yearly averages in Figure 18.

[98] Based on comparisons for yearly averages, seasonality strength and seasonality phase (detailed comparison are provided in Appendix C) the numbers of matches or mismatches with respect to AERONET at all 20 sites of Figure 18 are summarized individually for each model in Table 15.

[99] Simulated yearly averages of aerosol optical depth agree at best at about half of the AERONET sites. For most models underestimates are more common than overestimates. Exceptions are GOCART with its very efficient dust transport and ULAQ with its unusual strong urban sources.

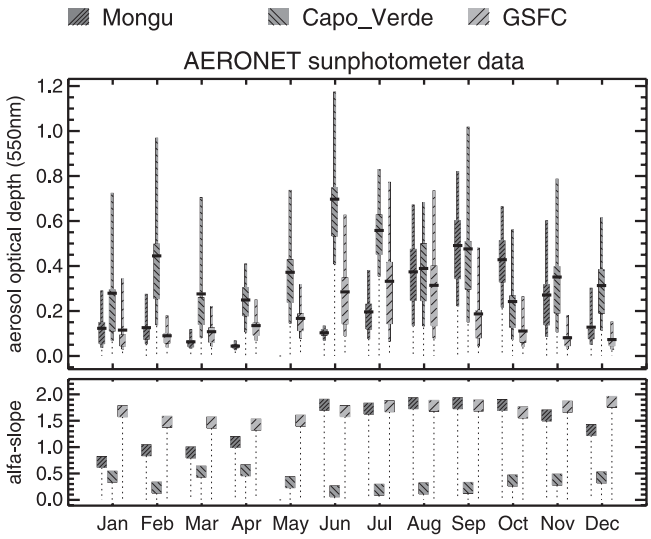

Figure 12. Sun-photometer data samples at sites representing biomass burning (Mongu, Jul-Nov), dust (Capo_Verde) and urban aerosol (GSFC). Monthly data for visible optical depth τ (upper panel) and Angstrom parameter (lower panel) are presented. For optical depth, aside from the average (horizontal bar), variability is also indicated via the 30 to 70% PDF range (thick column) and the 10 to 90% PDF range (thin column). See color version of this figure in the HTML.

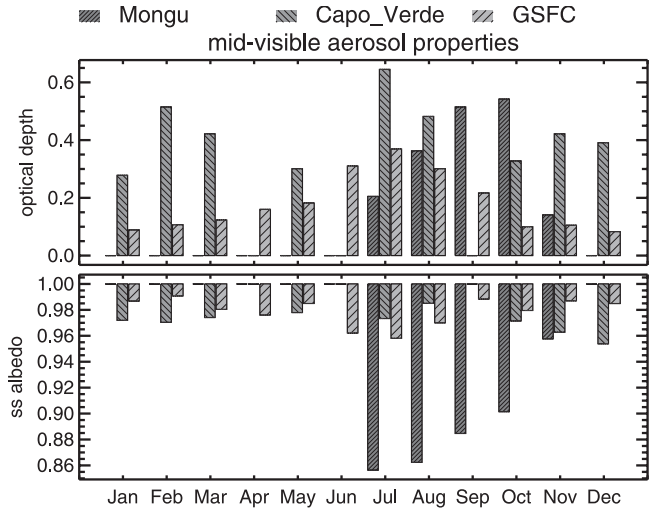

Figure 13. Sun/sky-photometer data samples at sites representing biomass burning (Mongu, Jul-Nov), dust (Capo_Verde) and urban aerosol (GSFC). Monthly averages for visible optical depth τ (upper panel) and single-scattering albedo (lower panel) are presented. Note that reliable values for single-scattering albedos from sky-radiances require optical depths in excess of 0.3. See color version of this figure in the HTML.

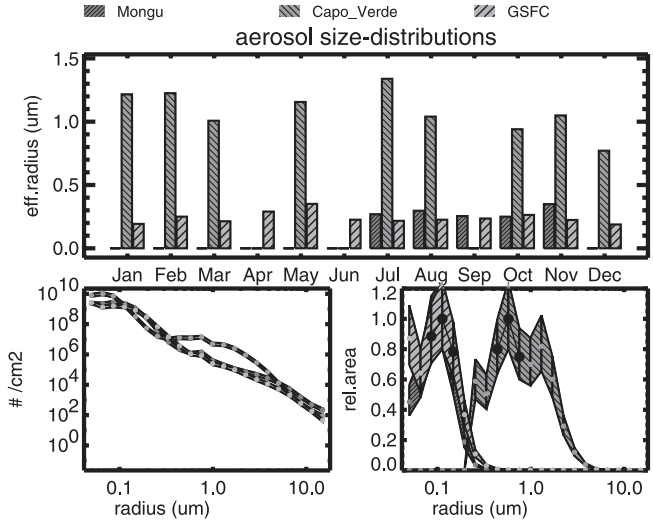

Figure 14. Aerosol size data from Sun/sky-photometer measurements at sites representing biomass burning (Mongu, Jul-Nov), dust (Capo_Verde) and urban aerosol (GSFC). Monthly averages for effective radius (upper panel) and yearly averages for size-distribution (lower left) and for sizes with maxima in surface area contribution (lower right) are given. The amplified concentration for dust at radii below 0.1 μm due to nonsphericity has been removed for the determination of the effective radius. See color version of this figure in the HTML.

Simulated seasonality strength for aerosol optical depth is usually stronger near dust sources, but weaker at midlatitude sites of the Northern Hemisphere (AERONET minima are lower) and also weaker at biomass burning sites in the tropics (AERONET maxima are higher). Simulated seasonality maxima (phase) are correct at about half of the AERONET sites. Matches of all three aerosol properties (yearly average, seasonality strength and seasonality phase) occur only at a rate of about 1 in 4 (AERONET sites). Although this disappoints, complete matches between AERONET and MODIS satellite data are also only of the same order.

[100] The location of the matches is also indicative of the strength of particular models: Grantour does usually well in all outflow regions, ECHAM4 does best in the N. Pacific, CCSR does best over Europe, GISS does best over the continental United States and GOCART is best near dust and biomass sources.

[101] Another approach to evaluate models with AERONET data is the comparison of seasonal averages. For the central month of each season (January, April, July and October) comparisons are presented in Figure 19 and a statistical summary from seasonal comparisons (which are provided in Appendix C) for the 20 sites of Figures 18 or 19 are given in Table 16.

[102] On the basis of larger deviations to AERONET data, overall seasonal trends were derived. These trends are consistent with earlier results that only GOCART and ULAQ have usually larger optical depths than AERONET. However, there are now two models that display overestimates as well, although only for one or two seasons: In ECHAM4 the overestimates relate in to a very strong dust component off Africa around April (in conjunction with the 'Azores HIGH') and in CCSR the overestimates relate to an unusual early (June rather than August) onset of the tropical biomass season.

[103] The comparisons for particular months indicate that differences with AERONET and among models are more

LOCATION	J	F	M	A	M	J	J	A	S	O	N	D	comments
Mongu	/	/	/	=	/	=	=	=	▲	▲	=	▽	
Seviletta	▲	▲	▲	▲	▲	▽	▽	▽	▽	=	=	=	
Cuiaba	/	/	/	/	/	=	=	▲	▲	▽	/	/	noon maxima …in fall
Banizoumbou	▲	▲	=	/	/	/	=	/	=	=	=	=	noon minima …in fall
Cape Verde	▲	=	▽	=	▽	▽	▽	=	=	=	=	=	
Waskesiu	/	/	/	/	=	=	=	=	=	=	/	/	
Goddard (GSFC)	▽	=	=	=	=	=	=	=	▽	=	=	=	noon minima …spring to fall
HJ-Andrews	/	/	/	/	=	=	=	▲	▲	▲	/	/	
Ispra	▲	▲	=	=	=	▲	=	=	▲	=	=	=	
Dry Tortugas	=	=	=	=	=	=	=	=	=	=	=	=	
Lanai	▲	=	=	=	=	=	=	=	▲	▲	▲	▲	
Alta Floresta	/	/	/	/	=	=	=	▲	▽	▽	/	/	noon maxima …in fall
Bahrain	=	=	=	=	=	=	▽	▲	=	=	=	=	noon maxima …in fall
Mexico City	/	/	/	▲	▲	▽	/	/	/	/	/	/	
Bondville	/	=	=	▽	=	▽	=	=	▽	=	=	=	noon minima …spring to fall
Ilorin	=	=	/	▽	=	=	/	/	/	=	=	▲	
Dalanzadgad	=	=	=	=	▲	▲	=	▲	=	=	=	=	
Conception	/	/	/	/	/	/	=	=	=	=	/	/	noon maxima …in fall
Sede Boker	=	=	=	=	▲	▲	=	=	=	▲	▲	▲	noon minima …in spring
Arica	▽	▽	▽	▽	▽	▽	=	▽	▲	=	▽	▽	

daytime variations: ▽ *am AOT > pm AOT* ▲ *am AOT < pm AOT* = *no trend* / *insufficient data*

Figure 15. Daytime trends for aerosol optical depths between morning and evening at 20 AERONET sites.

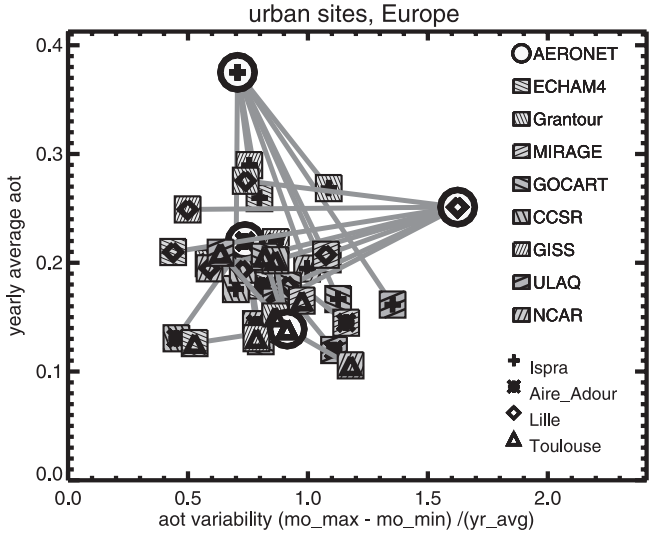

Figure 16. Comparisons of aerosol optical depth yearly average (y-axis) and variability (x-axis) at four European sites between AERONET statistics and model simulations. All four sites (Ispra, Aire Adour, Lille and Toulouse) are located within the area represented by a grid-point in most models. Despite large model differences, each model can claim "good agreement to AERONET" by picking an appropriate site. See color version of this figure in the HTML.

diverse than the comparison of the yearly average (also in Figure 19) indicates. This is best illustrated for the site in South America, where the strong seasonal cycle due to biomass burning (maximum from August to October) is poorly simulated. Even worse aerosol overestimates for the wet season suggest a less severe mismatch, when comparing yearly averages.

[104] In summary, matches between simulated aerosol optical depths and AERONET statistics over an entire year are the exception. However, no model (unlike satellite retrievals) displays a unanimous bias toward AERONET statistics, despite general trends of individual models to larger or smaller aerosol optical depths. Based on comparisons to AERONET, the identification of model deficiencies is difficult and limited to large deviations. This usually requires sites and seasons with large aerosol optical depths and is most useful at sites and times, when a particular aerosol type dominates (e.g., carbon during the biomass burning season). A detection of model deficiencies involving smaller differences with AERONET data will have to wait until model and AERONET data are matched in time and until there is a better understanding about the regional representation (and its seasonal dependence) for each AERONET site.

3.1.6. Comparison of Other Aerosol Properties

[105] With sky-radiance measurements of AERONET local statistics can be determined not only for aerosol optical depth but also aerosol size(-distribution) and aerosol absorption (see Figures 13 and 14). These data provide added tools to evaluate aerosol modules in global models, especially since these properties are less variable than optical depth, thus regional representation will be less of an issue.

[106] A brief sample for the representation of aerosol absorption is provided with comparisons for the mid-visible aerosol single-scattering albedo. (In that context it should be repeated that a good AERONET estimate requires sufficient aerosol optical depth: $\tau > 0.3$.) Comparisons between single-scattering albedos for the three major AERONET sample sites of Figures 2, 13, and 14 (Mongu, Cape Verde and Goddard) are presented in Figure 20.

[107] Satellite estimates from TOMS retrievals are in good agreement with AERONET data. Also in accordance to AERONET, the smallest single-scattering albedos are associated with biomass burning. This expected trend is also reproduced by those models that supplied data for this comparison, with one exception: CCSR displays a strong absorption for dust, which at least in part reflects its choice for a rather large mid-visible refractive index imaginary part (0.08). There are also absolute differences among models. ULAQ has a weaker absorption potential, whereas GOCART and especially ECHAM4 have a stronger absorption potential than AERONET. The reasons for these differences are not completely understood.

[108] Comparisons of size-distributions (or at least effective radii) were not possible, as for the initial comparison no request for 3-dimensional fields of simulated aerosol size-distributions was made. Now, with a growing AERONET database on aerosol size-distributions, comparisons of aerosol size (and size-distributions) should become a requirement in future model evaluations. The aspect of good (local) statistics on aerosol size-distributions may also lead to reasonable estimates for (wet) aerosol mass. Provided sufficient knowledge exists on permitted water uptake in simulations (to convert from dry to wet mass), comparisons of mass between AERONET and models may be possible. Comparisons at the mass level (Step 2 in Figure 1) rather than the optical depth level (Step 3 in Figure 1) seem desirable, as it will not allow model uncertainties in mass extinction efficiencies to impact evaluations of aerosol processing. Mass comparisons will be particularly valuable to model evaluations for the aerosol components of dust and sea salt.

3.2. Satellite Data

[109] Aerosol properties can be retrieved from satellites data. The most common retrieved aerosol property is the aerosol optical depth. For comparisons to models (and AERONET) the retrieved optical depths were spectrally adjusted to the mid-visible wavelength of 0.55μm. From polar-orbiting satellites (with at best one aerosol retrieval per day) three data sets are considered: MODIS, TOMS and AVHRR. All data sets cover at least an entire year. MODIS data [*Kaufman et al.*, 1997a] cover the year of 2001. TOMS data [*Torres et al.*, 2002] are based on measurements over two decades, from 1979 and 2000. Not considered in the TOMS record are (1) times of major contamination by volcanic aerosol (the 2 years following the eruptions of El Chichon in April 1982 and Mt. Pinatubo in June 1991), (2) the time of the Kuwait oil fire in spring of 1991 and (3) periods of no operations from March 1994 until July 1996. AVHRR data [*Geogdzhayev et al.*, 2002] are only based on NOAA-9 data, covering the time period from February 1985 to October 1988. For comparisons to models (and AERONET) all satellite retrievals were temporally and

LOCATION		J	F	M	A	M	J	J	A	S	O	N	D		comments
Mongu	M	▽	/	▽	▽	▽	▽	=	=	=	=	/	▽	X	**good** *biomass site* (Jul-Nov)
Seviletta	T	=	=	=	=	=	=	=	=	=	▽	=	=	X	*rural*
Cuiaba	M	/	/	=	=	=	△	△	=	=	/	/	/		(near Alta Floresta) ***removed***
Banizoumbou	T	=	=	=	=	=	=	=	=	=	=	=	=		(near Ilorin) ***removed***
Cape Verde	T	=	=	=	=	=	=	=	=	=	=	=	=	X	**good** *dust dominated*
Waskesiu	M	/	/	/	=	=	=	△	△	△	=	/	/	X	-15% in summer (boreal fires)
Goddard*GSFC*	M	▽	▽	▽	▽	▽	▽	▽	▽	▽	▽	▽	▽		+20%: local poll. ***removed***
HJ-Andrews	M	/	△	△	△	=	△	=	=	△	△	△	/	X	-15% (locally cleaner)
Ispra	M	△	△	▲	▲	△	△	△	=	=	=	=	△	X	-50% in spring (useful site?)
Dry Tortugas	M	=	=	=	=	/	/	/	/	=	=	=	=	X	**good** *maritime* (esp.in winter)
Lanai	M	=	▽	=	/	/	/	/	/	/	/	△	=	X	**good** *maritime*
Alta Floresta	M	/	/	/	▽	▽	△	△	=	=	=	=	/	X	**good** *biomass site* (Jul-Nov)
Bahrain	M	=	=	/	=	/	/	/	=	=	=	=	=	X	**good** *dust dominated*
Mexico City	M	▼	▼	▼	▼	▼	▽	▼	▼	▼	▼	/	/		+50%: local poll. ***removed***
Bondville	M	/	/	/	/	/	/	=	=	▽	=	/	/	X	**good** *urban-rural*
Ilorin	M	△	/	/	/	/	/	/	/	/	/	△	△	X	-25% (as biomass in late fall)
Dalanzadgad	T	▽	=	=	=	△	△	=	=	=	▽	=	▽	X	*dust-rural*
Conception	M	/	=	=	=	=	=	△	△	=	=	=	/		(near Alta Floresta) ***removed***
Sede Boker	T	=	=	=	=	▽	=	=	=	=	=	=	=	X	*dust-rural*
Arica	T	=	=	=	△	=	=	△	△	△	△	=	=		(in polluted region) ***removed***
Kaashidhoo	M	=	=	=	=	=	/	/	=	=	▽	▽	=	X	*urban outflow*
San Nicolas	M	△	△	=	=	/	/	/	=	=	=	=	=	X	*maritime mixed*
Aire Adour	T	△	△	=	=	=	=	=	▽	=	=	/	△	X	*urban*
Bonanza Cr.	M	/	/	/	=	=	=	=	=	△	/	/	/	X	*high latitude*
Nauru	T	=	=	=	=	=	=	=	=	=	=	=	=	X	*remote*
Kejimkujik	M	/	/	/	▽	▽	=	=	=	=	=	▽	▽	X	**good** urb.outflow (in summer)

▲: reg **>1.5***local, △: reg **>1.1***local, =: reg ~ local, ▽: reg **<.9***local, ▼: reg **<.66***local /: no data

Figure 17. Regional representation of local AERONET statistics based of monthly aerosol optical depth retrievals by MODIS (M) and TOMS (T). Ratios between regional (300 × 300 km) and local (10 × 10 km, MODIS) or subregional (80 × 80 km, TOMS) averages around selected AERONET sites are investigated. Ratios close to 1 (marked by an equals sign) suggest a good regional representation by local data. Data from sites with an ***X*** are used in the model evaluations.

spatially combined to global fields of monthly averages at a 1° latitude × 1° longitude horizontal resolution.

3.2.1. MODIS

[110] The Moderate-Resolution Imaging Spectroradiometer (MODIS) onboard EOS-Terra satellite was launched in December 1999 into a sun-synchronous polar orbit. Since February 2000, MODIS has continuously acquired measurements at thirty-six spectral channels (0.41–14 μm) at three different spatial resolutions (250 m, 500 m and 1 km). The MODIS aerosol algorithm derives aerosol optical depths at 0.47 and 0.66 μm over land [*Kaufman et al.*, 1997a] and aerosol properties (optical depth, effective radius, and fine-mode fraction) at 0.55, 0.67, 0.87, 1.24, 1.64, 2.1 μm over ocean [*Tanre et al.*, 1997]. Cloud screening is at 1 km resolution and thus far superior to that of the other two satellite data sets. MODIS measurements with a field-of-view of 110° or a swath width of 2,330 km provide near global coverage every day. Because of differences in surface characteristics, aerosol retrievals algorithms over land and ocean are different.

[111] 1. Over land, MODIS employs primarily three spectral channels centered at 0.47, 0.66, and 2.1 μm at

Table 14. Six AERONET Replacement Sites for the Model Evaluation: Location, Altitude, Dominant Aerosol Type, and Number of Quality-Controlled Attenuation Measurements Prior to the Year 2000 Are Listed, As Well As Replaced AERONET Sites of Table 13 and Reasons for Their Replacement

Location	Latitude, °N	Longitude, °E	*z*, m	Site Type	Aerosol	SUN[a]	Replacing	Reason
Kaashidhoo	5.0	73.5	0	near-ocean	biomass	4724	Cuiaba	overlap
San Nicolas	33.3	240.5	133	near-ocean	maritime	10437	Banizoumbou	overlap
Nauru	−.5	337.1	0	near-ocean	maritime	4119	Conception	overlap
Aire Adour	43.7	359.8	80	continental	off-urban	4343	Goddard	polluted
Bonanza Creek	64.8	211.7	150	continental	rural	5169	Mexico City	polluted
Kejimkujik	44.4	294.7	154	continental	rural	738	Arica	polluted

[a]SUN, number of quality-controlled attenuation measurements.

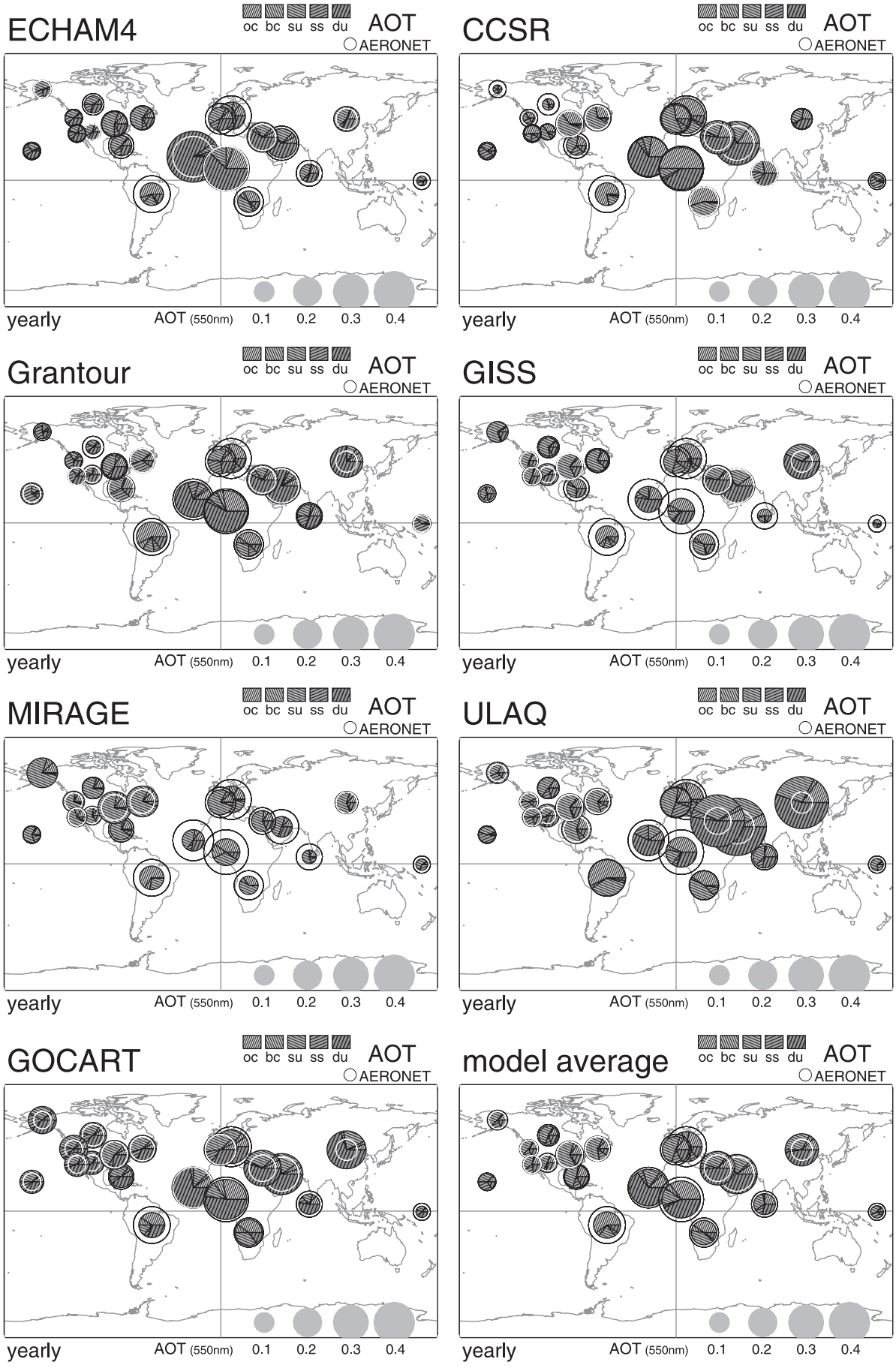
ECHAM4
CCSR
Grantour
GISS
MIRAGE
ULAQ
GOCART
model average
oc bc su ss du
AOT
AERONET
yearly
AOT (550nm) 0.1 0.2 0.3 0.4

Table 15. Local Agreement at 20 AERONET Sites: Matches in Terms of Yearly Average and Seasonality for Aerosol Optical Depth[a]

	AOT Versus AERONET								
	EC (>, ∼, <)	GO (>, ∼, <)	MI (>, ∼, <)	GI (>, ∼, <)	CC (>, ∼, <)	Gr (>, ∼, <)	UL (>, ∼, <)	MO (>, ∼, <)	TO (>, ∼, <)
Yearly average	*2*, ***10***, *8*	*7*, ***9***, *4*	*3*, *7*, *10*	*3*, *7*, *10*	*3*, ***11***, *6*	*3*, ***12***, *5*	*5*, ***12***, *3*	*9*, ***9***, *1*	*14*, ***6***, -
Season strength	*4*, ***12***, *4*	*1*, ***14***, *5*	*3*, ***9***, *8*	*4*, ***15***, *1*	*3*, ***13***, *4*	*1*, ***14***, *5*	*2*, ***12***, *6*	*2*, ***15***, *2*	*2*, *7*, *14*
Season phase	***13***	***13***	***8***	***14***	***11***	***10***	***10***	***11***	***7***
Avg +s-str. +s-ph	4	3	1	3	4	6	2	5	1

[a]When possible, a distinction was made between clearly larger values (>), clearly smaller values (<), and close agreement (∼). Yearly averages were considered agreeable when the simulated optical depth remained within 30% of the AERONET value. Seasonality strength was considered agreeable for variations within 50% of the AERONET value. Seasonality phase was considered agreeable when the month with the maximum of the three-month running average for optical depths had not shifted by more than one month from the month of the AERONET maximum. The last line indicates at how many sites (out of 20) all three aerosol properties matched the AERONET statistics.

500 m resolution. The dark target approach developed over vegetated surfaces (e.g., forest, grassland) is used to estimate the surface reflectances (ρ_s) at 0.47 μm and at 0.66 μm from the measurements at 2.1 μm assuming ${\rho_s}^{0.47\ \mu m}/{\rho_s}^{2.1\ \mu m} = 0.25$ and ${\rho_s}^{0.66\ \mu m}/{\rho_s}^{2.1\ \mu m} = 0.5$ [*Kaufman et al.*, 1997b]. Snow/ice and water covered surfaces are excluded, because there this empirical relationship becomes invalid. Aerosol optical depths are derived from averaged reflectance of an ensemble of cloud-free pixels on a 10 km × 10 km grid.

[112] 2. Over oceans, the algorithm inverts the spectral measurements (0.55–2.1 μm) to derive the spectral aerosol properties from cloud-free and glint-free measurements in on a 10 km × 10 km grid.

[113] MODIS-derived aerosol properties were validated against AERONET Sun photometer measurements with the errors of $\Delta\tau_a = \pm 0.05 \pm 0.20\tau_a$ over land [*Chu et al.*, 2002], and with the errors of $\Delta\tau_a = \pm 0.03 \pm 0.05\tau_a$ over ocean [*Remer et al.*, 2002]. In addition to the mid-visible aerosol optical depth, MODIS also provides information on particles size, deriving ratios of prescribed size modes from variations in spectral extinction. This size information is not used in this study but will certainly be of value in future model evaluations.

3.2.2. TOMS

[114] The Total Ozone Mapping Spectrometer (TOMS) is a 6-band (UV: 6) cross track scanning radiometer flown on many different polar-orbiting satellites (NIMBUS-7, Meteor-3, Earth Probe, ADEOS) since 1979. Swath width and spatial resolution are about 3000 km and 50 km. Although primarily designed to monitor ozone, measurements in channels with weak (0.34 μm) or no ozone absorption (0.38 μm) permit the retrieval of aerosol properties [*Torres et al.*, 1998]. The optical depth of scattering aerosol is derived from enhancements in molecular backscatter at 0.38 μm. Optical depth of absorbing aerosol and aerosol single-scattering albedo are derived from changes to the background spectral dependence of molecular scattering between 0.34 μm and 0.38 μm. These changes are a function of aerosol altitude. Thus not only appropriate assumptions of aerosol size (and shape) but also appropriate assumptions of aerosol elevations are essential. Altitude underestimates lead to aerosol optical depth overestimates and vice versa. For absorbing aerosol the current retrieval assumes an average altitude of 3 km. Also without sufficient background signal below the aerosol layer the detection of absorbing aerosol near the surface is difficult. The retrieval assumes surfaces at sea level, which causes overestimates for absorbing aerosol optical depths at high-altitude regions. The large 50 km × 50 km pixel size of a TOMS image makes it difficult to avoid contamination by clouds, which can have a strong impact on the retrieval of absorbing aerosol. A reflection threshold technique is assumed to remove clouds. Surface reflections, although small both over water and land in the ultraviolet, are based on minimum reflections for cases, where the spectral dependency of molecular scattering did not change.

3.2.3. AVHRR

[115] The Advanced Very High Resolution Radiometer AVHRR is a 5 band (vis: 1, near-IR: 2, IR: 2) cross track scanning radiometer flown on many NOAA polar-orbiting satellites since 1978. Swath width and spatial resolution are about 2800 km and 1 km. Aerosol optical depths are derived from visible (0.63 μm, as the nominal value for the 0.58–0.68 μm band) and near-infrared (0.83 μm, as the nominal value for the 0.72–1.1 μm band) reflection anomalies for cloud-free 1 × 4 km GAC (global area coverage) pixels over sun-glint free ocean scenes. For accuracy concerns, here AVHRR monthly averages are only based on NOAA-9 data (for the period from February 1985 to October 1988). These data had fewer calibration drifts than AVHRR sensors on other NOAA satellites. In addition, no major contamination by stratospheric aerosol from volcanic eruptions occurred during that time. Monthly averages include data from all four years. Retrieved optical depths of the visible band (0.63 μm) were extrapolated to values at 0.55 μm wavelength with the Angstrom parameter. The Angstrom statistics is based on a power law size-distribution, whose power exponent is inferred from the optical depth ratios of the visible and the near-infrared band. Other retrieval assumptions are moderate absorption ($0.97 < \omega_0 < 0.99$) and a spherical aerosol shape [*Mishchenko et al.*, 1999]. Cloud screening is based on the ISCCP data set [*Rossow et al.*, 1993], with the additional constraints, as to include only the warmest pixels (only retaining pixels with IR temperatures warmer than the composite value).

Figure 18. (opposite) Local comparisons of yearly average aerosol optical depth. Interpolated model simulations (disks) are compared to AERONET data (circles). Dark circles indicate model underestimates, and white circles indicate model overestimates. See color version of this figure in the HTML.

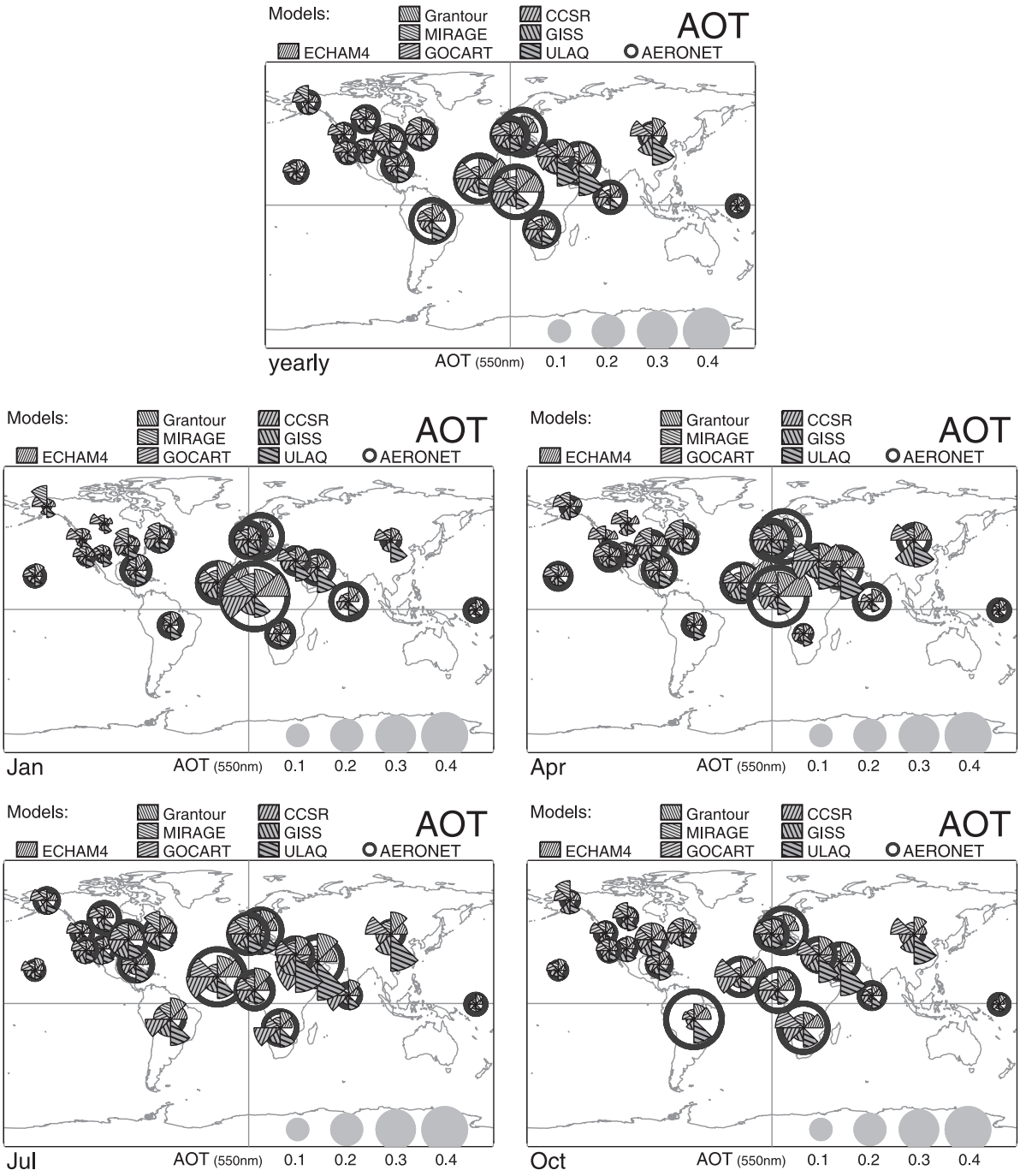

Figure 19. Local comparisons of simulated (outer pie-section border) and measured (circle) aerosol optical depths at 20 AERONET sites. Aside from yearly averages in the top panel, averages for the months of January, April, July and October are presented, to illustrate seasonal differences. See color version of this figure in the HTML.

3.2.4. Comparisons

[116] Evaluations of models with satellite data are conducted by comparing averages of regions. These regions, which were already introduced in Figure 2, are much larger than regions associated with a particular model grid point. In Figure 21, yearly and regionally averaged aerosol optical depths of satellite retrievals and models are compared. Separate comparisons are given with respect to individual models and to the 'average' model. The initial focus, however, will be on a comparison of satellite retrievals by aerosol class (see Table 7) to determine which satellite data should best be used in model evaluations.

[117] 1. In urban source regions, MODIS averages are larger than TOMS for East Asia, but smaller than TOMS for Europe and North America. In comparisons to AERONET (see Appendix C) TOMS more than MODIS, lacks on seasonality (in particular seasonal minima) and tends to overestimate. Choice is MODIS.

Table 16. Local Agreement at 20 AERONET Sites: Significant Mismatches in Seasonal Averages for Aerosol Optical Depth[a]

	AOT Versus AERONET																											
	EC				MI				GO				GI				CC				Gr				UL			
	1	2	3	4	1	2	3	4	1	2	3	4	1	2	3	4	1	2	3	4	1	2	3	4	1	2	3	4
Overest. > 0.2	1	2	–	–	–	–	–	–	–	–	1	1	–	1	1	–	–	1	1	–	–	–	1	–	3	3	3	3
Overest. > 0.1–0.2	–	1	1	–	1	2	1	1	6	4	2	4	–	–	1	1	–	1	3	–	–	–	1	1	–	1	1	–
Underest. < 0.1–0.2	2	2	8	3	2	3	3	4	2	2	–	1	2	4	3	–	3	6	1	1	–	4	2	–	1	2	1	3
Underest. < 0.2	–	–	–	1	2	2	2	2	–	–	–	1	1	1	1	4	–	–	–	1	1	–	1	2	1	1	1	1
Tendency	+	+	–	–	–	–	–	–	+	+	+	+	–	–	–	–	–	–	+	–	–	–	–	–	+	+	+	+

[a]Seasons: 1, D, J, F; 2, M, A, M; 3, J, J, A; and 4, S, O, N. Considering temporal mismatches and biases for the regional representation, only counts for large overestimates (for overestimates larger than 0.1–0.2 and for overestimates larger than 0.2) and large underestimates (for underestimates smaller than 0.1–0.2 and for underestimates smaller than 0.2) are given. AOT tendencies by quarter are indicated.

[118] 2. In urban outflow regions all three satellites usually generally agree with each other. MODIS, with slightly smaller values for the North Atlantic, has the superior cloud-screen. Choice is MODIS.

[119] 3. In dust source regions, TOMS averages are always larger than MODIS averages. MODIS retrievals fail over high reflecting surface (e.g., deserts) and missed large dust events in MODIS probably contribute to lower regional averages. Choice is TOMS.

[120] 4. In dust outflow regions, TOMS averages are larger than those of the other two satellite data sets. MODIS with the lowest values matches better with AERONET. Choice is MODIS.

[121] 5. In biomass source regions, TOMS suggests significantly larger averages than MODIS, in part because of a relatively high background level during the wet (off-) season. Choice is MODIS.

[122] 6. In biomass outflow regions and remote regions, TOMS and at times AVHRR retrievals are significantly larger than MODIS. In areas of low aerosol optical depth the impact of poor cloud screening is amplified. Also another AVHRR retrieval with a sophisticated and more consistent cloud-screen [*Stowe et al.*, 2002] for the same NOAA-9 data set agrees well with MODIS. Choice is MODIS.

[123] In summary, for model evaluations MODIS will be reference only replaced by TOMS near dust sources.

[124] Comparison of simulated yearly averages to satellite of Figure 21 and comparisons of seasonality are quantified in Appendix B. A brief summary with a distinction by aerosol class is given in Table 17. For an agreement the simulated yearly average optical depth had to remain within 15%, 20% and 30% of the regional average of the reference satellite data, at source, outflow and remote regions, respectively. Larger errors in outflow and remote regions were necessary to account for the influence of year-to-year variations. Seasonality phase was considered agreeable ($\sim$) when the month associated with the maximum of the three-month running average (for the optical depth) did not differ by more than one month from that of the satellite.

[125] All models (though at different degree) underestimate aerosol optical depth compared to satellite data. This is even valid with respect to the (relative aerosol optical depth weak) MODIS/TOMS reference data set. It could be argued, that this tendency is not necessarily a modeling problem, as MODIS and especially TOMS, as shown in Table 15, have biases toward larger aerosol optical depths in comparisons to AERONET. In particular, low seasonal minima (aerosol optical depths below 0.1) are rarely retrieved. For TOMS and also AVHRR this discrepancy is largely caused by cloud contamination. For MODIS, the discrepancies with AERONET minima are largest in areas with potential for partial snow cover. Still, aside from snow contamination, sampling issues can also explain differences. MODIS can detect between cloud-gaps, where aerosol optical depths are usually larger than under completely cloud-free conditions, which AERONET prefers. More detailed comparisons are needed to settle this issue.

[126] On the basis of matches to the reference satellite data for yearly and regional averages, Grantour and GOCART do best. For almost half of the 20 regions both models achieve overall agreement in both yearly average and seasonality phase. Grantour excels in regions dominated by urban and biomass aerosol, while GOCART excels in regions dominated by dust. Both models do also better in remote regions. Here all models, at times severely under-predict aerosol optical depth and only Grantour comes close. Comparisons to AVHRR [see also *Penner et al.*, 2002] and TOMS are worse, in part because clouds contaminate in retrievals. Grantour achieves the better aerosol optical matches to MODIS in remote regions by assuming smaller sizes for

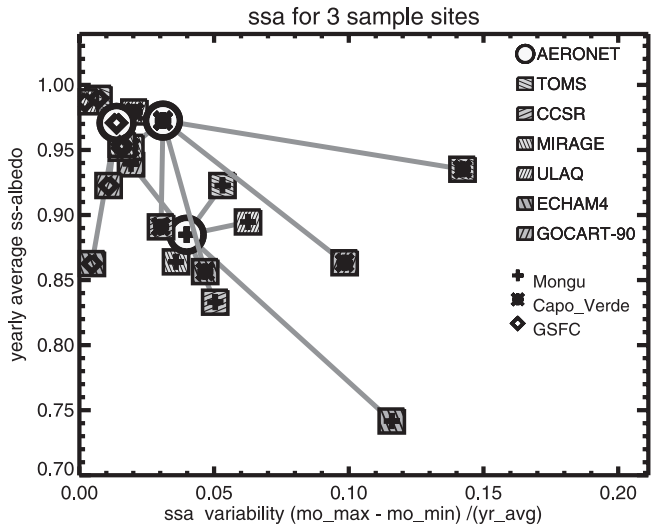

Figure 20. Comparison of simulated single-scattering albedos for three sample sites for biomass burning season aerosol (Mongu), for dust-outflow aerosol (Cape Verde) and for urban aerosol (GSFC). See color version of this figure in the HTML.

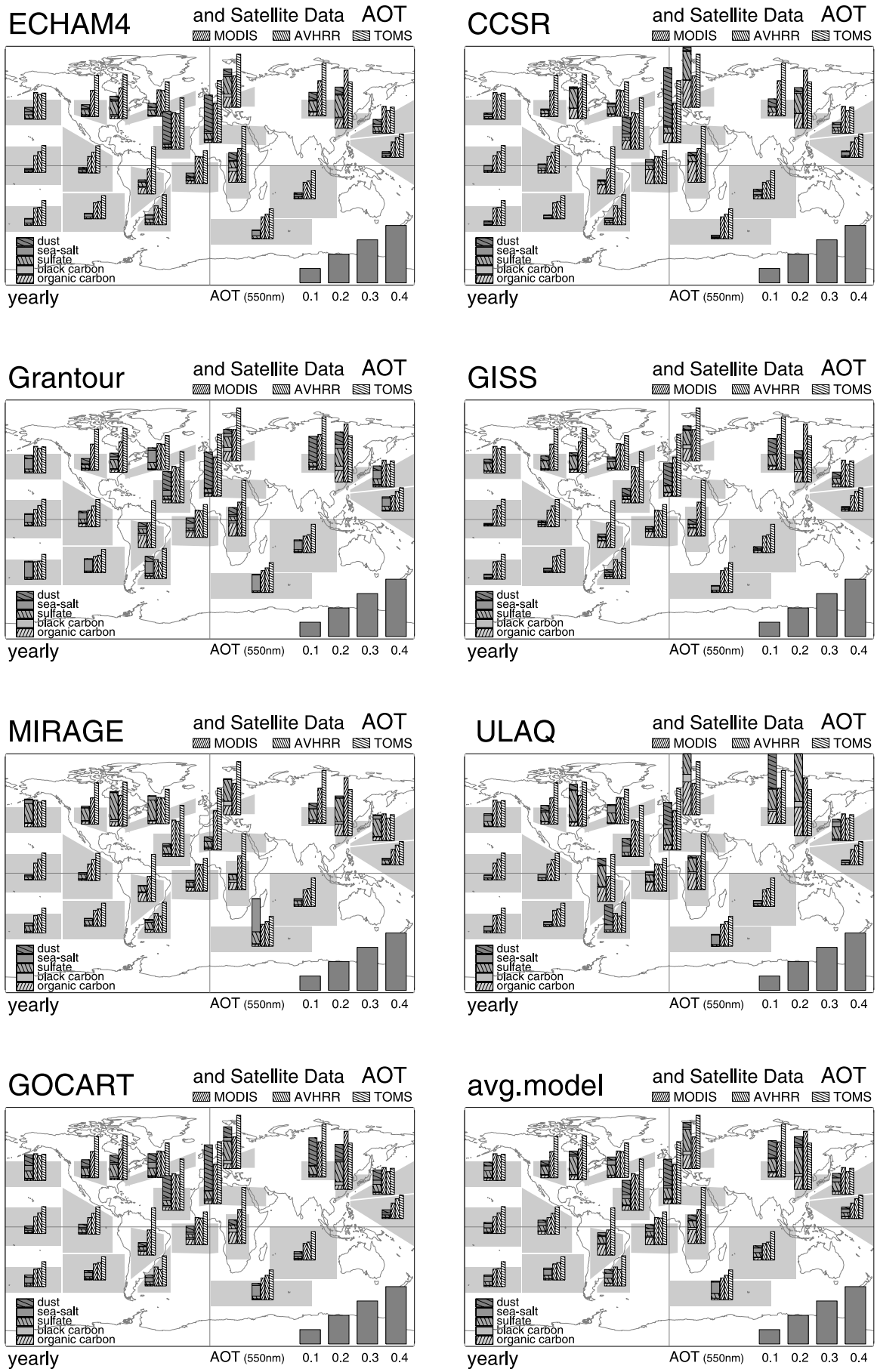
ECHAM4
and Satellite Data AOT
MODIS AVHRR TOMS
dust
sea-salt
sulfate
black carbon
organic carbon
yearly
AOT (550nm) 0.1 0.2 0.3 0.4
CCSR
and Satellite Data AOT
MODIS AVHRR TOMS
dust
sea-salt
sulfate
black carbon
organic carbon
yearly
AOT (550nm) 0.1 0.2 0.3 0.4
Grantour
and Satellite Data AOT
MODIS AVHRR TOMS
dust
sea-salt
sulfate
black carbon
organic carbon
yearly
AOT (550nm) 0.1 0.2 0.3 0.4
GISS
and Satellite Data AOT
MODIS AVHRR TOMS
dust
sea-salt
sulfate
black carbon
organic carbon
yearly
AOT (550nm) 0.1 0.2 0.3 0.4
MIRAGE
and Satellite Data AOT
MODIS AVHRR TOMS
dust
sea-salt
sulfate
black carbon
organic carbon
yearly
AOT (550nm) 0.1 0.2 0.3 0.4
ULAQ
and Satellite Data AOT
MODIS AVHRR TOMS
dust
sea-salt
sulfate
black carbon
organic carbon
yearly
AOT (550nm) 0.1 0.2 0.3 0.4
GOCART
and Satellite Data AOT
MODIS AVHRR TOMS
dust
sea-salt
sulfate
black carbon
organic carbon
yearly
AOT (550nm) 0.1 0.2 0.3 0.4
avg.model
and Satellite Data AOT
MODIS AVHRR TOMS
dust
sea-salt
sulfate
black carbon
organic carbon
yearly
AOT (550nm) 0.1 0.2 0.3 0.4

Table 17. Agreement to Satellite Data in 20 Regions: Matches in Terms of Yearly Average and Seasonality for Aerosol Optical Depth[a]

	AOT Versus Satellite							
	EC (>, ∼, <)	GO (>, ∼, <)	MI (>, ∼, <)	GI (>, ∼, <)	CC (>, ∼, <)	Gr (>, ∼, <)	UL (>, ∼, <)	Permitted Deviation (∼)
Urban source (2)	–, **1**, 1	1, –, 1	–, **1**, 1	–, ***1***, 1	1, –, 1	0, ***2***, 0	2, –, 0	M ± 15%
Off urban (4)	–, –, 4	, ***4***, –	–, ***2***/**2**, –	–, –, 4	0, **1**, 3	0, **2**, 2	0, **1**, 3	M ± 20%
Dust source (2)	–, –, 2	–, ***2***, –	–, –, 2	–, –, 2	1, –, 1	–, –, 2	1, –, 1	T ± 15%
Off dust (1)	–, **1**, –	–, ***1***, –	–, –, 1	–, –, 1	–, ***1***, –	–, **1**, –	–, –, 1	M ± 20%
Biomass source (2)	–, **1**, 1	–, –, 2	–, –, 2	–, –, 2	–, **1**, 1	–, ***2***, –	1, ***1***, –	M ± 20%
Off biomass (3)	–, –, 3	–, –, 3	–, –, 3	–, –, 3	–, **1**, 2	–, ***3***, –	1, –, 2	M ± 25%
Remote, S. Hemis. (3)	–, –, 3	–, **1**, 2	–, –, 1	–, –, 3	–, –, 3	–, ***2***/**1**, –	–, –, 3	M ± 30%
Remote, trop. (3)	–, –, 3	–, **3**, –	–, –, 3	–, –, 3	–, –, 3	–, **3**, –	–, –, 3	M ± 30%
Matches (20)	0	7	2	1	1	9	1	

[a]For class-combined regions (see Table 7), matches (bold) and mismatches in yearly average are given. Permitted deviations from MODIS (M) or TOMS (T) are indicated in the right column. Matches that also agreed in seasonality timing (bold-italic) are added up in the last line.

sea salt, which more efficiently turn mass into optical depth. This raises the question, if all other models assume too large sizes for sea salt. This is one of many open questions to be addressed in subsequent and more detailed model evaluations. More details on individual model tendencies with respect to the reference satellite data set and with respect to the median model are summarized in section 2.2.5.

[127] Against the overall trend most models match and over-predict aerosol optical depth for Europe. This unusual trend over Europe, however, could be related to the use of older emission data for Europe. Older emission data for Europe overestimate source strength, compared to 2001, the year of the MODIS retrievals. This emphasizes the need for appropriate emission data.

[128] To focus on seasonal differences with the reference satellite data set, simulated aerosol optical depths of all models are compared for the central month of each season (January, April, July and October) in Figure 22. Explanations for commonly larger satellite data vary. For January the larger satellite data over North America could be related to contamination by snow on the ground and those over South America could be related to an extended biomass season. Larger satellite data in April for the Northern Hemisphere are probably related to underestimates in dust transport from Asia in many models. Differences are less severe for July and October, although differences in tropical biomass regions the model predicted seasonal peak is often too early and too weak.

[129] In summary, satellite data are essential for the evaluation of global models. Satellite data, however, are only (quantitatively) of use if their limitations and assumptions are taken into account.

[130] The currently most accurate global aerosol satellite data set (from a combination of MODIS and TOMS) suggests that most models underestimate aerosol optical depth. Mismatches in regional comparisons are more common than matches. This should not diminish a good seasonal agreement of many models for particular regions. When differences to satellite data occur, it is often difficult to judge whether the model or satellite is at error. Here a strengthening of satellite data with other satellite data or ground data would help, if those are available. For instance, there is a lack of data from ground stations in remote oceanic regions of the Southern Hemisphere to help understand why in those regions retrieved aerosol optical depths are much larger than simulations. Aside from optical depth there are also satellite retrievals of other aerosol properties, which can help in the evaluation of global models. Incorporating information on size (e.g., MODIS distinguish between coarse and fine mode fractions), absorption (e.g., TOMS provides estimates on the single-scattering albedo) and composition (e.g., CO concentration of MOPPIT could identify pollution) will be a challenge to future model evaluations.

4. Conclusions

[131] New aerosol modules were evaluated. These modules separately process at least five different aerosol types (sulfate, organic carbon, black carbon, sea salt and dust). Comparison of simulations for aerosol mass and aerosol optical depth revealed model specific behavior. Major tendencies by model are as follows: (1) ECHAM4 has unusual high dust contributions off Africa around April and sea-salt contributions are weak, because assumed sea-salt sizes are too large. (2) GOCART has the strongest intercontinental transport for carbon and dust. (3) MIRAGE has strong sulfate contributions, weak tropical sources and unusual maxima at polar midlatitudes, where relative humidity is usually higher. (4) GISS has weak contributions from all components except sulfate and issues for the conversion of mass into optical depth (e.g., sulfate sizes too large, dust sizes are often too small and with conversion constants no size variability is permitted for carbon and sea salt). (5) CCSR has a weak intercontinental transport for dust and carbon. (6) Grantour has the largest optical depth in remote regions, mainly because of an assumption of relatively small sizes for sea salt. (7) ULAQ has very strong sulfate and carbon sources in urban regions and weak transport for black carbon.

[132] To what degree these tendencies reflect a skill or a deficiency must be decided in evaluations to measurements. Aerosol optical depth data based on remote sensing data from ground and space are available. However, these

Figure 21. (opposite) Yearly and regionally averaged aerosol optical depths of retrievals from MODIS, AVHRR and TOMS. Satellite data are compared to (component) simulations with individual models and an 'average model. See color version of this figure in the HTML.

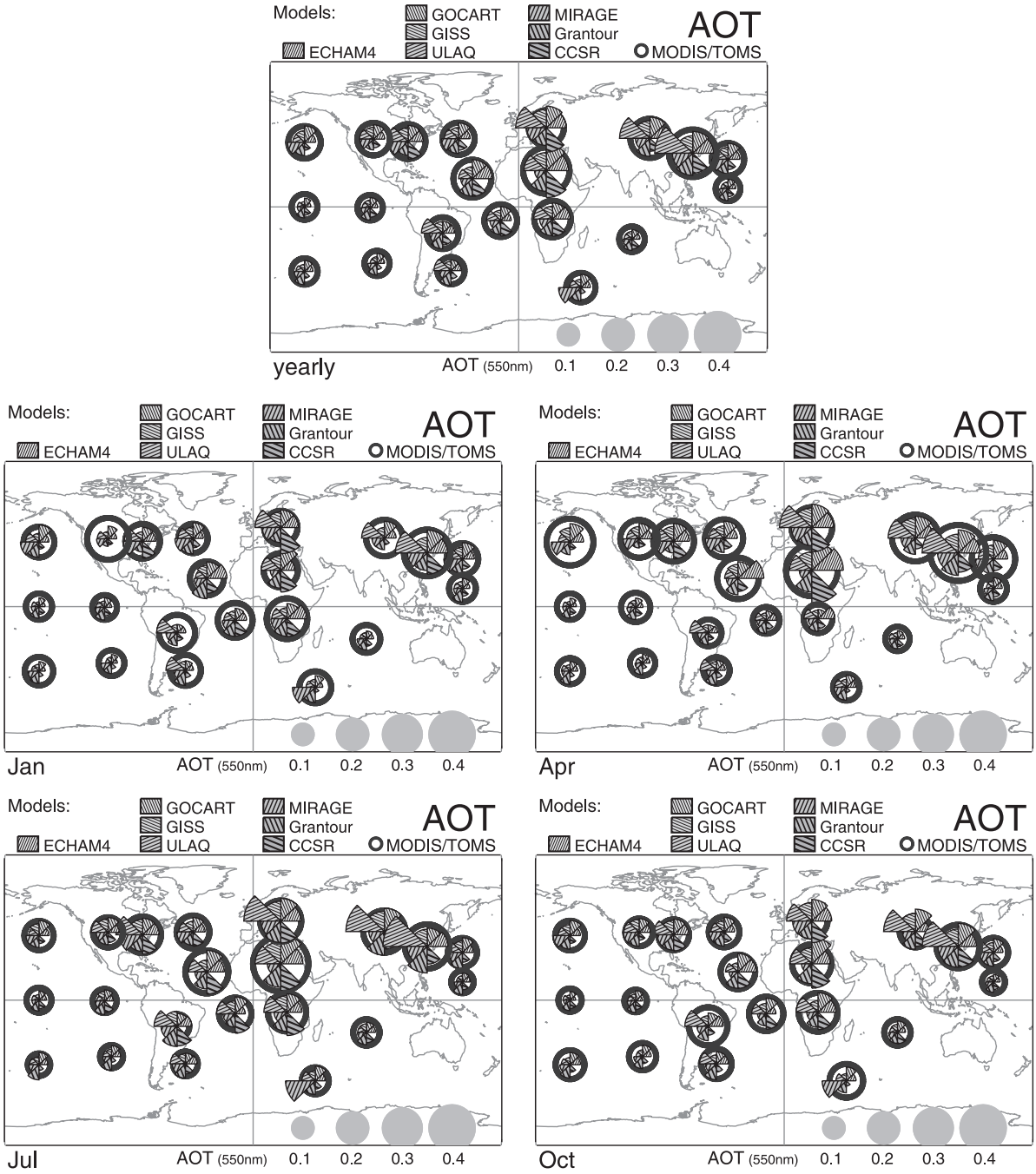

Figure 22. Regional comparisons of simulated (outer pie-section border) and satellite retrieved (circle) aerosol optical depths. Satellite data are a combination of MODIS (1.choice) and TOMS (2.choice). Aside from yearly averages in the top panel, averages for the months of January, April, July and October are presented, to illustrate seasonal differences. See color version of this figure in the HTML.

measurements have limitations of their own (e.g., a-priori assumptions, lack of global coverage or a lack of regional representation) and type-combined properties usually reveal little about the treatment of a particular aerosol type. Thus model evaluations apply only in rather general terms.

[133] Comparisons to ground-based statistics of AERONET are mixed. For many sites regional representation issues could not be settled, despite the use of satellite data. However, larger deviations to AERONET, especially for sites and seasons where one aerosol type dominates, clearly demonstrate that many models miss seasonal strength or timing for biomass and dust.

[134] Comparisons to a satellite data set, which combines the best of MODIS and TOMS, indicate that models tend to underestimate optical depth. The use of older emission data may be the reason, why this common trend is not observed over Europe. Many underestimates to satellite data seem related to model deficiencies for source strength and trans-

port. Less clear are reasons for consistently lower model simulations for remote regions of the tropics and the Southern Hemisphere.

[135] This study served two purposes. It was intended to provide a glimpse into the problems and uncertainties of climate simulations with aerosol and to convey the message for the need of measurements, on which the skill of these models can be tested. On the other hand this study provides feedback to the models that have participated in this comparison. In fact, as a result of this comparison, several assumptions regarding the representation of aerosol in some models were or are currently modified. As biases often can be traced back to one aerosol type, it can be expected that performances of some models could drastically improved with few modifications. Still, many model tendencies are difficult to explain. For more insights on model behavior, a more coordinated approach is needed. This includes an stepped up effort for identical background data (assimilated meteorology and emission), added intermediate model output (e.g., surface winds, water uptake by type, vertical distributions, subsampling for time-matches to data), a willingness to perform sensitivity tests (e.g., tracer transport simulations, humidification with prescribed humidity fields), a consensus on assumptions for aerosol (e.g., absorption of dust and organic carbon, dust-size) and a review of radiative transfer schemes as to their appropriateness for aerosol studies.

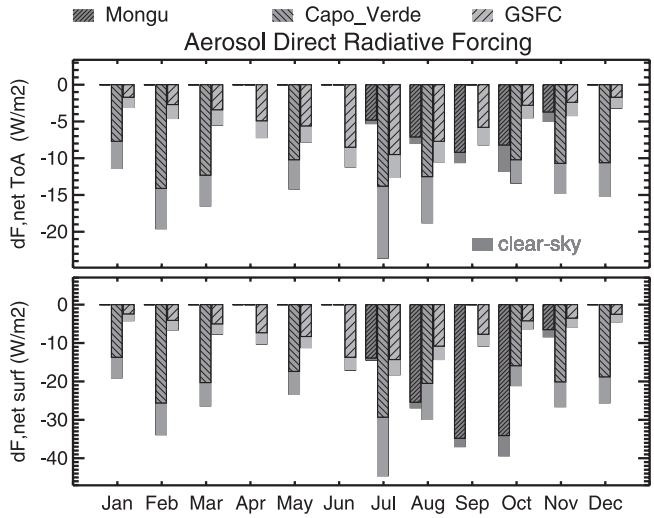

Figure A1. AERONET-derived aerosol forcing at sites representing biomass burning (Mongu, Jul-Nov), dust (Capo_Verde) and urban aerosol (GSFC). Radiative forcing monthly averages are given at the top of the atmosphere (upper panel) and at the surface (lower panel) for clear-sky conditions (grey bars) and under cloudy conditions (striped or colored bars). See color version of this figure in the HTML.

Appendix A: Direct Aerosol Forcing

[136] AERONET sky data completely define the aerosol optical properties (see Figures 13 and 14). Combining these data with smart choices to other atmospheric properties (as input to radiative transfer codes) the associated local direct radiative forcing for aerosol can be determined. Here, additional input to the model included monthly statistics for solar surface albedo from MODIS [*Schaaf et al.*, 2002] and for cloud cover from ISCCP [*Rossow et al.*, 1993]. For the three major AERONET sites of Figure 2 the calculated net-flux changes at the top of the atmosphere (ToA) and at the surface is presented in Figure A1.

[137] The aerosol radiative forcing at the top of the atmosphere (ToA) is always less negative than the associated forcing at the surface. This difference is mainly an indicator for the aerosol solar absorption (which is particularly large for aerosol from biomass burning). The consideration of clouds (versus a cloud-free scenario) usually reduces the aerosol forcing strength. Particularly important for the 'climate impact indicating' ToA forcing is the relative altitude placement between cloud and aerosol. Clouds below aerosol brighten the aerosol's underlying surface, similar to switching from ocean to desert or snow surfaces. Such brightening can change the sign of aerosol ToA forcing from a net flux loss (cooling) to a net flux gain (warming).

[138] Calculated aerosol forcing for all 20 AERONET sites of Table 13 and Figure 2 are summarized in Tables A1 and A2 for (ISCCP-) cloudy conditions. Three-month (seasonal) averages are usually presented. At sites strongly influenced by biomass burning, only monthly averages of the biomass peak season are given.

[139] The direct aerosol forcing at AERONET sites is usually larger than global forcing averages because of the proximity of AERONET sites to aerosol sources. In addition, when comparing to values of IPCC studies [e.g., *Houghton et al.*, 2001], it must be kept in mind that IPCC only addresses forcing from anthropogenic aerosol, whereas the results here include effects from natural aerosol. All calculated forcings carry some uncertainty with year-to-year variations in aerosol concentration (e.g., common occurrence of episodic events such as dust storms and shifts in onset and/or intensity of seasonal events such as a biomass burning seasons).

[140] At all 20 evaluated AERONET sites, aerosol reduces (on a seasonal basis) the available energy to the Earth-atmosphere system (negative ToA forcing). Associated reductions of surface net-fluxes are always larger, because of aerosol absorption. This atmospheric forcing heats aerosol layers and is particularly large for biomass and polluted urban aerosol. To what degree this added heating in the atmosphere influences the dynamics (less instability and/or suppressed convection and precipitation) is not completely understood.

Appendix B: Regional Comparisons

[141] Here, differences among models and to satellite data are compared individually for each region. Such comparison provides more detail than comparing averages of type-similar regions, as it was done in the text above for brevity (according to Table 7). Aerosol properties of mass, optical depth and optical depth compositional partition are compared for the 20 regions of Figure 2. Investigated properties are yearly average, seasonality strength and seasonality phase. Their definition is the same as in the text: Seasonality strength is the ratio between the (maximum-minimum) range of the three-month running average during a year

Table A1. Direct (All-Sky) Aerosol Forcing at AERONET Sites on a Seasonal Basis

	Lat, N	Lon, E	Forcing, W/m^2 Top of Atmosphere DJF	MAM	JJA	SON	Surface DJF	MAM	JJA	SON	Atmosphere DJF	MAM	JJA	SON
Dust														
Cape Verde	17	337	−11	−11	−13	−11	−20	−19	−25	−19	9	8	12	8
Banizoumbou	14	3	−6	−9	−4	−8	−14	−27	−21	−18	8	18	17	10
Ilorin	8	4	−12	−10	−7	−9	−55[b]	−24	−21	−17	43[b]	14	14	8
Sede Boker	31	34	−4	−6	−5	−5	−6	−11	−9	−9	2	5	4	4
Bahrain	26	50	−5	−11	−11	−8	−8	−19	−23	−12	3	8	12	4
Dalanzadgad	44	104	0	−8	−2	−1	−14	−20	−8	−11	14	12	6	10
Urban/Rural														
GSFC	39	283	−2	−5	−9	−4	−3	−7	−13	−6	1	2	4	2
Ispra	46	9	−3	—	−6	−8	−4	—	−14	−15	1	—	8	7
Mexico City	19	261	—	−5	−3	—	—	−23	−14	—	—	18	12	—
Bondville	40	272	−1	−4	−9	−4	−2	−7	−13	−6	1	3	4	2
Sevilleta	24	253	−1	−3	−2	−1	−3	−6	−7	−7	2	3	5	6
Arica	18	310	−6	−5	−5	−5	−10	−9	−8	−8	4	4	3	3
Maritime														
Lanai	21	203	−3	−5	−2	−2	−4	−7	−4	−3	1	2	2	1
Dry Tortugas	25	277	−5	−8	−6	−2	−8	−12	−9	−6	3	4	3	2

[a]DJF, Dec/Jan/Feb; MAM, Mar/Apr/May; JJA, Jun/Jul/Aug; SON, Sep/Oct/Nov. Dashes indicate insufficient statistics.
[b]During DJF, "Ilorin" is strongly influenced by biomass aerosol (causing strong surface cooling and atmospheric forcing).

and the yearly average. Seasonality phase is identified by the (center-) months associated with the maximum and minimum of a three-month running average during a year.

B1. Aerosol Mass

[142] Regional mass comparisons of Table B1 quantify the comparisons of Figure 3 for yearly average and seasonality strength (or range). Table B2 compares the corresponding seasonality phase.

B2. Aerosol Optical Depth

[143] Regional aerosol optical depth comparisons of Table B3 quantify the comparisons of Figure 5 for yearly average and seasonality strength (or range). Table B4 compares the corresponding seasonality phase indicating central months, when the three-month running mean is at its maximum or minimum, respectively.

[144] Tables B3 and B4 also display statistics of three satellite data sets: MODIS, TOMS and AVHRR. To what degree these 'measured' aerosol optical depths can be used for model evaluations of aerosol modules depends largely on the accuracy in those satellite retrievals. At issue are the appropriateness of retrieval assumptions and the skill to remove scenes with clouds. Cloud-contamination issues are likely explanations for the relatively high aerosol optical depths in remote regions of TOMS (large pixel size) and of AVHRR (ISCCP climatology threshold). In contrast, multispectral data at subkilometer pixel size of MODIS are the basis of a superior cloud screen. Thus MODIS is the selected reference for model evaluations, except for dust source regions, where TOMS statistics replaces MODIS as reference. This is because MODIS retrievals fail over continental regions with relatively high solar surface reflectance (e.g., deserts). In addition, large dust events in MODIS retrievals are frequently mistaken as clouds and removed, leading to regional underestimates near dust sources.

[145] Compared to the best satellite product (MODIS with TOMS) all models tend to underestimate aerosol optical depth, as illustrated in Table B5. Particularly common are underestimates for outflow and remote regions. Less common are underestimates for source regions. Here many models match up quite well to satellite data and even a few model overestimates occur. In fact, over Europe almost all models suggest larger values than the satellite data. This unusual trend over Europe, however, could be related to the use of older emission data for Europe. Older emission data

Table A2. Direct (All-Sky) Aerosol Forcing at AERONET Sites During Months of Biomass Burning

	Lat, N	Lon, E	Forcing for Biomass, W/m^2 Top of Atmosphere July	Aug.	Sept.	Oct.	Surface July	Aug.	Sept.	Oct.	Atmosphere July	Aug.	Sept.	Oct.
Mongu	−15	23	−5	−7	−9	−8	−14	−25	−35	−34	9	18	26	26
Cuiaba	−15	304	−5	−9	−11	−6	−11	−34	−49	−19	6	25	38	13
Alta Floresta	−10	303	−5	−16	−17	−10	−8	−30	−48	−19	3	14	31	9
Conception	−16	298	−5	−12	−10	−10	−8	−26	−24	−18	3	14	14	8
			Forcing for High Latitude, W/m^2											
	Lat, N	Lon, E	Top of Atmosphere May	June	July	Aug.	Surface May	June	July	Aug.	Atmosphere May	June	July	Aug.
Waskesiu	54	254	−9	−16	−12	−7	−14	−34	−19	−9	5	18	7	2
HJ Andrews	44	238	−3	−4	−4	−3	−6	−7	−7	−5	3	3	3	2

Table B1. Simulations of Aerosol Mass for Regions of Figure 2: Yearly Average and Seasonality Strength[a]

	Mass (Yearly Average in g/m^2, Seasonality-Strength)						
	EC	GO	MI	GI	CC	Gr	UL
Urban source							
E. Asia	**.11**, *0.5*	**.20**, *0.7*	**.06**, *0.4*	**.06**, *0.4*	**.06**, *0.4*	**.13**, *1.0*	**.26**, *0.7*
Europe	**.11**, *0.6*	**.15**, *0.3*	**.05**, *0.5*	**.05**, *0.8*	**.06**, *0.5*	**.05**, *0.9*	**.09**, *0.3*
Urban outflow							
NW Atlantic	**.13**, *1.1*	**.12**, *0.3*	**.04**, *0.4*	**.03**, *0.6*	**.05**, *0.7*	**.05**, *0.6*	**.05**, *0.8*
NW Pacific	**.13**, *0.8*	**.13**, *0.5*	**.04**, *0.6*	**.04**, *0.6*	**.04**, *0.5*	**.06**, *0.5*	**.05**, *0.3*
N. Pacific	**.15**, *1.3*	**.44**, *0.4*	**.04**, *0.5*	**.04**, *0.6*	**.03**, *0.4*	**.04**, *0.3*	**.05**, *0.7*
Dust source							
N. Africa	**.34**, *1.6*	**.58**, *0.6*	**.06**, *0.6*	**.15**, *0.6*	**.73**, *1.6*	**.30**, *0.8*	**.24**, *0.6*
Asia	**.09**, *1.3*	**.32**, *0.6*	**.08**, *0.9*	**.11**, *1.3*	**.10**, *1.7*	**.22**, *1.4*	**.53**, *1.1*
Dust outflow							
E. Atlantic	**.29**, *0.8*	**.21**, *0.9*	**.04**, *0.6*	**.05**, *0.8*	**.18**, *1.3*	**.12**, *0.6*	**.10**, *0.9*
Biomass source							
Africa	**.10**, *1.3*	**.07**, *1.1*	**.02**, *0.7*	**.03**, *1.0*	**.05**, *1.1*	**.06**, *0.5*	**.04**, *1.1*
S. America	**.04**, *1.3*	**.05**, *1.0*	**.02**, *0.8*	**.02**, *0.9*	**.02**, *1.6*	**.04**, *0.7*	**.09**, *0.6*
Biomass outflow							
SE Atlantic	**.06**, *0.8*	**.07**, *1.0*	**.03**, *0.3*	**.02**, *0.7*	**.05**, *0.6*	**.03**, *0.5*	**.04**, *1.1*
SW Atlantic	**.11**, *1.0*	**.05**, *0.5*	**.03**, *0.3*	**.03**, *0.1*	**.02**, *0.6*	**.07**, *0.6*	**.23**, *0.7*
W. Pacific	**.07**, *0.5*	**.05**, *0.3*	**.02**, *0.4*	**.01**, *0.5*	**.03**, *0.4*	**.03**, *0.4*	**.02**, *0.9*
Remote, S. Hemis.							
S. Atlantic	**.19**, *1.0*	**.08**, *0.6*	**.03**, *0.1*	**.02**, *0.6*	**.02**, *0.8*	**.04**, *0.6*	**.06**, *0.7*
S. Pacific	**.13**, *1.3*	**.06**, *0.6*	**.02**, *0.2*	**.02**, *0.5*	**.03**, *1.0*	**.03**, *0.6*	**.03**, *0.5*
Remote, tropics							
Indian O.	**.08**, *1.2*	**.05**, *0.8*	**.02**, *0.1*	**.02**, *0.5*	**.04**, *1.1*	**.02**, *0.6*	**.03**, *0.7*
Mid-Pacific	**.04**, *0.5*	**.06**, *0.6*	**.02**, *0.2*	**.02**, *0.5*	**.03**, *1.1*	**.03**, *0.4*	**.03**, *0.5*
Other regions							
E. Pacific	**.04**, *0.5*	**.04**, *0.4*	**.02**, *0.2*	**.01**, *0.2*	**.03**, *0.2*	**.02**, *0.3*	**.02**, *0.2*
SE Pacific	**.34**, *1.6*	**.58**, *0.6*	**.06**, *0.6*	**.15**, *0.9*	**.73**, *1.6*	**.30**, *0.8*	**.24**, *0.6*
N. America	**.06**, *0.4*	**.09**, *0.3*	**.05**, *0.7*	**.04**, *0.8*	**.03**, *0.5*	**.04**, *0.8*	**.06**, *1.1*

[a]Data pairs by region indicate the yearly average in g/m^2 (first value, in bold) and the seasonality (second value, in italics) of each model. Models: ECHAM4, GOCART, MIRAGE, GISS, CCSR, Grantour, ULAQ.

Table B2. Simulations of Aerosol Mass for Regions of Figure 2: Seasonality Phase (Months of Maxima and Minima)[a]

	Mass (Seasonal Maximum–Seasonal Minimum)						
	EC	GO	MI	GI	CC	Gr	UL
Urban source							
E. Asia	**Jan–Nov**	**Jun–Feb**	**Apr–Jul**	**Apr–Jan**	*Jun–Feb*	**Jun–Jan**	***Jun–Feb***
Europe	**Mar–Sep**	***Mar–Sep***	*May–***Jan**	**May–Dec**	**Jun–Jan**	**Jul**–*Jan*	**Jul–Oct**
Urban outflow							
NW Atlantic	***Jan***–**Aug**	**Mar**–***Jul***	**Apr–Nov**	*Mar–Aug*	**Jan–Sep**	**Feb–Jul**	**Feb–Sep**
NW Pacific	***Jan***–**Aug**	**May**–***Oct***	**Apr–Jul**	**May**–*Sep*	*Dec*–**Aug**	**Jun–Oct**	**Feb–Sep**
N. Pacific	***Jan***–**Aug**	**May**–***Sep***	**Apr–Jul**	**Mar–Dec**	*Feb–Jul*	**Feb–Jul**	**Jan–Aug**
Dust source							
N. Africa	**May–Dec**	**May**–***Jan***	*May–Jan*	**Jun–Dec**	***May***–**Dec**	**Jul–Jan**	**Jul–Dec**
Asia	**May–Dec**	**Jun–Jan**	*Jun–***Jan**	**Jun–Jan**	**Aug**–*Feb*	**Jul–Jan**	***Jul–Feb***
Dust outflow							
E. Atlantic	***Mar–Oct***	**Jul–Dec**	*Jan–***Oct**	**Mar**–*Oct*	**Jul–Dec**	**Aug–May**	**Jul–Nov**
Biomass source							
Africa	***Feb–Nov***	**Aug–May**	*Jan–***May**	**Jul**–*Apr*	**Jul–Apr**	**Feb–May**	**Sep–Apr**
S. America	**Aug–Jan**	**Sep–Apr**	*Jul–***Mar**	**Aug–Feb**	**Jul**–*Feb*	**Aug–Apr**	***Oct–Apr***
Biomass outflow							
SE Atlantic	**Mar–Nov**	***Aug–Dec***	**Jul–Apr**	*Aug–Apr*	**Jul–Apr**	**Aug–Oct**	**Jul–Mar**
SW Atlantic	**Jul–Jan**	**Oct–Mar**	**Dec–May**	**Nov–Feb**	*Jul–Feb*	**Dec–Jun**	***Dec–Jul***
W. Pacific	***Jan–Sep***	**Jul–Nov**	**Apr–Aug**	*Mar–Aug*	**Jan–Sep**	**Jan–Oct**	**Feb–Jul**
Remote, S. Hemis.							
S. Atlantic	***Jul–Jan***	**Aug–Jan**	*Aug–***Jun**	**Jul–Nov**	**Jul**–*Feb*	**Aug–Nov**	**Jul–Dec**
S. Pacific	***Jul–Jan***	**Aug–Feb**	**Jan–Jul**	*Aug–Apr*	**Oct–Feb**	**Aug–Apr**	**Aug–Dec**
Remote, tropics							
Indian O.	***Jul–Jan***	**Aug–Mar**	**Aug–May**	*Oct–May*	**Oct–Feb**	**Jul–Dec**	**Aug–Dec**
Mid–Pacific	***Jul–Oct***	**Aug–Nov**	**Jan–Oct**	*Mar–May*	**Jul–Mar**	**Aug–Nov**	**Sep–Dec**
Other regions							
E. Pacific	**Jul–Dec**	***Aug–Jan***	**Jul–Nov**	*Mar–Dec*	**Aug–Jan**	**Aug–Nov**	**Jan–Jul**
SE Pacific	**May–Dec**	**May**–***Jan***	*May–Jan*	**Jun–Dec**	***May***–**Dec**	**Jul–Jan**	**Jul–Dec**
N. America	**May–Nov**	***May–Sep***	**May–Jan**	**Jun**–*Jan*	*Jul*–**Jan**	**Jul–Mar**	**Nov**–*Apr*

[a]Italics indicate the regional maxima and minima among all models. Models: ECHAM4, GOCART, MIRAGE, GISS, CCSR, Grantour, ULAQ.

Table B3. Simulations of Aerosol Optical Depth for Regions of Figure 2: Yearly Average and Seasonality Strength[a]

	Aerosol Optical Thickness (Yearly Average in g/m^2, Seasonality-Strength)									
	EC	GO	MI	GI	CC	Gr	UL	MO	TO	AV
Urban source										
E. Asia	**.29**, *0.4*	**.33**, *0.4*	**.28**, *0.2*	**.22**, *0.2*	**.28**, *0.3*	***.37***, *0.8*	**.97**, *0.6*	**.41**, *0.5*	**.27**, *0.3*	
Europe	**.27**, *0.4*	**.33**, *0.5*	***.25***, *0.4*	***.25***, *0.8*	**.42**, *0.3*	***.22***, *0.7*	**.63**, *0.7*	**.23**, *0.6*	**.30**, *0.2*	
Urban outflow										
NW Atlantic	**.09**, *0.4*	***.17***, *0.4*	***.20***, *0.6*	**.09**, *0.3*	**.09**, *0.6*	**.16**, *0.6*	**.13**, *0.3*	**.19**, *0.5*	**.24**, *0.3*	**.20**, *0.3*
NW Pacific	**.10**, *0.7*	***.17***, *0.6*	***.18***, *0.8*	**.10**, *0.6*	**.08**, *0.4*	**.15**, *0.5*	**.15**, *0.1*	**.19**, *0.8*	**.18**, *0.2*	**.19**, *0.5*
N. Pacific	**.08**, *0.6*	***.18***, *0.4*	***.19***, *0.6*	**.10**, *0.9*	**.04**, *0.5*	**.12**, *0.5*	**.09**, *0.5*	**.19**, *0.9*	**.18**, *0.3*	**.20**, *0.4*
Dust source										
N. Africa	**.33**, *1.5*	***.44***, *0.5*	**.09**, *0.5*	**.23**, *0.8*	**.52**, *1.3*	**.31**, *0.7*	**.33**, *0.5*	**.28**, *0.7*	**.40**, *0.9*	
Asia	**.16**, *0.8*	***.30***, *0.6*	**.14**, *0.4*	**.22**, *0.1*	**.12**, *1.3*	**.23**, *1.3*	**.62**, *0.9*	**.28**, *0.4*	**.30**, *0.9*	
Dust outflow										
E. Atlantic	***.26***, *0.8*	***.24***, *0.6*	**.09**, *0.6*	**.10**, *0.8*	**.22**, *0.8*	**.22**, *0.5*	**.13**, *0.9*	**.26**, *0.5*	**.36**, *0.7*	**.27**, *0.2*
Biomass source										
Africa	**.21**, *0.7*	**.18**, *1.2*	**.02**, *0.8*	**.12**, *1.0*	**.21**, *1.2*	**.20**, *0.7*	***.24***, *1.1*	**.25**, *0.8*	**.28**, *0.2*	
S. America	**.10**, *1.4*	**.10**, *1.5*	**.11**, *0.8*	**.10**, *1.3*	**.10**, *1.8*	***.18***, *1.0*	**.30**, *0.6*	**.18**, *1.0*	**.25**, *0.5*	
Biomass outflow										
SE Atlantic	**.07**, *0.7*	**.13**, *1.3*	**.08**, *0.6*	**.08**, *0.9*	***.17***, *1.2*	**.14**, *0.5*	**.13**, *1.1*	**.19**, *0.5*	**.23**, *0.3*	**.22**, *0.2*
SW Atlantic	**.07**, *0.8*	**.08**, *0.5*	**.09**, *0.6*	**.06**, *0.4*	**.05**, *0.5*	***.16***, *0.2*	**.19**, *0.6*	**.14**, *0.5*	**.21**, *0.2*	**.16**, *0.2*
W. Pacific	**.04**, *0.6*	**.06**, *0.6*	**.05**, *0.4*	**.03**, *0.5*	**.05**, *0.2*	***.10***, *0.5*	**.03**, *0.5*	**.11**, *0.4*	**.16**, *0.1*	**.18**, *0.3*
Remote, S. Hemis.										
S. Atlantic	**.06**, *0.6*	**.12**, *0.5*	**.33**, *1.3*	**.05**, *0.6*	**.03**, *1.1*	***.13***, *0.4*	**.08**, *0.7*	**.15**, *0.6*	**.21**, *0.2*	**.20**, *0.3*
S. Pacific	**.05**, *0.9*	**.08**, *0.5*	**.07**, *0.5*	**.04**, *0.4*	**.03**, *1.0*	***.13***, *0.6*	**.05**, *0.4*	**.13**, *0.6*	**.17**, *0.1*	**.17**, *0.2*
Remote, tropics										
Indian O.	**.04**, *0.8*	**.06**, *0.8*	**.05**, *0.3*	**.04**, *0.6*	**.07**, *0.9*	**.09**, *0.5*	**.04**, *0.4*	**.12**, *0.4*	**.20**, *0.2*	**.17**, *0.1*
Mid-Pacific	**.03**, *0.5*	**.05**, *0.6*	**.03**, *0.2*	**.02**, *0.3*	**.05**, *1.1*	**.09**, *0.2*	**.03**, *0.1*	**.12**, *0.2*	**.19**, *0.1*	**.18**, *0.3*
Other regions										
E. Pacific	**.04**, *0.7*	**.07**, *0.4*	**.06**, *0.2*	**.04**, *0.8*	**.06**, *0.7*	***.11***, *0.4*	**.04**, *0.2*	**.12**, *0.3*	**.19**, *0.1*	**.18**, *0.1*
SE Pacific	**.04**, *0.7*	**.07**, *0.6*	**.06**, *0.5*	**.03**, *0.5*	**.03**, *0.7*	***.10***, *0.6*	**.03**, *0.7*	**.11**, *0.4*	**.16**, *0.1*	**.17**, *0.1*
N. America	**.16**, *0.5*	**.18**, *0.4*	**.24**, *0.7*	**.14**, *0.6*	***.22***, *0.5*	**.13**, *0.8*	**.29**, *0.7*	**.22**, *0.5*	**.31**, *0.3*	

[a]Data pairs by region for model or satellite indicate the yearly average (first value, in bold) and the seasonality (second value, in italics). Models: ECHAM4, GOCART, MIRAGE, GISS, CCSR, Grantour, ULAQ; Satellites: MODIS, TOMS, AVHRR (oceans only).

Table B4. Simulations of Aerosol Optical Depth for Regions of Figure 2: Seasonality Phase (Months of Maxima and Minima)[a]

	Aerosol Optical Thickness (Seasonal Maximum–Seasonal Minimum)									
	EC	GO	MI	GI	CC	Gr	UL	MO	TO	AV
Urban source										
E. Asia	**Apr–Nov**	**Mar**–Jul	Oct–Jun	**Apr**–Feb	**Jun**–Nov	**Jun**–Jan	**Jun**–Jan	***May–Nov***	Apr–Dec	
Europe	May–Jan	**Aug–Jan**	May–Jan	**Jun–Dec**	Dec–Jul	**Jul–Jan**	**Jul**–Nov	***Jul–Jan***	Dec–Oct	
Urban outflow										
NW Atlantic	**Apr–Sep**	**Mar**–Jul	**Mar–Sep**	**May–Aug**	Jun–Jan	Feb–Aug	Feb–Oct	***Apr–Sep***	Mar–Nov	Mar–Dec
NW Pacific	**Apr–Oct**	**Apr–Sep**	Feb–Aug	**May–Sep**	**May–Oct**	Jun–Sep	Dec–Mar	***Apr–Sep***	Mar–Oct	Mar–Aug
N. Pacific	**May–Aug**	**Apr–Aug**	**Apr–Aug**	**May**–Dec	Jun–Jan	Dec–Aug	Jan–Jul	***Apr–Jul***	Apr–Jan	Apr–Aug
Dust source										
N. Africa	May–Dec	**Aug–Jan**	**Jul–Nov**	**Jul–Dec**	May–Dec	**Jul–Jan**	**Jul–Dec**	Aug–Dec	***Jun–Dec***	
Asia	**May–Dec**	**Jun–Jan**	**Jun–Dec**	**Jun–Jan**	Aug–Jan	Jul–Jan	Jul–Jan	Sep–Nov	***May–Dec***	
Dust outflow										
E. Atlantic	Mar–Oct	**Jul–Dec**	Jan–Oct	Mar–Oct	**Jul–Dec**	Feb–May	**Jul–Dec**	***Jul–Nov***	Jul–Nov	Jun–Feb
Biomass source										
Africa	Feb–Jul	**Sep–Apr**	Jan–May	**Aug–Apr**	Jul–Apr	**Aug–May**	**Aug**–Mar	***Sep–May***	Feb–May	
S. America	**Sep**–Feb	**Sep**–Mar	Jul–Mar	**Aug**–Mar	Jul–Mar	**Aug**–Dec	**Sep**–Apr	***Sep–Jun***	Sep–Jun	
Biomass outflow										
SE Atlantic	**Feb**–Nov	Aug–Apr	**Jan**–Oct	Aug–Apr	Aug–Apr	**Feb**–Oct	Aug–Mar	***Jan–May***	Jan–May	Aug–Apr
SW Atlantic	**Sep**–Jan	**Sep**–Feb	Aug–Apr	Jul–Apr	Jul–Feb	**Sep**–Mar	Dec–Jul	***Oct–Jun***	Sep–May	Oct–Jul
W. Pacific	May–Nov	Mar–Oct	Apr–Sep	Mar–Sep	Mar–Oct	**Feb**–Oct	**Jan–Jul**	***Jan–Jun***	Jul–Mar	Jan–Aug
Remote, S. Hemis.										
S. Atlantic	Aug–Jan	Aug–Feb	Aug–Apr	Jul–Nov	Jul–Feb	Feb–Nov	Jul–Dec	***Nov–May***	Jun–Apr	Jan–Jul
S. Pacific	Sep–Jan	Aug–Feb	Dec–Apr	Aug–Apr	**Oct–Jun**	Jul–Jan	Aug–Dec	***Oct–Jun***	Oct–May	Oct–Jul
Remote, tropics										
Indian O.	**Aug**–Dec	**Sep**–Feb	Dec–May	**Aug–Apr**	**Oct**–Feb	**Aug**–Nov	**Aug**–Dec	***Sep–May***	Aug–Jan	Sep–Jan
Mid-Pacific	Jul–Nov	Aug–May	**Jan–Sep**	Aug–Dec	Aug–Feb	**Feb**–Nov	Aug–Nov	***Jan–Aug***	Jun–Feb	Jan–Sep
Other regions										
E. Pacific	Aug–Nov	Aug–Mar	Jan –Oct	Aug–Dec	Jul–Dec	Aug–Nov	Jan–Jun	***May–Oct***	Apr–Sep	May–Nov
SE Pacific	Aug–Jan	Sep–Feb	**Dec–May**	Aug–Apr	**Nov–May**	Jul–Dec	Aug–Dec	***Nov–Jun***	Aug–May	Oct–Jun
N. America	Jul–Jan	**Apr**–Jan	Jul–Nov	**Jun**–Jan	Aug–Nov	Jul–Jan	Jul–Feb	***May–Nov***	Aug–Dec	

[a]For the 20 regions of Figure 2, months of maximum (left) and minimum (right) aerosol optical depth are displayed. Bold type indicates model simulations whose maxima (or maxima and minima) differ by less than two months from extremes (bold, italic type) of the "best" satellite data (MODIS, except for TOMS over dust sources). Models: ECHAM4, GOCART, MIRAGE, GISS, CCSR, Grantour, ULAQ; Satellites: MODIS, TOMS, AVHRR.

Table B5. Agreement to Satellite Data in 20 Regions (of Figure 2): Simulated Aerosol Optical Depths[a]

	AOT Versus Satellite Data						
	EC (>, ∼, <)	GO (>, ∼, <)	MI (>, ∼, <)	GI (>, ∼, <)	CC (>, ∼, <)	Gr (>, ∼, <)	UL (>, ∼, <)
Yearly average	0, ***2***, *18*	*1*, ***8***, *11*	*1*, ***5***, *14*	*0*, ***1***, *19*	*2*, ***4***, *14*	*0*, ***16***, *4*	*6*, ***2***, *12*
Seasonality phase (max)	***9***	***13***	***7***	***11***	***6***	***10***	***8***
Average + phase	0	7	2	1	1	9	1

[a]Investigated properties are yearly average and seasonality phase. For the comparison of yearly averages a distinction was made between clearly larger values (>), clearly smaller values (<) and general agreement (∼). For general agreement the simulated optical depths had to remain within 15%, 20% and 30% of the regional average of the satellite data, at source, outflow, and remote regions, respectively. Larger errors in outflow and remote regions were necessary to account for the influence of year-to-year variations. Seasonality phase was considered agreeable (∼) when the month with the maximum the three-month running average (for the optical depth) did not differ by more than one month from that of the satellite. Here, satellite data refer to MODIS retrievals, except for dust source regions, where TOMS data fill in. Also given is the count of 20 regions where both properties matched satellite data.

for Europe overestimate source strength, compared to 2001, the year of the MODIS retrievals.

[146] Looking for matches to satellite data in terms of all three optical depth properties (yearly average, seasonality strength and seasonality phase) we find on a model-by-model basis: (1) ECHAM4 has no regional matches (dust outflow average match has incorrect seasonality). (2) GOCART has regional matches at dust sources, dust outflow and urban outflow regions. (3) MIRAGE has regional matches only at higher-latitude regions of the Northern Hemisphere. (4) GISS has a regional match only for Europe. (5) CCSR has no regional match (biomass outflow average match has incorrect seasonality). (6) Grantour has regional matches for biomass source, urban source and urban outflow regions. (7) ULAQ has a regional for N. Africa (but only because of high sulfate and carbon contributions).

B3. Aerosol Composition

[147] Regional aerosol optical depth partitioning varies by model, region and season. For a general overview yearly averages are compared in Table B6. Particularly insightful is the central range, which already excluded extremes of the (indicated) maximum and minimum models.

[148] Models agree on the following: (1) dominant carbon contributions for central Africa and South America, (2) high sulfate and carbon contributions in and off Europe and Asia, (3) dominant sea-salt contributions in midlatitudes of the Southern Hemisphere, and (4) dominant dust contributions over central Asia and Northern Africa.

[149] Models disagree on the following: (1) source strength for dust and tropical biomass burning, (2) sea-salt contributions over tropical oceans, (3) carbon contributions over tropical and Southern Hemispheric oceans, and (4) dust contributions, especially for off-source regions.

Appendix C: Local Comparisons of Aerosol Optical Depths

[150] Here, model and satellite data are compared to ground statistics at 20 AERONET sites. The coarse horizontal resolution of models (coarser than 2°lat × 2°lon) and of satellite data sets (1°lat × 1°lon) required interpolations. Only data of the four closest grid points was considered. Comparisons are limited to aerosol optical depth properties of yearly average, seasonality strength and seasonality phase. Seasonality strength is the ratio between the (maximum-minimum)

Table B6. Contributions to Total Aerosol Optical Depth for the 20 Regions of Figure 2[a]

	Aerosol Optical Thickness											
	Carbon			Sulfate			Sea Salt			Dust		
	τ, %	Max/Min	Range, %	τ, %	Max/Min	Range, %	τ, %	Max/Min	Range, %	τ, %	Max/Min	Range, %
1: NW Atlantic	10	***CC***/*UL*	16–6	47	***MI***/*Gr*	52–32	28	***Gr***/*MI*	38–20	15	***GO***/*MI*	31–5
2: E. Atlantic	16	***GI***/*UL*	26–5	19	***MI***/*EC*	20–10	13	***UL***/*EC*	19–7	51	***EC***/*MI*	62–41
3: SE Atlantic	46	***CC***/*EC*	58–36	22	***MI***/*Gr*	33–16	13	***Gr***/*GI*	15–10	18	***EC***/*UL*	30–4
4: SW Atlantic	19	***CC***/*UL*	27–13	27	***MI***/*UL*	37–11	31	***Gr***/*MI*	38–19	24	***UL***/*EC*	31–6
5: S. Atlantic	8	***CC***/*UL*	8–2	20	***MI***/*Gr*	25–14	66	***Gr***/*CC*	80–61	5	***GO***/*MI*	7–3
6: Indian O.	20	***GI***/*Gr*	30–10	28	***MI***/*CC*	38–21	37	***Gr***/*CC*	48–18	16	***GI***/*UL*	24–5
7: NW Pacific	15	***GI***/*UL*	21–11	41	***MI***/*Gr*	57–30	21	***Gr***/*GI*	27–13	22	***GO***/*MI*	35–12
8: W. Pacific	15	***GI***/*EC*	16–7	35	***MI***/*CC*	45–25	36	***Gr***/*GI*	56–23	14	***GO***/*UL*	30–3
9: N. Pacific	10	***GI***/*Gr*	15–6	38	***MI***/*Gr*	53–28	30	***Gr***/*GI*	45–23	21	***GO***/*MI*	35–12
10: mid–Pacific	13	***GI***/*UL*	15–5	34	***MI***/*CC*	39–23	42	***CC***/*GI*	63–26	11	***GO***/*UL*	24–2
11: S. Pacific	9	***MI***/*Gr*	14–3	26	***MI***/*Gr*	29–18	54	***Gr***/*MI*	65–47	11	***CC***/*MI*	17–3
12: E. Pacific	22	***GI***/*UL*	29–15	37	***MI***/*Gr*	40–26	28	***UL***/*GI*	41–16	13	***GO***/*MI*	21–3
13: SE Pacific	8	***GI***/*Gr*	14–2	28	***MI***/*Gr*	34–18	54	***Gr***/*MI*	61–45	10	***GO***/*MI*	15–3
N. Africa	11	***MI***/*EC*	13–8	20	***MI***/*CC*	34–8	3	***UL***/*GO*	4–1	66	***Gr***/*MI*	77–48
Asia	15	***CC***/*GO*	16–11	31	***MI***/*Gr*	44–22	2	***EC***/*GI*	2–1	52	***Gr***/*EC*	68–32
E. Asia	30	***GI***/*GO*	37–25	49	***UL***/*Gr*	54–36	3	***Gr***/*UL*	4–1	18	***GO***/*MI*	25–10
Europe	39	***GI***/*GO*	46–35	46	***MI***/*Gr*	48–40	5	***Gr***/*MI*	9–2	10	***GO***/*MI*	15–1
Africa	57	***CC***/*EC*	64–52	23	***UL***/*Gr*	31–16	2	***Gr***/*MI*	3–1	17	***GI***/*MI*	27–6
S. America	52	***CC***/*UL*	59–41	30	***UL***/*Gr*	37–21	5	***Gr***/*MI*	6–2	14	***GO***/*MI*	20–3
N. America	19	***CC***/*GI*	21–14	48	***MI***/*Gr*	56–41	6	***EC***/*MI*	10–1	27	***Gr***/*MI*	34–10

[a]Listed by aerosol type are the yearly average, models with the highest (“Max”; italic-bold) and lowest fraction (“Min”; italic) and the central range of fractional contributions (after removing the identified models with the highest and lowest fraction). Models: EC, ECHAM4; GO, GOCART; MI, MIRAGE; GI, GISS; CC, CCSR; Gr, Grantour; UL, ULAQ.

Table C1. Simulations of Aerosol Optical Depth at 20 AERONET Sites: Yearly Average and Seasonality Strength[a]

	Aerosol Optical Thickness (Yearly Average in g/m^2, Seasonality-Strength)									
	AER	EC	GO	MI	GI	CC	Gr	UL	MO	TO
Urban outflow										
Ispra	**.38**, *0.5*	**.18**, *0.6*	**.27**, *0.7*	**.17**, *0.9*	**.20**, *0.9*	**.29**, *0.4*	**.19**, *0.5*	**.26**, *0.6*	**.25**, *0.6*	**.34**, *1.0*
Bondville	**.16**, *1.5*	**.14**, *0.5*	**.17**, *0.3*	**.24**, *0.4*	**.16**, *1.0*	**.17**, *0.6*	**.13**, *1.1*	**.18**, *0.7*	**.24**, *0.7*	**.25**, *0.3*
Keiimkujik	**.13**, *0.3*	**.13**, *0.7*	**.16**, *0.3*	**.22**, *0.6*	**.11**, *0.7*	**.17**, *0.4*	**.14**, *0.5*	**.16**, *0.6*	**.20**, *0.7*	**.34**, *0.3*
Dust outflow										
Cape Verde	**.39**, *0.6*	**.61**, *1.0*	**.39**, *0.7*	**.11**, *0.6*	**.16**, *0.8*	**.36**, *1.1*	**.30**, *0.5*	**.22**, *0.8*	**.40**, *0.9*	**.46**, *1.0*
Bahrain	**.27**, *0.7*	**.20**, *1.1*	**.28**, *0.6*	**.10**, *0.6*	**.28**, *1.2*	**.45**, *1.4*	**.31**, *1.3*	**.77**, *0.8*	**.32**, *0.5*	**.45**, *0.8*
Sede Boker	**.17**, *0.5*	**.21**, *1.1*	**.27**, *0.6*	**.10**, *0.3*	**.20**, *0.9*	**.26**, *1.2*	**.21**, *0.7*	**.64**, *1.1*	**.30**, *0.6*	**.31**, *0.1*
Dalanzadgad	**.10**, *1.3*	**.15**, *0.8*	**.30**, *0.7*	**.12**, *0.5*	**.29**, *1.1*	**.09**, *1.4*	**.23**, *1.1*	**.63**, *0.9*	–	**.19**, *0.7*
Biomass outflow										
Mongu	**.20**, *1.9*	**.11**, *1.2*	**.14**, *2.1*	**.08**, *0.6*	**.11**, *1.4*	**.21**, *1.3*	**.14**, *1.3*	**.19**, *1.0*	**.19**, *1.4*	**.22**, *0.7*
Alta Floresta	**.35**, *2.2*	**.13**, *1.9*	**.15**, *2.5*	**.14**, *1.0*	**.13**, *1.8*	**.14**, *2.6*	**.23**, *1.1*	**.33**, *1.2*	**.22**, *1.6*	**.40**, *1.1*
Ilorin	**.47**, *1.1*	**.48**, *1.6*	**.35**, *1.0*	**.17**, *1.2*	**.16**, *1.1*	**.42**, *0.9*	**.41**, *0.5*	**.21**, *1.0*	**.38**, *0.6*	**.51**, *0.5*
Rural										
Sevilletta	**.06**, *1.0*	**.06**, *0.7*	**.11**, *0.7*	**.08**, *0.6*	**.11**, *1.0*	**.06**, *1.2*	**.09**, *0.7*	**.12**, *0.4*	**.19**, *1.0*	**.24**, *1.0*
Waskesiu	**.12**, *1.4*	**.07**, *0.5*	**.14**, *0.3*	**.11**, *0.5*	**.09**, *0.9*	**.03**, *0.8*	**.06**, *1.0*	**.12**, *0.6*	**.16**, *1.4*	**.28**, *0.4*
HJ Andrews	**.08**, *1.4*	**.06**, *0.7*	**.15**, *0.3*	**.10**, *0.4*	**.09**, *0.8*	**.03**, *0.5*	**.07**, *0.2*	**.08**, *0.3*	**.14**, *0.7*	**.21**, *0.3*
Bonanza Cr.	**.07**, *0.7*	**.08**, *0.3*	**.16**, *0.2*	**.15**, *1.0*	**.13**, *0.5*	**.02**, *0.6*	**.04**, *0.5*	**.12**, *0.4*	**.16**, *1.0*	**.31**, *0.5*
Maritime										
Kaashidhoo	**.16**, *0.9*	**.08**, *0.4*	**.09**, *1.3*	**.04**, *0.4*	**.04**, *0.3*	**.16**, *1.3*	**.13**, *0.6*	**.12**, *0.6*	**.21**, *0.4*	**.21**, *0.2*
Nauru	**.07**, *0.4*	**.02**, *0.4*	**.03**, *0.5*	**.03**, *0.3*	**.02**, *0.2*	**.04**, *0.3*	**.07**, *0.3*	**.04**, *0.2*	**.08**, *0.7*	**.21**, *0.1*
Lanai	**.07**, *0.8*	**.06**, *0.9*	**.12**, *0.5*	**.07**, *0.6*	**.04**, *0.7*	**.05**, *0.3*	**.11**, *0.3*	**.06**, *0.3*	**.15**, *0.6*	**.19**, *0.2*
Coastal										
San Nicolas	**.07**, *1.1*	**.06**, *0.8*	**.12**, *0.5*	**.09**, *0.5*	**.09**, *0.8*	**.06**, *0.5*	**.07**, *0.2*	**.09**, *0.2*	**.19**, *0.7*	**.25**, *0.3*
Dry Tortugas	**.15**, *0.8*	**.10**, *0.5*	**.10**, *0.4*	**.11**, *0.4*	**.08**, *0.7*	**.09**, *0.7*	**.17**, *0.3*	**.19**, *0.4*	**.17**, *0.5*	**.23**, *0.2*
Aire Adour	**.23**, *0.4*	**.13**, *0.5*	**.22**, *0.7*	**.14**, *0.7*	**.13**, *0.3*	**.18**, *0.6*	**.14**, *0.3*	**.20**, *0.4*	**.23**, *0.6*	**.26**, *0.5*

[a]Data of models and satellite data spatially interpolated. Data pairs indicate the yearly average (first value, in bold) and the seasonality (second value, in italics). Ground-data: Aeronet; Models: ECHAM4, GOCART, MIRAGE, GISS, CCSR, Grantour, ULAQ; Satellites: MODIS, TOMS.

range of the three-month running average during a year and the yearly average. Seasonality phase is identified by the (center-) months associated with the maximum and minimum of a three-month running average during a year.

[151] Local comparisons of Table C1 compare yearly average and seasonality strength (or range). Table C2 compares the seasonality phase and Table C3 statistically quantifies the matches to AERONET from comparisons in Tables C1 and C2. Requirements for local matches were usually less stringent than for regional comparisons (in Table B3), because of uncertainties with the regional representation of many AERONET sites.

Table C2. Simulations of Aerosol Optical Depth at 20 AERONET Sites: Seasonality Phase (Months of Maxima and Minima)[a]

	Aerosol Optical Thickness (Seasonal Maximum–Seasonal Minimum)									
	AER	EC	GO	MI	GI	CC	Gr	UL	MO	TO
Urban outflow										
Ispra	***Apr–Dec***	**May–Jan**	Sep–Jan	Jul–Feb	Jun–Dec	**Apr**–Oct	Jul–Feb	Jul–Nov	Jun–Nov	**May**–Oct
Bondville	***Aug–Jan***	**Aug–Jan**	**Aug–Jan**	May–Jan	**Jul–Jan**	**Aug–Dec**	**Sep–Jan**	**Aug**–Mar	Feb–Nov	**Aug**–Apr
Keiimkujik	***Jun–Nov***	**Jul**–Jan	Apr–Jul	**Jul**–Jan	**May**–Jan	**Jul**–Apr	**Jul–Dec**	**Jul**–Jan	**Jul**–Jan	Jan–Nov
Dust outflow										
Cape Verde	***Jul–Apr***	Mar–Aug	**Jul**–Dec	Jan–Apr	Mar–Oct	**Jul**–Dec	**Aug–May**	**Jul**–Dec	**Jul**–Dec	**Jul**–Nov
Bahrain	***Aug–Dec***	May–Dec	Jun–Dec	**Aug–Dec**	**Jul–Dec**	**Jul–Dec**	**Jul–Jan**	**Jul–Jan**	**Aug–Dec**	Jun–Nov
Sede Boker	***Aug–Jan***	May–Dec	Apr–Feb	May–Sep	**Aug–Dec**	May–Feb	**Jul–Jan**	**Jul–Dec**	May–Dec	May–Dec
Dalanzadgad	***Apr–Dec***	**May–Dec**	Jul–Jan	Jun–Feb	**May–Jan**	Jul–Jan	Jul–Jan	Jul–Jan	–	Jun–Oct
Biomass outflow										
Mongu	***Sep–Apr***	**Oct–Mar**	**Oct**–Feb	Nov–May	**Aug–Mar**	Jul–Mar	**Aug–Apr**	**Aug–Mar**	**Sep**–Jun	**Oct–May**
Alta Floresta	***Sep–Apr***	**Sep**–Jan	**Aug**–Jan	Jun–Nov	Jul–Mar	Jul–Mar	**Aug**–Dec	**Aug**–Feb	**Oct**–Jun	**Sep**–Jun
Ilorin	***Jan–Aug***	**Feb–Jul**	**Jan–Aug**	**Feb–Sep**	**Feb–Sep**	**Jan–Aug**	**Feb**–Oct	**Feb–Aug**	**Feb–Aug**	Mar–Sep
Rural										
Sevilletta	***Jul–Jan***	May–Jan	**Jun–Dec**	Apr–Dec	**Jul–Feb**	**Aug–Jan**	Sep–Dec	**Jul–Feb**	Jan–Oct	**Jun–Dec**
Waskesiu	***May–Jan***	**May–Jan**	**May–Jan**	**Apr–Jan**	**May–Dec**	**May–Jan**	Jul–Jan	Aug–Apr	**Apr**–Nov	Aug–Nov
HJ Andrews	***Apr–Dec***	**May–Dec**	**May–Nov**	**Apr**–Aug	**May–Jan**	Aug–Jan	Nov–Aug	Aug–Jan	**Apr–Nov**	**Apr–Nov**
Bonanza Cr.	***Jun–Oct***	**May–Nov**	**May–Sep**	Nov–Aug	**May–Nov**	**Jul**–Mar	Nov–May	Aug–Mar	May–Oct	Mar–Aug
Maritime										
Kaashidhoo	***Feb–Aug***	Jun–Nov	Jul–Nov	**Feb–Sep**	**Feb**–Oct	Jul–Nov	Jul–Nov	Aug–Apr	Jul–Apr	Dec–Feb
Nauru	***Feb–Sep***	Jul–Nov	**Feb**–Jun	**Jan**–Jun	**Mar**–Nov	Nov–Jun	**Feb**–Oct	Aug–May	**Feb–Aug**	Oct–Jan
Lanai	***Apr–Oct***	**May**–Dec	**May–Oct**	**Apr–Oct**	**May–Oct**	Jul–Jan	Feb–Sep	Dec–Jun	**May**–Dec	Jun–Sep
Coastal										
San Nicolas	***Apr–Dec***	**May–Jan**	Jun–Dec	Aug–Dec	Jul–Feb	Aug–Jan	Aug–Dec	Jul–Feb	**May–Jan**	Aug–Dec
Dry Tortugas	***Jun–Nov***	Apr–Dec	**Jun**–Jan	Apr–Dec	Mar–Dec	**Jul**–Jan	**Jul–Nov**	**Jul**–Jan	Apr–Dec	Feb–Sep
Aire Adour	***May–Nov***	**Apr–Dec**	Aug–Dec	Jul–Jan	**Jun**–Mar	**Apr–Oct**	Jul–Oct	Jul–Oct	Jul–Oct	Jul–Jan

[a]Bold indicates model simulations or satellite data whose maxima (or maxima and minima) differ by less than two months from extremes of AERONET. Ground data: AERONET; Models: ECHAM4, GOCART, MIRAGE, GISS, CCSR, Grantour, ULAQ; Satellites: MODIS, TOMS.

Table C3. Agreement to Data at 20 AERONET Sites: Simulated and Retrieved Aerosol Optical Depths[a]

	Aerosol Optical Thickness Versus AERONET								
	EC (>, ∼, <)	GO (>, ∼, <)	MI (>, ∼, <)	GI (>, ∼, <)	CC (>, ∼, <)	Gr (>, ∼, <)	UL (>, ∼, <)	MO (>, ∼, <)	TO (>, ∼, <)
Yearly average	*2*, ***10***, *8*	*7*, **9**, 4	*3*, *7*, *10*	*3*, *7*, *10*	*3*, ***11***, *6*	*3*, ***12***, *5*	*5*, ***12***, *3*	*9*, ***9***, *1*	*14*, ***6***, –
Season strength	*4*, ***12***, *4*	*1*, ***14***, *5*	*3*, ***9***, *8*	*4*, ***15***, *1*	*3*, ***13***, *4*	*1*, ***14***, *5*	*2*, ***12***, *6*	*2*, ***15***, *2*	*2*, *7*, *14*
Avg + s-str.	**5**	**6**	**3**	**4**	**7**	**7**	**5**	**8**	**1**
Season phase	***13***	***13***	***8***	***14***	***11***	***10***	***10***	***11***	*7*
Avg + s-str. + s-ph	4	3	1	3	4	6	2	5	1

[a]Here, avg, yearly average; s-str., seasonality strength; and s-phase, phase. Often a distinction was made between clearly larger values (>), clearly smaller values (<) and general agreement (∼). Yearly averages were considered agreeable, when the simulated optical depth remained within 30% of the AERONET value. Seasonality strength was considered agreeable for variations within 50% of the AERONET value. Seasonality phase was considered agreeable phase when the month of with the maximum the three-month running average for optical depths had not shifted by more than one month from the month of the AERONET maximum. The last line indicates out of 20 the number of sites, where all three aerosol properties matches with AERONET statistics.

[152] For models the yearly average of simulated aerosol optical depth agrees at 35 to 60% of the AERONET sites. Underestimates are more common than overestimates, except in GOCART (very efficient transport) and ULAQ (strong urban sources). Simulated seasonality strength for aerosol optical depth is usually stronger near dust sources, but weaker at midlatitude sites of the Northern Hemisphere (AERONET minima are lower) and also weaker at biomass burning sites in the tropics (AERONET maxima are higher). Simulated seasonality maxima (phase) are correct at 40 to 70% of the AERONET sites. Matches of all three aerosol properties (yearly average, seasonality strength and seasonality phase) occur only at a rate of about 1 in 4.

[153] For more temporal detail seasonal comparisons are provided in Figure C1, where seasonal biases with respect to AERONET statistics can be explored.

[154] For satellites, there is a clear bias toward larger yearly averages. In particular, low seasonal minima (aerosol

	EC				MI				GO				GI				CC				Gr				UL			
-- seasons --	1	2	3	4	1	2	3	4	1	2	3	4	1	2	3	4	1	2	3	4	1	2	3	4	1	2	3	4
Mongu	↓	=	↓	↓	↓	=	↓	⇊	↓	=	↓	=	↓	=	↓	⇊	=	↑	↑	↓	↓	=	=	⇊	=	↑	↑	↓
Seviletta	=	=	=	=	↑	↑	=	=	↑	↑	↑	↑	↑	↑	↑	↑	=	↓	=	=	↑	=	=	↑	↑	↑	↑	↑
Cuiaba	↓	/	↓	⇊	↓	/	↓	⇊	↓	/	↓	⇊	↓	/	↓	⇊	↓	/	↑	⇊	↓	/	↑	⇊	↑	/	↑	↓
Banizoumbou	=	↑	↓	↓	⇊	⇊	⇊	⇊	↑	↓	↑	↑	↓	⇊	⇊	⇊	↑	↓	=	=	=	↓	=	↓	↑	↑	↑	↑
Cape Verde	⇈	⇈	↓	=	⇊	⇊	⇊	⇊	↑	↓	=	↑	↓	↓	⇊	⇊	↓	=	↑	↓	↓	↓	⇊	↓	↓	↓	⇊	↓
Waskesiu	↑	↓	↓	=	↑	↓	↓	↑	↑	=	=	↑	=	↓	↓	↑	=	↓	↓	↓	=	↓	↓	=	↑	↓	↓	↑
Goddard	↑	↑	↓	↑	↑	↑	↑	↑	↑	↑	↓	↑	=	=	↓	=	↑	↑	↑	↑	=	=	↓	↑	↑	↑	↑	↑
HJ Andrews	=	↓	=	=	↑	=	=	↑	↑	↑	↑	↑	=	↓	↑	=	=	↓	↓	↓	↑	↓	=	=	↑	↓	=	↑
Ispra	↓	↓	↓	↓	↓	↓	↓	↓	↓	↓	↑	↑	↓	↓	=	↓	↑	=	↑	=	↓	↓	=	↓	=	↓	↑	=
Dry Tortugas	↓	↓	↓	↓	↓	↓	↓	↓	↓	↓	↓	=	↓	↓	↓	↓	↓	↓	↓	↓	↑	↓	↑	↑	↑	=	↑	↑
Lanai	↓	↓	=	=	=	=	=	=	↑	↑	↑	↑	↓	↓	=	=	↓	↓	=	=	↑	=	↑	↑	=	↓	=	=
Alta Floresta	↓	↓	↓	⇊	=	↑	↓	⇊	↓	↓	=	⇊	↓	=	↓	⇊	↓	↓	↓	⇊	↑	↑	↓	⇊	↑	↑	↑	⇊
Bahrain	↓	=	↓	↓	↓	↓	⇊	↓	↑	↑	↑	↑	↓	=	↑	=	=	⇈	⇈	=	↓	↓	↑	=	⇈	⇈	⇈	⇈
Mexico City	/	↓	⇊	/	/	↓	⇊	/	/	↓	⇊	/	/	↓	⇊	/	/	⇊	⇊	/	/	↓	↓	/	/	⇊	⇊	/
Bondville	↑	=	↓	=	↑	↑	=	↑	↑	↑	↓	↑	=	=	↓	=	↑	↑	↓	=	=	↓	↓	=	↑	=	↓	↑
Ilorin	=	⇈	↓	↓	⇊	⇊	↓	⇊	↓	↓	↓	↓	⇊	⇊	↓	⇊	↓	↓	↑	=	⇊	↓	↑	=	⇊	⇊	↓	↓
Dalanzadgad	↑	=	↑	↑	↑	↓	↑	↑	↑	↑	⇈	⇈	↑	⇈	⇈	↑	↓	↓	↑	↑	↑	↑	⇈	↑	⇈	⇈	⇈	⇈
Conception	↓	/	⇊	↓	↓	/	↓	⇊	↓	/	↓	⇊	↓	/	↓	⇊	↓	/	↓	⇊	↓	/	↓	↓	↑	/	↓	↓
Sede Boker	=	↑	↑	↓	↓	↓	↓	↓	↑	↑	↑	↑	=	↑	↑	=	↑	↑	↑	↑	=	↑	↑	↑	⇈	⇈	⇈	⇈
Arica	⇊	⇊	↓	↓	⇊	⇊	↓	↓	↓	⇊	↓	↓	⇊	⇊	↓	↓	⇊	⇊	↓	↓	↓	⇊	↓	↓	↓	↓	=	↓
Kaashidhoo	↓	↓	↓	↓	↓	↓	↓	↓	↓	↓	↑	↓	↓	↓	↓	↓	↓	↓	↑	↓	↓	↓	↑	=	↓	↓	↑	=
San Nicolas	=	↓	=	=	↑	=	=	=	↑	↑	↑	↑	=	↑	↑	=	=	↓	=	=	↑	↓	=	=	↑	↓	=	=
Nauru	↓	↓	↓	↓	↓	↓	↓	↓	↓	↓	↓	↓	↓	↓	↓	↓	↓	↓	↓	=	=	=	=	=	↓	↓	↓	↓
Aire Adour	↓	↓	↓	↓	↓	↓	↓	↓	=	=	=	↑	↓	↓	↓	↓	=	↓	↓	↓	↓	↓	↓	↓	↑	↓	=	=
Bonanza Cr.	/	=	=	↑	/	↑	↑	↑	/	↑	↑	↑	/	↑	↑	↑	/	↓	↓	↓	/	↓	↓	=	/	↑	↑	↑
Kejimkujik	=	↓	=	=	↑	↑	↑	↑	↑	↑	=	↑	↓	↓	↓	=	↑	↓	↑	↑	=	↓	=	=	↑	↓	↑	↑

(⇊<-0.2, -0.2<↓<-0.1, -0.1<↓<-0.02, -0.02< = <0.02, 0.02<↑<0.1, 0.1<↑<0.2, 0.2<⇈, / : no data)

Figure C1. Model-based deviations with respect to multiyear statistics at 26 AERONET sites for seasonally averaged aerosol optical depth (1, Dec–Jan–Feb; 2, Mar–April–May; 3, June–July–Aug; 4, Sept–Oct–Nov). Results for all seven models are displayed and more meaningful deviations in excess of ±0.1 for optical depth are indicated by solid arrows. Because of a characterization by local pollution at Mexico City and Arica, model underestimates are expected at these sites.

optical depths below 0.1) are rarely reproduced. This tendency is particularly strong for TOMS in remote regions. In those regions, where cloud contamination issues gain in importance, yearly average values are larger and seasonality strength is weaker than AERONET. Near aerosol source regions (as aerosol optical depths exceed 0.3) TOMS displays better skill. MODIS shows numerous matches at a variety of AERONET sites, but not more frequent than the better models. This is disappointing but may in part be related to sampling biases. MODIS can detect near clouds, whereas AERONET prefers completely cloud-free environments. Since aerosol optical depths near-clouds are usually larger, MODIS averages are expected to exceed AERONET. Thus it remains an open question, to what degree the MODIS tendency toward larger optical depth averages in reference AERONET is real or a sampling artifact.

References

Barrie, L., et al., A comparison of large scale atmospheric sulphate aerosol models (COSAM): Overview and highlights, *Tellus, Ser. B*, *53*, 615–645, 2001.

Benkowitz, C., M. Scholtz, J. Pacyna, L. Tarrason, J. Dignon, E. Voldner, P. Spiro, J. Logan, and T. Graedel, Global gridded inventories of anthropogenic emissions of sulfur and nitrogen, *J. Geophys. Res.*, *101*, 29,239–29,253, 1996.

Chin, M., R. Rood, S.-J. Lin, J.-F. Muller, and A. Thompson, Atmospheric sulfur cycle simulated in the global model GOCART: Model description and global properties, *J. Geophys. Res.*, *105*, 24,671–24,687, 2000.

Chin, M., P. Ginoux, S. Kinne, O. Torres, B. Holben, B. Duncan, R. Martin, J. Logan, A. Hiragushi, and T. Nakajima, Tropospheric aerosol optical thickness from the GOCART model and comparisons with satellite and sunphotometer measurements, *J. Atmos. Sci.*, *59*, 461–483, 2002.

Chu, D. A., Y. Kaufman, C. Ichoku, L. Remer, D. Tanre, and B. Holben, Validation of MODIS aerosol optical depth retrieval over land, *Geophys. Res. Lett.*, *29*(12), 8007, doi:10.1029/2001GL013205, 2002.

Cooke, W., and J. Wilson, A global black carbon aerosol model, *J. Geophys. Res.*, *101*, 19,395–19,409, 1996.

Cooke, W., C. Liousse, H. Cachier, and J. Feichter, Construction of $1° \times 1°$ fossil fuel emission data set for carbonaceous aerosol and implementation and radiative impact in the ECHAM4 model, *J. Geophys. Res.*, *104*, 22,137–22,162, 1999.

Dubovik, O., and M. King, A flexible inversion algorithm for the retrieval of aerosol optical properties from Sun and sky radiance measurements, *J. Geophys. Res.*, *105*, 20,673–20,696, 2000.

Dubovik, O., A. Smirnov, B. Holben, M. King, Y. Kaufman, T. Eck, and I. Slutsker, Accuracy assessments of aerosol optical properties retrieved from AERONET Sun and sky radiance measurements, *J. Geophys. Res.*, *105*, 9791–9806, 2000.

Dubovik, O., B. Holben, T. Eck, A. Smirnov, Y. Kaufman, M. King, D. Tanre, and I. Slutsker, Variability of absorption and optical properties of key aerosol types observed in worldwide locations, *J. Atmos. Sci.*, *59*, 590–608, 2002.

Duncan, B., R. Martin, A. Standt, R. Yevich, and J. Logan, Interannual and seasonal variability of biomass burning emissions constrained by satellite observations, *J. Geophys. Res.*, *108*(D2), 4100, doi:10.1029/2002JD002378, 2003.

Eck, T., B. Holben, J. Reid, O. Dubovik, A. Smirnov, N. O'Neill, I. Slutsker, and S. Kinne, Wavelength dependence of the optical depth of biomass burning, urban and desert dust aerosols, *J. Geophys. Res.*, *104*, 31,333–31,349, 1999.

Erickson, D., J. Merill, and R. Duce, Seasonal estimates of global atmospheric sea-salt contribution, *J. Geophys. Res.*, *91*, 1067–1072, 1986.

Geogdzhayev, I., M. Mishchenko, W. Rossow, B. Cairns, and A. Lacis, Global 2-channel AVHRR retrieval of aerosol properties over the ocean for the period of NOAA-9 observations and preliminary retrievals using NOAA-7 and NOAA-11 data, *J. Atmos. Sci.*, *59*, 262–278, 2002.

Ghan, S., R. Easter, E. Chapman, H. Abdul-Razzak, Y. Zhang, L. Leung, N. Laulainen, R. Saylor, and R. Zaveri, A physically based estimate of radiative forcing by anthropogenic sulfate aerosol, *J. Geophys. Res.*, *106*, 5279–5293, 2001a.

Ghan, S., N. Laulainen, R. Easter, R. Wagener, S. Nemesure, E. Chapman, Y. Zhang, and R. Leung, Evaluation of aerosol direct forcing in MIRAGE, *J. Geophys. Res.*, *106*, 5295–5316, 2001b.

Gillette, D., A wind tunnel simulation of the erosion of soil: Effect of soil texture, sandblasting, wind-speed, and soil consolidation, *Atmos. Environ.*, *12*, 1735–1743, 1978.

Gillette, D., and R. Passi, Modeling dust emission caused by wind erosion, *J. Geophys. Res.*, *93*, 14,233–14,242, 1988.

Ginoux, P., M. Chin, I. Tegen, J. Prospero, B. Holben, O. Dubovik, and S.-J.Lin, Sources and distributions of dust aerosol simulated with the GOCART model, *J. Geophys. Res.*, *106*, 20,255–20,273, 2001.

Gong, S., L. Barrie, J. Prospero, D. Savoie, G. Ayers, J.-P. Blanchet, and L. Spacek, Modeling sea-salt in the atmosphere, atmospheric concentration and fluxes, *J. Geophys. Res.*, *102*, 3819–3830, 1997.

Guelle, W., M. Schulz, Y. Balkanski, and F. Dentener, Influence of the source formulation on modeling the atmospheric global distribution of sea-salt aerosol, *J. Geophys. Res.*, *106*, 27,509–27,524, 2001.

Guenther, A., et al., A global model for natural volatile organic compound emissions, *J. Geophys. Res.*, *100*, 8873–8892, 1995.

Hobbs, P., J. Reid, A. Kotchenruther, R. Ferek, and R. Weiss, Direct radiative forcing by smoke from biomass burning, *Science*, *275*, 1776–1777, 1997.

Holben, B., et al., AERONET: A federated instrument network and data-archive for aerosol characterization, *Remote Sens. Environ.*, *66*, 1–16, 1998.

Holben, B., et al., An emerging ground-based aerosol climatology: Aerosol optical depth from AERONET, *J. Geophys. Res.*, *106*, 12,067–12,097, 2000.

Houghton, J., L. Meira Filho, J. Bruce, H. Lee, B. Callander, E. Haites, N. Harris, and K. Maskell, *Climate Change 1994: Radiative Forcing and Climate Change and an Evaluation of the IPCC (International Panel on Climate Change) IS 92 Emission Scenarios*, Cambridge Univ. Press, New York, 1995.

Houghton, J., et al., *Climate Change 2001: The Scientific Basis, An Evaluation of the IPCC (International Panel on Climate Change)*, Cambridge Univ. Press, New York, 2001.

Kaufman, Y., D. Tanre, L. Remer, E. Vermote, D. Chu, and B. Holben, Operational remote sensing of tropospheric aerosol over the land from EOS-MODIS, *J. Geophys. Res.*, *102*, 17,051–17,061, 1997a.

Kaufman, Y., et al., The MODIS 2.1 μm channel: Correlation with visible reflectance for use in remote sensing of aerosol, *IEEE Trans. Geosci. Remote Sens.*, *35*(5), 1286–1298, 1997b.

Kaufman, Y., D. Tanre, O. Dubovik, A. Karnieli, and L. Remer, Absorption of sunlight by dust as inferred from satellite and groundbased remote sensing, *Geophys. Res. Lett.*, *28*, 1479–1482, 2001.

Koch, D., The transport and direct radiative forcing of carbonaceous and sulfate aerosol in the GISS GCM, *J. Geophys. Res.*, *106*, 20,311–20,332, 2001.

Koch, D., D. Jacob, I. Tegen, D. Rind, and M. Chin, Tropospheric sulfur simulation and sulfate direct forcing in the Goddard Institute for Space Studies (GISS) general circulation model, *J. Geophys. Res.*, *104*, 23,799–23,822, 1999.

Koehler, H., The nucleus in the growth of hygroscopic droplets, *Trans. Faraday Soc.*, *32*, 1152–1161, 1936.

Koepke, P., M. Hess, I. Schult, and E. P. Shettle, Global aerosol data set, *Tech. Rep. 243*, Max-Planck-Inst. für Meteorol., Hamburg, Germany, 1997.

Liousse, C., J. Penner, C. Chuang, J. Walton, H. Eddleman, and H. Cachier, A global three-dimensional model study of carbonaceous aerosol, *J. Geophys. Res.*, *101*, 19,411–19,432, 1996.

Lohmann, U., J. Feichter, C. Chuang, and J. Penner, Predicting the number of cloud droplets in the ECHAM GCM, *J. Geophys. Res.*, *104*, 24,557–24,563, 1999.

Lohmann, U., et al., Vertical distributions of sulfur species simulated by large scale atmospheric models in COSAM: Comparison with observations, *Tellus, Ser. B*, *53*, 646–672, 2001.

Malm, W., J. F. Sisler, D. Hoffmann, R. Eldred, and T. Cahill, Spatial and seasonal trends in particle concentration and optical extinction in the United States, *J. Geophys. Res.*, *99*, 1347–1370, 1994.

Mishchenko, M., I. Geogdzhayev, B. Cairns, W. Rossow, and A. Lacis, Aerosol retrievals over ocean using channel 1 and 2 AVHRR data: A sensitivity study and preliminary results, *Appl. Opt.*, *36*, 7325–7341, 1999.

Monahan, E., D. Spiel, and K. Davidson, A model of marine aerosol generation via whitecaps and wave-disruptions, in *Oceanic Whitecaps*, pp. 167–174, D. Reidel, Norwell, Mass., 1986.

Novakov, T., D. Hegg, and P. Hobbs, Airborne measurements of carbonaceous aerosols on the east coast of the United States, *J. Geophys. Res.*, *102*, 30,023–30,030, 1997.

O'Dowd, C. D., M. H. Smith, I. E. Consterdine, and J. A. Lowe, Marine aerosols, sea-salt, and the marine sulfur cycle: A short review, *Atmos. Environ.*, *31*, 73–80, 1997.

Olivier, J., A. Bouwan, C. Van der Mass, J. Berdowski, C. Veldt, J. Bloss, A. Vesschedijk, P. Znaweld, and J. Haverlag, Description of EDGAR

version 2.0: A set of global emission inventories of greenhouse gases and ozone depleting substances for all anthropogenic and most natural sources on a per country basis on a 1 × 1 grid, *RIVM/TNO Rep. 771060 002*, RIVM, Bilthoven, Netherlands, Dec. 1996.

Patterson, E., D. Gilette, and B. Stockton, complex index of refraction between 300 and 700nm for Saharan aerosol, *J. Geophys. Res.*, *81*, 5733–5748, 1976.

Penner, J., et al., A comparison of model- and satellite-derived aerosol optical depth and reflectivity, *J. Atmos. Sci.*, *59*, 441–460, 2002.

Pitari, G., E. Mancini, V. Rizi, and D. Shindell, Impact of future climates and emission changes on stratospheric aerosol and climate, *J. Atmos. Sci.*, *59*, 414–440, 2002.

Remer, L., et al., Validation of MODIS aerosol retrieval over ocean, *Geophys. Res. Lett.*, *29*(12), 8008, doi:10.1029/2001GL013204, 2002.

Roeckner, E., K. Arpe, L. Bengtsson, M. Christoph, M. Claussen, L. Duemenil, M. Esch, M. Giorgetta, U. Schlese, and U. Schulzweida, The atmospheric general circulation model ECHAM-4: Model description and simulation of present-day climate, *Tech. Rep. 218*, Max-Planck-Inst. für Meteorol., Hamburg, Germany, 1996.

Roelofs, G.-J., et al., Analysis of regional budgets of sulfur species modelled for the COSAM exercise, *Tellus, Ser. B*, *53*, 673–694, 2001.

Rossow, W., A. Walker, and C. Garder, Comparison of ISCCP and other cloud amounts, *J. Clim.*, *6*, 2394–2418, 1993.

Schaaf, C., et al., First observational BRDF, albedo and nadir reflectance from MODIS, *Remote Sens. Environ.*, *83*, 135–148, 2002.

Schulz, M., Y. Balkanski, F. Dulac, and W. Guelle, Role of aerosol size distribution and source location in a three-dimensional simulation of a Saharan dust episode tested against satellite derived optical thickness, *J. Geophys. Res.*, *103*, 10,579–10,592, 1998.

Smirnov, A., B. Holben, T. Eck, O. Dubovik, and I. Slutsker, Cloud screening and quality control algorithms for the AERONET database, *Remote Sens. Environ.*, *73*, 337–349, 2000.

Sokolik, I., and O. B. Toon, incorporation of mineral composition into models of the radiative properties of mineral aerosol from UV to IR wavelengths, *J. Geophys. Res.*, *104*, 9423–9444, 1999.

Stowe, L., H. Jacobowitz, G. Ohring, K. Knapp, and N. Nalli, The advanced very high resolution radiometer Pathfinder Atmosphere (PATMOS) data set: Initial analyses and evaluations, *J. Clim.*, *15*, 1243–1260, 2002.

Takemura, T., H. Okamoto, Y. Maruyama, A. Numaguti, A. Hiragushi, and T. Nakajima, Global three dimensional simulation of aerosol optical thickness distribution of various origins, *J. Geophys. Res.*, *105*, 17,853–17,873, 2000.

Takemura, T., T. Nakajima, O. Dubovik, B. Holben, and S. Kinne, Single scattering albedo and radiative forcing of various aerosol species with a global three-dimensional model, *J. Clim.*, *4*, 333–352, 2002.

Tanre, D., et al., Remote sensing of aerosol properties over ocean using the MODIS/EOS spectral radiances, *J. Geophys. Res.*, *102*, 16,971–16,988, 1997.

Tegen, I., and I. Fung, Contributions to the atmospheric mineral load from land-surface modification, *J. Geophys. Res.*, *100*, 18,707–18,726, 1995.

Tegen, I., P. Hollrig, M. Chin, I. Fung, D. Jacob, and J. Penner, Contribution of different aerosol species to the global aerosol extinction optical thickness: Estimates from model results, *J. Geophys. Res.*, *102*, 23,895–23,915, 1997.

Tegen, I., D. Koch, A. Lacis, and M. Sato, Trends in tropospheric aerosol loads and corresponding impact on direct radiative forcing between 1950 and 1990: A model study, *J. Geophys. Res.*, *105*, 26,971–26,989, 2000.

Torres, O., P. Barthia, J. Herman, Z. Ahmad, and J. Gleason, Derivation of optical properties from satellite measurements of backscattered ultraviolet radiation: Theoretical basis, *J. Geophys. Res.*, *103*, 17,099–17,110, 1998.

Torres, O., P. Barthia, J. Herman, A. Sinyuk, P. Ginoux, and B. Holben, A long-term record of aerosol optical depth from TOMS observations and comparison to AERONET measurements, *J. Atmos. Sci.*, *59*, 398–413, 2002.

Walton, J., M. MacCracken, and S. Ghan, A global-scale Lagrangian trace species model of transport, transformation, and removal processes, *J. Geophys. Res.*, *93*, 8339–8354, 1988.

M. Chin, GIT/NASA Goddard Space Flight Center, M.S. 916.0, Building 21, Room C217, Greenbelt, MD 20771, USA. (chin@gator1.gsfc.nasa.gov)

D. A. Chu, O. Dubovik, T. Eck, I. Slutsker, and A. Smirnov, Goddard Earth Sciences and Technology Center, University of Maryland Baltimore County-NASA Goddard Space Flight Center, Greenbelt, MD 20771, USA. (achu@climate.gsfc.nasa.gov; dubovik@aeronet.gsfc.nasa.gov; tom@aeronet.gsfc.nasa.gov; ilya@aeronet.nasa.gov; asmirnov@spamer.gsfc.nasa.gov)

R. Easter and S. Ghan, Pacific Northwest National Laboratory, Battelle, 6th & P Street, Building 790, Richland, WA 99352, USA. (richard.easter@pnl.gov; steve.ghan@pnl.gov)

J. Feichter, S. Kinne, and C. Timmreck, Max-Planck-Institut für Meteorologie, Bundesstraße 55, D-20146 Hamburg, Germany. (feichter@dkrz.de; kinne@dkrz.de; timmreck@dkrz.de)

I. Geogdzhayev, D. Koch, and M. Mishchenko, NASA Goddard Institute for Space Studies, 2880 Broadway, New York, NY 10025, USA. (ig117@columbia.edu; dorothy.koch@yale.edu; mmishchenko@giss.nasa.gov)

P. Ginoux, Geophysical Fluid Dynamics Laboratory, NOAA, Princeton Forrestal Campus Route 1, P. O. Box 308, Princeton, NJ 08542-0308, USA. (ginoux@rondo.gsfc)

M. Herzog and J. Penner, Department of Atmospheric, Oceanic and Space Sciences, University of Michigan, 2455 Hayward Street, Ann Arbor, MI 48109, USA. (herzogm@umich.edu; penner@umich.edu)

B. Holben and Y. Kaufman, NASA Goddard Space Flight Center, Code 923, Greenbelt, MD 20771, USA. (brent@aeronet.gsfc.nasa.gov; yoram.j.kaufman@nasa.gov)

G. Pitari, Dipartimento di Fisica, Università degli Studi dell'Aquila, I-67010, Coppito L'Aquila, Italy. (pitari@vxscaq.aquila.infn.it)

U. Lohmann, Atmospheric Sciences Program, Department of Physics, Dalhousie University, Halifax, Nova Scotia, Canada B3H 3J5. (ulrike.lohmann@dal.ca)

M. Schulz, Laboratoire des Sciences du Climat et l'Environnement, CEA/CNRS-LSCE, L'Orme des Merisiers, Bat. 709, F-91191, Gif-sur-Yvette Cedex, France. (schulz@lsce.saclay.cea.fr)

T. Takemura, Research Institute for Applied Mechanics, Kyushu University, 6-1 Kasuga-koen, Kasuga, Fukuoka 816-8580, Japan. (toshi@riam.kyushu-u.ac.jp)

D. Tanre, Laboratoire d'Optique Atmosphérique, Université des Sciences et Technologies de Lille 1, Bâtiment P5, F-59655 Villeneuve d'Ascq Cédex, France. (didier.tanre@univ-lille1.fr)

I. Tegen, Max-Planck-Institut für Biogeochemie, P. O. Box 100164, Tatzendpromenade 1a, D-07745 Jena, Germany. (itegen@bgc-jena.mpg.de)

O. Torres, Joint Center for Earth Systems Technology, University of Maryland Baltimore County-NASA Goddard Space Flight Center, Greenbelt, MD 20771, USA. (torres@tparty.gsfc.nasa.gov)